

**FEDERAL UNIVERSITY OF TECHNOLOGY – PARANÁ**

**DANIELA CAROLINA MARQUES**

**EXPERIMENTAL ANALYSIS OF HYDRATE DEPOSITION UNDER  
MULTIPHASE FLOW CONDITIONS**

**CURITIBA**

**2023**

**DANIELA CAROLINA MARQUES**

**EXPERIMENTAL ANALYSIS OF HYDRATE DEPOSITION UNDER  
MULTIPHASE FLOW CONDITIONS**

**Análise experimental da deposição de hidratos em condições de escoamento  
multifásico**

Tese apresentada como requisito para a obtenção do título de Doutor em Engenharia Mecânica, do Programa Pós-Graduação em Engenharia Mecânica e de Materiais da Universidade Tecnológica Federal do Paraná (UTFPR). Área de concentração: Engenharia Térmicas.

Advisor: Prof. Dr. Rigoberto Eleazar Melgarejo Morales  
Co-Advisor: Prof. Dr. Amadeu Kun Wan Sum

**CURITIBA**

**2023**



Esta licença permite compartilhamento, remixe, adaptação e criação a partir do trabalho, mesmo para fins comerciais, desde que sejam atribuídos créditos ao(s) autor(es). Conteúdos elaborados por terceiros, citados e referenciados nesta obra não são cobertos pela licença.



**Ministério da Educação  
Universidade Tecnológica Federal do Paraná  
Campus Curitiba**



DANIELA CAROLINA MARQUES

**EXPERIMENTAL ANALYSIS OF HYDRATE DEPOSITION UNDER MULTIPHASE FLOW CONDITIONS**

Trabalho de pesquisa de doutorado apresentado como requisito para obtenção do título de Doutor Em Engenharia da Universidade Tecnológica Federal do Paraná (UTFPR).  
Área de concentração: Engenharia Térmica.

Data de aprovação: 29 de Maio de 2023

Dr. Rigoberto Eleazar Melgarejo Morales, Doutorado - Universidade Tecnológica Federal do Paraná

Dra. Ana Cameirao, Doutorado - Ecole Superieure de Mines de Saint-Etienne

Dr. Fabio Alencar Schneider, Doutorado - Faculdades Integradas do Brasil (Unibrasil)

Dr. Marcos Lucio Corazza, Doutorado - Universidade Federal do Paraná (Ufpr)

Dr. Moises Alves Marcelino Neto, Doutorado - Universidade Tecnológica Federal do Paraná

Documento gerado pelo Sistema Acadêmico da UTFPR a partir dos dados da Ata de Defesa em 09/02/2024.

## **ACKNOWLEDGEMENTS**

I would like to convey my gratitude and respect to my advisors, Prof. Dr. Rigoberto E. M. Morales and Prof. Dr. Amadeu Sum, for their guidance, support and comments during the development of this work.

I am very grateful to all the professors of the Mechanical Engineering Post-Graduation course at UTFPR (Federal University of Technology – Paraná) for the opportunity to learn from their knowledge.

I want to thank NUEM – Multiphase Flow Research Center and UTFPR for the welcome, support and infrastructure.

I also thank all colleagues and collaborators of the NUEM for all the support given to this work.

I wish to extend my thanks to all UTFPR collaborators and other staff as they contributed to a clean, safe and friendly environment.

A special thanks to all my friends from Centro Cultural Igaraçu for the human, cultural and spiritual formation, but mainly for their friendship.

Finally, but not lesser important, an immense thank you to all my family members and friends for always being there.

I thank God above and beyond all things.

## RESUMO

Um dos desafios durante a produção de óleo e gás em águas profundas é a formação e acúmulo de hidratos ao longo da linha de escoamento, visto que isso pode causar o comprometimento da produção ou bloqueio do duto, levando a perdas de receita (lucros cessantes) e ameaçando a integridade estrutural do sistema. Historicamente, a formação de hidratos em operações marítimas tem sido evitada por meio de aquecimento, isolamento ou injeção de inibidores termodinâmicos. No entanto, essas abordagens podem ser ineficientes e envolvem custos elevados; por isso, a indústria tem passado da prevenção de hidratos para estratégias de gerenciamento de hidratos, que permitem a formação de hidratos enquanto evitam seu acúmulo. Nesse contexto, uma sólida compreensão dos mecanismos de formação e acúmulo de hidratos é fundamental para a implementação segura de estratégias de gerenciamento de hidratos. Com esse fim, a interdependência das condições de escoamento multifásico e o processo de formação e acúmulo de hidratos foi investigada em uma célula de balanço de alta pressão com janelas de visualização. Vários experimentos foram realizados sob diferentes condições de sub-resfriamento, gradiente de temperatura, carregamento de líquido e corte de água a fim de analisar a influência desses parâmetros no mecanismo de formação, deposição na parede e aglomeração de hidratos. Foram consideradas duas composições de sistemas diferentes: água/gás e água/hidrocarboneto líquido/gás. Para focar na deposição de hidrato na parede, um gradiente de temperatura dentro da célula de balanço foi forçado a fim de promover a deposição na parede superior. Fenômenos como aglomeração, deposição, desprendimento e esfoliação de hidratos foram identificados. A filmagem dos experimentos permitiu a identificação das condições de escoamento antes e depois do início da formação de hidratos e do modelo fenomenológico do processo de formação e acúmulo de hidratos sob condições de escoamento multifásico. Verificou-se que a hidrodinâmica do sistema antes do início da formação de hidratos impacta o processo de acumulação de hidratos. As condições de escoamento promovem a dispersão das fases e conseqüentemente influenciam na localização dos depósitos de hidratos. Os resultados sugerem que a presença de uma fase de água livre após o início da formação de hidratos representa sérias preocupações em linhas de escoamento em termos de transportabilidade e formação de plugues, pois favorece a deposição de hidratos na parede, independentemente da quantidade de água e gás consumidos, bem como da presença ou ausência de uma fase oleosa. Esses resultados podem ajudar no desenvolvimento de estratégias de gerenciamento de hidratos, bem como na melhoria dos modelos de escoamento multifásicos com formação de hidratos, contribuindo para aumentar a segurança operacional e a otimização de campo.

Palavras-chave: garantia de escoamento; deposição de hidrato; hidrato de gás; célula de balanço.

## ABSTRACT

One of the challenges faced during deep-water oil and gas production operations is the hydrate formation and accumulation throughout the flowline since it may cause either production impairment or pipeline blockage, leading to temporary revenue losses, whilst threatening the system's structural integrity. Historically, hydrate formation in offshore operations has been prevented through heating, insulation or injection of thermodynamic inhibitors. However, these approaches might be inefficient and involve high costs; thence, the industry has been moving from hydrate avoidance towards hydrate management strategies, which allow hydrate formation whilst preventing its accumulation. In this context, a solid understanding of hydrate formation and accumulation mechanisms is key to safely implementing hydrate management strategies. For this purpose, the interdependence of multiphase flow conditions and the process of hydrate formation and accumulation was investigated in a high-pressure rock-flow cell with viewing windows. Several experiments were performed under different conditions of subcooling, temperature gradients, liquid loadings and water contents to analyse the influence of these parameters on the mechanism of hydrate formation, wall deposition and agglomeration. Two different system compositions were considered: water/gas and water/liquid hydrocarbon/gas. To focus on hydrate wall deposition, a gradient temperature inside the rocking cell was forced to promote upper wall deposition. Phenomena such as hydrate agglomeration, wall deposition, sloughing and washing were identified. The footage of the experiments allowed the identification of the flow conditions before and after the beginning of the hydrate formation and the development of a phenomenological model for the process of hydrate formation and accumulation under multiphase flow conditions. It was found that the hydrodynamics of the system before the beginning of the hydrate formation impacts the hydrate accumulation process. The flow conditions promote the dispersion of the phases and consequently influence the location of the hydrate deposits. These findings suggest that the presence of a free water phase after the beginning of the hydrate formation represents severe concerns in flowlines in terms of transportability and plug formation as it favours the hydrate wall deposition no matter the amount of water and gas consumed, as well as the presence or absence of an oil phase. These outcomes might help in the development of hydrate management strategies as well as in the improvement of multiphase hydrate flow models, contributing to increasing operational safety and field optimisation.

Keywords: flow assurance; hydrate deposition; gas hydrate; rock-flow cell.

## LIST OF FIGURES

Figure 2.1— Clathrate hydrate structures. Structure I consists of 46 molecules of water forming two types of cavities in the proportions of 2:6; the first has a tetradecahedron with pentagonal faces ( $5^{12}$ ) and the other a hexagonal truncated trapezohedron ( $5^{12}6^2$ ). Structure II comprises 136 water molecules forming two types of cavities in the proportion of 16:8. Structure H consists of 34 water molecules forming three types of cavities in the proportion of 3:2:1.....	29
Figure 2.2— Representation of contact angle and surface tension among liquid, gas and solid surface.....	31
Figure 2.3— Illustration of the forces presents in the rock-flow cell (a) before and (b) after the onset of the hydrate formation. Subscripts i, WL, WG, GL, MBL and SBL refer to shear stress ( $\tau$ ), specific weight ( $\rho g$ ) and velocity ( $V$ ) acting on the interface, wall-liquid, wall-gas, gas-liquid, moving bed layer and stationary bed layer, respectively.	32
Figure 2.4 – Adhesive force measurement between ice and carbon steel near the melting point. ....	33
Figure 2.5 – Tetrahydrofuran (THF)-water droplet being absorbed when brought into contact with hydrate-coated steel. ....	34
Figure 2.6 – Mechanisms of water migration to the deposition surface. ....	35
Figure 2.7 – Conceptual hydrate formation and accumulation model in a shear-stabilised dispersion. ....	41
Figure 3.1— Rock-flow cell with visualisation capabilities and cylindrical shape. ....	47
Figure 3.2— Rock-flow cell system with six front viewing windows. ....	48
Figure 3.3— Schematic of the setup of the rock-flow cell apparatus with six front viewing windows.....	49
Figure 3.4— Rock-flow cell system with two viewing windows. ....	51
Figure 3.5— Schematic of the setup of the rock-flow cell apparatus with four front viewing windows.....	52
Figure 3.6— Hydrate equilibrium condition for water and pure methane and for water and a gas mixture composed of 74.7mol% methane and 25.3mol% ethane. ....	57
Figure 4.1— General pressure and temperature variations trends over time for experiments conducted under isochoric conditions. Stage I is the time required for liquid/gas solubility. Stage II is the beginning of experiment #24 (40 %vol. LL and 18.75 rpm). At stage III, the system remains inside the hydrate formation region without visible hydrate formation. Stage IV represents the end of the experiment, which occurred approximately 48 hours after the beginning of the hydrate formation. ....	66

Figure 4.2— Captured images of the rock-flow experiments showing the highest liquid level in each window before the onset of the hydrate formation. a) Water never touches the upper wall of windows 1 and 2 (experiment #18, 20 %vol. LL and 11.25 rpm). b) Water partially touches the upper wall of window 1, but does not touch window 2 (experiment #13, 20 %vol. LL and 18.75 rpm). c) Water completely touches the upper wall of window 1, but does not touch window 2 (experiment #27, 40 %vol. LL and 11.25 rpm). d) Water touches all walls of the rock-flow cell (experiment #36, 60 %vol. LL and 11.25 rpm). ..... 69

Figure 4.3— Classification of the wet perimeter for the gas-water system based on liquid loading and oscillation rate in the rock-flow cell before the onset of the hydrate formation. In the legend, rhombic symbols mean that all windows were wetted during the motion. Triangular symbols: the water phase does not touch the upper wall of the window 2. Circular symbol: the bottom of all windows was wetted except window 4. Squared symbols: the upper wall of the edge windows was wetted (windows 1 and 3). Solid symbols represent methane/ethane gas mixture, whereas hollow symbols represent methane gas experiments. .... 70

Figure 4.4— Illustration of a gas-water flow map in the rock-flow cell before the onset of the hydrate formation as a function of the liquid loading and of the oscillation rate. The categorisation was based on the footage of the rock-flow cell experiments. .... 71

Figure 4.5— Captured images of the rock-flow cell experiments taken 48 hours after the beginning of the hydrate formation showing the final hydrate morphology: a) experiment #20 (20 %vol. LL and 06 rpm) presents a bottom wall deposit, b) experiment #25 (40 %vol. LL and 11.25 rpm) shows a plug formation at the edges of the rock-flow cell, c) experiment #39 (60 %vol. LL and 06 rpm) show a thicker upper wall deposit with some unconverted water at the bottom..... 75

Figure 4.6— Final hydrate morphology as a function of liquid loading and oscillation rate based on a characteristic gas-water flow map for rock-flow cell experiments. The captured images at three different positions of the rock-flow cell — side window — (window 4), left front window (window 1), and window 2 (window 2) were the basis for the categorisation. .... 76

Figure 4.7— Images captured before the onset of the hydrate formation a) of experiment #28 (40 %vol. LL and 06 rpm), at the beginning of the hydrate formation b), hydrates adhered to the wall c), after the first wave due to the oscillation of the rock-flow cell d), second wave e), third wave f), 140 and 200 seconds after the beginning of the hydrate formation g) and h), respectively..... 78

Figure 4.8— Illustration of the process of hydrate particle attachment to the wall observed during the experiments: a) hydrate particles in the bulk; b) hydrate particles, which have collided with the wall due to the motion of the cell, adhered to the pipe wall because of the formation of a liquid bridge; c) the retraction of the liquid phase favours the consolidation of the liquid bridge on the wall; d) hydrate deposits being wetted by the second wave of the flow; e) the retraction of the liquid phase causes the growth of the deposit because of the contact with hydrate formers and the adhesion of the hydrate particles that were floating in the bulk; f-g) the motion of the cell continues to bring hydrate formers and hydrate particles to the surface of the deposit which grows



continuously; h) formation of thicker hydrate deposits at the end. The illustration of the process of hydrate formation and accumulation was restricted to one of the windows of the rock-flow cell (window 2). The dotted line represents the previous gas-liquid interface before the contraction of the flow due to the motion of the rock-flow cell. .. 80

Figure 4.9— Description of the particle deposition process on the wall called wave effect. a) particles dispersed into the bulk; b) collision of the particle against the wall; c) contraction of the flow whereas the particle remains attached to the wall because of the liquid bridge formed on the particle interface, wall and gas phase; d) consolidation of the liquid bridge forming the first layer of the deposit; e) the liquid-phase wets the surface of the deposit once again providing water and new particles which are dispersed into the bulk; f) new particles adhere to the deposit and that may or may not consolidate; g), h) deposit growth due to the crystallisation of the water provided by the flow, conversion of the water trapped inside the porous hydrate particle and the attachment of new particles; i) eventually, the flow motion can wash particles out of the deposit if they are not consolidated and depending on the shear rate..... 82

Figure 4.10— Illustration of a sloughing event and the forces involved in the mechanism. a) forces presented in the hydrate deposit structure and b) sloughing event..... 84

Figure 4.11— Photos from the experiment #10 (50 %vol. LL and 18.75 rpm) showing the rock-flow cell before the sloughing events (a), two consecutive sloughing events (b, c) with time between shots of 2 and 26 seconds after the beginning of the hydrate formation. The red arrow shows the window where the rupture of the hydrate deposit occurred. The red rectangle highlights the window where the plug formation occurred. .... 85

Figure 4.12— Pressure (a), temperature (b) and water converted (c) into hydrate of experiment #10 (50 %vol. LL and 18.75 rpm). a) the red line is the pressure of the system, which drops as the temperature decreases and gas is consumed to form hydrates; the green line represents the hydrate equilibrium pressure under the same conditions; b) the temperature of the system (purple), hydrate equilibrium temperature (green) and subcooling (yellow), the difference between purple and green lines; c) amount of water converted to hydrates during the experiment. The vertical dashed lines, I to IV, refer to specific events related to hydrate formation and accumulation observed throughout the experiment. .... 86

Figure 4.13— Illustration of the annealing process in the hydrate deposit..... 87

Figure 4.14— Photos of experiment #27 (40 %vol. LL and 11.25 rpm) showing the annealing process of the hydrate deposit on windows 2 (a, b) and 1 (c, d). The photos were captured 24 hours (the leftmost figures) and 48 hours (the rightmost figures) after the onset of the hydrate formation. The dotted line in a) and c) shows the height of the deposit after 24 hours (b and d, respectively)..... 88

Figure 4.15— Illustration of the formation of a transportable hydrate slurry..... 89

Figure 4.16— Photos from the experiment #11 (50 %vol. LL and 18.75 rpm) where a transportable hydrate slurry was formed..... 89

Figure 4.17— Illustration of the thicker hydrate deposit a) with and b) without a free water film observed at the end of some experiments..... 90

Figure 4.18— Photos of experiment #31 (60 %vol. LL and 18.75 rpm): a) showing the thicker hydrate deposit with a free water film and experiment #32 (60 %vol. LL and 18.75 rpm) and b) without the free water film..... 90

Figure 4.19— Conceptual model of hydrate formation and accumulation in the water-continuous system as a function of time considering a slug flow pattern. The illustration reflects the impact of the slug flow pattern on the growth of the deposit: system condition before the beginning of the hydrate formation; the onset of the hydrate formation on the gas-water interface; hydrate particles stick to the wall surface because of the liquid bridge formed and consolidated; the intermittent passage of the flow causes the collision of hydrate particles which were floating in the flow and continuously expose the surface of the deposit to hydrate-forming compounds (water and gas) eventually causing the growth of the deposit. .... 91

Figure 4.20— A three-phase system. The black dashed line represents the equilibrium condition for the water and gas system, and the red continuous line represents the equilibrium condition for the gas and hydrate phases..... 94

Figure 4.21— Pressure, temperature and water converted to hydrate of experiment #25 (40 %vol. LL and 11.25 rpm). The red line is the pressure of the system which drops as the temperature decreases and gas is consumed to form hydrates. The temperature of the system (purple), hydrate equilibrium temperature (green) and subcooling (yellow) — difference between purple and green lines. The blue line is the amount of water converted to hydrates during the experiment. The vertical dashed lines refer to: gas solubility in the liquid phase (region I), the system temperature decrease to the experimental temperature (region II), system conditions are inside the hydrate equilibrium curve (region III) without visible hydrate formation, the onset of the hydrate formation (region IV). .... 95

Figure 4.22— Water converted to hydrates for 30 %vol. LL of water and gas methane as the gas phase at different experimental temperatures and 18.75 rpm (except experiment #1, which was performed at 11.25 rpm)..... 96

Figure 4.23— Water converted to hydrates for 40 %vol. LL of water and gas methane as the gas phase at different experimental temperatures..... 96

Figure 4.24— Water converted to hydrates for 50 %vol. LL of water and gas methane as the gas phase at different experimental temperatures..... 98

Figure 4.25— Water converted to hydrates for 20 %vol. of water and methane/ethane gas mixture system under different temperatures and oscillation rate conditions. .... 98

Figure 4.26— Water converted to hydrates for 40 %vol. of water and methane/ethane gas mixture systems at different temperatures and oscillation rate conditions. .... 99

Figure 4.27— Water converted to hydrates for 60 %vol. of water and methane/ethane gas mixture systems under different temperatures and oscillation rate conditions. 100

Figure 4.28— Photos showing the process of hydrate formation and accumulation under static conditions for 60 %vol. of LL and upper wall temperature at around 4oC and bottom wall temperature at about 10oC: a) before the onset of the hydrate formation; b) the onset of the hydrate formation on the gas-liquid interface; c) 13 hours after the onset of the hydrate formation, a layer of hydrates is observed in the bulk (red bracket) and a thin hydrate layer on the upper wall (red arrow); d) the oscillation of the rock-flow cell begins, showing the consolidation of hydrates on the wall; e) the contraction of the flow, due to the motion, drags particles that deposit on the wall. The photos are from windows 4 and 2. .... 103

Figure 4.29— The photos show the hydrate formation and accumulation process when the rock-flow cell stops at 11o. a) before the onset of the hydrate formation; b) the onset of the hydrate formation on the gas-liquid interface; c) 15 hours after the onset of the hydrate formation, a layer of hydrates is observed in the bulk and a thin hydrate layer forms on the upper wall (window 4); d) shortly after the start of the rotation of the rock-flow cell at 2 rpm; e) the flow carries the particles that shall consolidate on the wall; f) end of the experiment twelve hours after. The photos are from windows 4 and 2. .... 104

Figure 4.30— Classifications of wall deposition and bedding mechanism for flow risk analysis of gas-hydrate-water systems. Blue represents the water phase; green is the gas phase; white is the hydrate deposits or particles. The background colours (green, yellow and red) were used to facilitate risk identification. The circle shape represents the view of the cross-section area, and the rectangular shape represents the length of the cell. .... 107

Figure 4.31— Photos of the classification for wall deposition and bedding mechanisms according to flow risk criterion for gas-hydrate-water systems. The red arrow indicates that the bulk phase is in constant motion. .... 109

Figure 5.1— The oil-gas-water flow images observed before the onset of the hydrate formation throughout the experiments: a) water phase dispersed in the oil-continuous phase (experiment #63, 80 %vol. LL and 20%vol. WC). b) a thicker free water layer with a dispersed water and oil phase (experiment #68, 80 %vol. LL and 70%vol. WC). c) a water-free phase at the bottom, an intermediate layer of dispersed water and oil, and an oil phase above (experiment #66, 80 %vol. LL and 45%vol. WC). d) a dispersed water and oil phase at the bottom and an oil phase above (experiment #49, 40 %vol. LL and 45%vol. WC). .... 120

Figure 5.2— Illustration of an oil-gas-water flow map for 40 %vol. of liquid loading in the rock flow cell before the onset of the hydrate formation as a function of water content and oscillation rate. The categorisation was based on the footage considering what happens in the middle of the rock-flow cell. .... 121

Figure 5.3— Illustration of an oil-gas-water flow map for 60 %vol. of liquid loading in the rock flow cell before the beginning of the hydrate formation as a function of water content and oscillation rate. The categorisation was based on the footage considering what happens in the middle of the rock-flow cell. .... 122

Figure 5.4— Illustration of an oil-gas-water flow map for 80 %vol. of liquid loading in the rock flow cell before the beginning of the hydrate formation as a function of water content and oscillation rate. The categorisation was based on the footage considering what happens in the middle of the rock-flow cell..... 123

Figure 5.5— Illustration of an oil-gas-water flow map in the rock flow cell before the onset of the hydrate formation as a function of liquid loading and water content. The categorisation was based on the footage considering what happens in the middle of the rock-flow cell and the velocities analysed. .... 124

Figure 5.6— Photos of experiment #49 (letters a and b, 40 %vol. LL, 45 %vol. WC and 18.75 rpm) and #54 (letters c and d, 40 %vol. LL, 70 %vol. WC and 18.75 rpm). a) water and oil dispersion with a thin oil layer at the top before the beginning of the hydrate formation. b) phase separation before hydrate is visually observed by the naked eye. c) two liquid phases before the onset of the hydrate formation: a water and oil dispersion above a water layer. d) dispersed flow after the hydrate formation onset. .... 126

Figure 5.7— Photos of experiment #66 (80 %vol. LL, 45 %vol. WC and 18.75 rpm) showing the system's dispersion before the onset of the hydrate formation, the phase separation at the beginning of the hydrate formation followed by the formation of a dispersion. The photos show a) the system before the beginning of the hydrate formation; b) phase separation of the liquid phases, although hydrate formation is not visually observed by the naked eye (5 seconds after the picture of letter a); c) formation of an intermediate phase between the oil and water phases after the beginning of the hydrate formation (the photo was taken 35 seconds after the previous image, letter b); d) a slurry is observed 45 seconds from the previous image (letter c)..... 127

Figure 5.8— Illustration of the process of hydrate formation for low water content (< 20%vol.) and for low to medium liquid loading (40 to 60 %vol. LL): a) flow characteristic before the onset of the hydrate formation, stratified wavy oil and water layer with a thin layer of dispersed water above a thin water film; b) the onset of the hydrate formation with hydrate particles flowing in the bulk; c) collision of hydrate particles forms agglomerates; d) the agglomerates settles and consolidates on the bottom of the cell with no free water available in the system. .... 129

Figure 5.9— Illustration of the process of hydrate formation for middle water content (20 to 45 %vol.) and for low to medium liquid loading (40 to 60 %vol. LL): a) flow characteristic before the onset of the hydrate formation, an oil layer at the top, a dispersed layer of water in oil, and a water-free phase at the bottom; b) the onset of the hydrate formation with hydrate particles flowing dispersed in the bulk as a slurry forming a stabilised dispersed phase (water-oil-hydrate phase); c) hydrate particles adhered to the pipe wall; d) a thin layer of hydrate deposit is created on the laterals of the cell; e) hydrate deposit growth in the presence of a flowable hydrate slurry; f) the liquid phase dries out. The oil phase and the remaining water in the system were trapped inside the porous hydrate deposits on the bottom of the cell. .... 130

Figure 5.10— Illustration of the process of hydrate formation for high water content (> 45 %vol.) and low to middle liquid loading (40 to 60 %vol. LL): a) flow characteristic before the onset of the hydrate formation, a dispersed layer of water in oil with a water

layer at the bottom; b) the onset of the hydrate formation with hydrate particles flowing dispersed in the bulk forming a stabilised dispersed phase (water-oil-hydrate phase); c) hydrate particles adhered to the pipe wall; d) the preferred region for hydrate deposition is the upper one because of the lower flow energy; e) the hydrate deposit is constantly wetted because of the tilting of the cell forming a thicker hydrate deposit few minutes (< 30 min) after the onset of the hydrate formation. Because of the high volume in the system, a water-free or oil phase can be observed at the end of some experiments. This behaviour is similar to the 100% of water content (oil-free) experiments. .... 131

Figure 5.11— Illustration of the process of hydrate formation for high liquid loading (> 80 %vol. LL): a) flow characteristic before the onset of the hydrate formation, a dispersed layer of water in oil with a water layer at the bottom; b) the onset of the hydrate formation with hydrate particles flowing dispersed in the bulk, forming a stabilised dispersed phase (water-oil-hydrate phase); c) some hydrate particles adhered to the pipe wall and some hydrate particles float in the bulk; d) hydrate deposits start forming on the laterals, whereas agglomerates start forming in the bulk; e) the upper hydrate deposit is constantly wetted due to the motion of the cell forming a thicker hydrate deposit whereas the agglomerates settle forming a bed and later a bottom deposit. This behaviour may represent a hybrid region with two fundamental mechanisms: wave effect and agglomeration. .... 132

Figure 5.12— Illustration of final hydrate morphology as a function of the liquid loading and the water content based on the characteristic oil-gas-water flow map for rock-flow cell experiments. The captured images at three different positions of the rock-flow cell were the basis for the general categorisation. In region I, hydrate agglomeration is the primary mechanism of accumulation. In region II, the liquid phase dried up, indicating that part of the fluid was trapped in the lower porous hydrate structure. Region III is dominated by the hydrate deposition. Region IV is a hybrid region where hydrate wall deposition and agglomeration followed by settling are presented. .... 133

Figure 5.13— Captured images of the rock-flow cell: a) experiment #57 (60 %vol. LL, 20 %vol. WC and 11.25 rpm) representing the conditions for low water content and low to medium liquid loading system, b) experiment #47 (40 %vol. LL, 45 %vol. WC and 11.25 rpm) representing the conditions for middle water content (20 to 45 %vol.) and for low to medium liquid loading (40 to 60 %vol. LL, c) experiment #58 (60 %vol. LL, 70 %vol. WC and 18.75 rpm) representing the conditions for high water content (> 45%vol.) and low to middle liquid loading (40 to 60 %vol. LL), d) experiment #69 (80 %vol. LL, 70 %vol. WC and 11.25 rpm) representing the conditions for high liquid loading (> 60 %vol. LL). .... 135

Figure 5.14— Description of the process of particle aggregation, cristallisation and agglomeration, which leads to the formation of a bedding layer or hydrate deposits on the bottom of the pipe. a) particles dispersed into the bulk; b) collision of the particle against another particle; c) the particle remains attached because of the capillary bridge formed on the particle surface, oil and gas phases; d) cristallisation of the capillary bridge forming the first agglomerate; e) if the motion of the rock-flow cell does not provide enough force to lift the agglomerate, the agglomerate settles forming a moving bedding at the bottom; f) the agglomerate may consolidate at the bottom forming a deposit. .... 138

Figure 5.15— Description of the particle deposition process on the wall, called wave effect, for gal-oil-water systems, which leads to the formation of hydrate deposits. a) hydrate particle dispersed into the bulk; b) collision of the particle against the wall; c) contraction of the flow, whereas the particle remains attached to the wall because of the liquid bridge formed on the particle surface, wall and gas phases; d) consolidation of the liquid bridge forming the first layer of the deposit; e) the motion of the rock-flow cell wets the surface of the deposit once again providing water, oil and new particles which are dispersed into the bulk; f) new particles adhere to the deposit and may or may not consolidate; g), h), i) eventually, the flow can wash particles out of the deposit if they are not consolidated (time-dependent) and depending on the shear rate. ... 140

Figure 5.16— Description of the process of particle deposition on the wall and agglomeration followed by settlement for the hybrid region in an oil-gas-hydrate-water system, which leads to pipe cross-section reduction. a) hydrate particle dispersed into the bulk; b) collision of the particle against the wall and another particle; c) contraction of the flow whereas the particle remains attached to the wall because of the liquid bridge formed on the particle surface, wall and gas phase, and particle-particle capillary bridge formed on the particle, oil, water interface; d) cristallisation of the liquid bridge forming the first layer of the deposit on the wall and cristallisation of the capillary bridge forming an agglomerate in the bulk; e) the motion of the rock-flow cell wets the surface of the deposit once again providing water, oil and new particles which were dispersed into the bulk and eventually the agglomerates settled, establishing a bedding layer in the cases where the flow energy is not enough to lift the agglomerates; f) the wall deposits grow, and the size of the agglomerates increases whilst the hydrate particles are water-wet, and eventually, the bedding layer can become a deposit. 142

Figure 5.17— Photo from experiment #70 (80 %vol. LL, 70 %vol. WC, 18.75 rpm) showing the detachment of the upper hydrate deposit: the imminence of the sloughing event (left) and right after it has occurred (right). ..... 144

Figure 5.18— Photos of experiment #63 (80 %vol. LL, 20 %vol. WC, 18.75 rpm). a) hydrate bottom and upper wall deposit after 30 min from the onset of the hydrate formation; b) screenshot from 3h40 of the onset of the hydrate formation, the flow energy detaches chunks from the bottom wall deposit, and the hydrate particles in the flow eventually attach to the upper wall deposit; c) 48 hours after the onset of the hydrate formation, a solid hydrate deposit was formed on the upper wall, and the oil phase flows freely. .... 145

Figure 5.19— Photo from experiment #42 (40 %vol. LL, 20 %vol. WC, 18.75 rpm) exhibiting the agglomerates formed 5 minutes after the onset of the hydrate formation (left) and the hydrate slurry with an upper wall deposit formed after the beginning of the hydrate formation (right). ..... 146

Figure 5.20— Water converted to hydrates over time for the oil-gas-hydrate-water experiments with 40 %vol. of liquid loading at different water contents, oscillation rates and under subcooling conditions. .... 148

Figure 5.21— Water converted to hydrates over time for the oil-gas-hydrate-water experiments with 60 %vol. of liquid loading at different water contents, oscillation rates and under subcooling conditions. .... 149

Figure 5.22— Water converted to hydrates over time for the oil-gas-hydrate-water experiments with 80 %vol. of liquid loading at different water contents, oscillation rates and under subcooling conditions. ....	149
Figure 5.23— Amount of water converted to hydrates over time. a) for 40 %vol. systems; b) for 60 %vol. systems; c) for 80 %vol. systems. The curves were grouped by rate of conversion and water content. The average water converted to hydrates is denoted by bold lines, and the shaded areas are the regions of deviation values..	150
Figure 5.24— Classification of hydrate mechanisms for flow risk analysis of oil-gas-water systems. The brown colour represents the liquid phase. Green characterises the gas phase, and white symbolises the hydrate deposits or particles. The background colours (green, yellow and red) were used as a method to facilitate risk assessment. ....	151
Figure 5.25— Photos of the classification for aggregation, wall deposition and bedding mechanisms according to flow risk criterion for oil-gas-hydrate-water systems. The red arrow indicates that the bulk phase is in motion. The aggregation and wall deposition show photos from the side view of the rock-flow cell and the bedding from the front views.....	153
Figure 6.1— Flowchart of the process of hydrate formation and accumulation in an oil-gas-hydrate-water system.....	163

## LIST OF TABLES

Table 2.1— Syntheses of some studies on hydrate formation and accumulation.....	43
Table 3.1— Specifications of the experimental equipment. ....	50
Table 3.2— Specification of the mineral oil.....	56
Table 3.3— Experimental grid of the rock-flow cell.....	57
Table 4.1— Summary of experiments performed with the respective measured data, estimated water converted and flow risk analysis for fresh water and gas systems.	63
Table 4.2— Flow risk analysis for water and methane systems. Grade 0 represents a pass condition, grade 1 is a moderate condition, and grade 2 is a fault condition. The maximum flow risk index is 8 indicating a high risk of flow disruption. The first column represents the analysis after 5 minutes of the beginning of the hydrate formation and the other at the end of the experiment. ....	109
Table 4.3— Flow risk analysis for water and methane/ethane gas mixture systems. Grade 0 represents a pass condition, grade 1 is a moderate condition, and grade 2 is a fault condition. The maximum flow risk index is 8 indicating a high risk of flow disruption. The first column represents the analysis after 5 minutes of the beginning of the hydrate formation and the other at the end of the experiment. ....	110
Table 5.1— Experimental data summary for fresh water, mineral oil, gas mixture and gas hydrate systems with the respective measured data at the onset of the hydrate formation, estimated amount of water converted to hydrate and flow risk index.....	117
Table 5.2— Flow risk analysis for oil-gas-hydrate-water systems. Grade 0 represent a pass condition, grade 1 is a moderate condition, and grade 2 is a fault condition. The maximum flow risk index is 12 indicating a high risk of flow disruption. ....	154



## LIST OF ACRONYMS

DCV	Direct current voltage
Exp.	Experiment number
GWR	Gas-water ratio
NUEM	Multiphase Flow Research Center
RTD	Resistance temperature detector
SW	Stratified wavy flow regime
sl	Hydrate structure I
sII	Hydrate structure II
TC	Thermocouple
UTFPR	Federal University of Technology – Paraná
WC	Water content

## NOMENCLATURE

### *Greek letters*

$\phi$	Contact angle	rad
$\rho$	Density	kg/m <sup>3</sup>
$\sigma$	Surface tension	N/m
$\tau$	Shear stress	Pa
$\omega$	Oscillation rate	rpm
$\Delta t$	Time between hydrates formation and the start of hydrate dissociation	h

### *Roman letters*

Aq	Aqueous phase	
ci	Compound index	
E	Error	
F	Fluid friction	N
F <sub>A</sub>	Adhesion force per unit length	N/m
F <sub>G</sub>	Gravity force	N
g	Gravitational acceleration	m/s <sup>2</sup>
G	Gas phase	
H	Hydrate phase	
i	Interfaces between heterogeneous layers	
L	Liquid phase	
LL	Liquid loading	%vol.
M	Molar mass	
m	mass	
MBL	Moving bed layer	
n	Molar amount	
SBL	Stationary bed layer	
P	Pressure	bar
S	Solid surface	

t	Time	
T	Temperature	°C
T <sub>average</sub>	Average experimental temperature	°C
v	Velocity	
V <sub>M</sub>	Molar volume	
V <sub>T</sub>	Total volume	m/s
X	Molar fraction	
w	Water phase	
W	Pipe wall	

## TABLE OF CONTENTS

<b>1. INTRODUCTION.....</b>	<b>23</b>
<b>1.1 OBJECTIVES AND MOTIVATION .....</b>	<b>25</b>
<b>1.2 STRUCTURE OF THE THESIS .....</b>	<b>27</b>
<b>2. LITERATURE REVIEW .....</b>	<b>28</b>
<b>2.1 FUNDAMENTAL CONCEPTS.....</b>	<b>28</b>
2.1.1 COHESIVE AND ADHESIVE HYDRATES FORCES.....	33
<b>2.2 HYDRATE WALL DEPOSITION .....</b>	<b>34</b>
<b>2.3 HYDRATE FORMATION AND ACCUMULATION IN GAS-HYDRATE-WATER SYSTEM.....</b>	<b>37</b>
<b>2.4 HYDRATE FORMATION AND ACCUMULATION IN OIL-GAS-HYDRATE-WATER SYSTEM.....</b>	<b>39</b>
<b>2.5 FINAL CONSIDERATIONS OF THIS CHAPTER.....</b>	<b>42</b>
<b>3. METHODOLOGY.....</b>	<b>46</b>
<b>3.1 APPARATUS DESCRIPTION .....</b>	<b>46</b>
3.1.1 ROCK-FLOW CELL WITH SIX FRONT VIEWING WINDOWS.....	46
3.1.2 ROCK-FLOW CELL WITH FOUR FRONT VIEWING WINDOWS .....	50
3.1.3 ROCK-FLOW CELL SETUPS .....	52
<b>3.2 EXPERIMENTAL PROCEDURE .....</b>	<b>53</b>
<b>3.3 MATERIALS .....</b>	<b>55</b>
<b>3.4 EXPERIMENTAL CONDITIONS.....</b>	<b>57</b>
<b>3.5 ACCURACY IN THE MEASURED DATA.....</b>	<b>58</b>

<b>4. RESULTS AND DISCUSSION OF WATER AND SYNTHETIC GAS SYSTEMS</b>	<b>61</b>
4.1 HYDRATE FORMATION IN FRESHWATER SYSTEMS .....	61
4.2 FLOW CONDITIONS BEFORE HYDRATE FORMATION ONSET .....	67
4.3 CHARACTERIZATION OF HYDRATE FORMATION AND ACCUMULATION	72
4.3.1 WAVE EFFECT.....	77
4.3.2 SLOUGHING.....	83
4.3.3 ANNEALING .....	86
4.3.4 TRANSPORTABLE HYDRATE SLURRY .....	88
4.3.5 FREE WATER FILM AT THE END OF THE EXPERIMENT .....	89
4.3.6 CONCEPTUAL MODEL OF HYDRATE FORMATION AND ACCUMULATION IN WATER-DOMINATED SYSTEM.....	91
4.4 ESTIMATION OF THE AMOUNT HYDRATE FORMED.....	92
4.5 STATIC EXPERIMENTAL CONDITIONS.....	100
4.6 FLOW RISK ANALYSIS.....	105
4.7 FINAL CONSIDERATIONS OF THE CHAPTER.....	111
<b>5. RESULTS AND DISCUSSION OF WATER, MINERAL OIL AND SYNTHETIC GAS SYSTEMS.....</b>	<b>115</b>
5.1 HYDRATE FORMATION IN FRESH WATER- MINERAL OIL- GAS SYSTEMS	116
5.2 FLOW CONDITIONS BEFORE HYDRATE FORMATION ONSET .....	119
5.3 HYDRATE MORPHOLOGY OF FORMATION AND ACCUMULATION .....	125
5.3.1 THE ONSET OF THE HYDRATE FORMATION AND STABILITY OF THE DISPERSION.....	125

5.3.2	CHARACTERIZATION OF HYDRATE FORMATION AND ACCUMULATION 127	
<b>5.4</b>	<b>MECHANISMS RELATED TO HYDRATE WALL DEPOSITION .....</b>	<b>136</b>
5.4.1	AGGLOMERATION AND SETTLING.....	137
5.4.2	WAVE EFFECT.....	139
5.4.3	HYBRID SYSTEMS.....	141
5.4.4	LONG-TIME SCALE MECHANISMS .....	143
<b>5.5</b>	<b>ESTIMATION OF THE AMOUNT OF HYDRATE FORMED.....</b>	<b>146</b>
<b>5.6</b>	<b>FLOW RISK ANALYSIS .....</b>	<b>150</b>
<b>5.7</b>	<b>FINAL CONSIDERATIONS OF THE CHAPTER.....</b>	<b>155</b>
<b>6.</b>	<b>CONCLUSIONS.....</b>	<b>158</b>
<b>6.1</b>	<b>WATER AND SYNTHETIC GAS SYSTEMS .....</b>	<b>159</b>
<b>6.2</b>	<b>WATER, MINERAL OIL AND SYNTHETIC GAS SYSTEMS .....</b>	<b>161</b>
<b>6.3</b>	<b>SUGGESTIONS FOR FUTURE INVESTIGATIONS.....</b>	<b>164</b>
	<b>REFERENCES .....</b>	<b>167</b>
	<b>APPENDIX A — PROCEDURE FOR THE ESTIMATION OF THE AMOUNT OF HYDRATE FORMED .....</b>	<b>172</b>

## 1. INTRODUCTION

The flow of mixtures with more than one thermodynamic phase is called multiphase flow. In the oil & gas industry, a production system often handles multiphase flows composed of water, oil and gas. Light components flow – partially or totally – dissolved in the liquid phase, be it water, liquid hydrocarbon, or a mixture of both, but it can also form a free gas phase. Water can be found in the emulsion, shear-stabilised dispersion or even as a condensate or a free phase. The presence of the water in the production system can be due to connate water, water influx from an aquifer or as a result of waterflooding techniques aimed at improving the oil recovery. Therefore, depending on the field characteristics and development strategies, the amount of water in the transport facilities may increase as the field matures.

The efforts and techniques ensuring that the hydrocarbons are transported economically from the reservoir to the refineries are referred to as flow assurance. One of the most well-known flow assurance challenges in offshore operations is the precipitation of solid and their deposition (scale, wax deposition, asphaltene precipitation, gas hydrates and, sometimes, sand as well). Understanding the multiphase flow behaviour when these solid particles are present is key to develop flow assurance strategies. The thermo-hydraulic flow conditions affect the transport of the fluids and they do play an important role in the process of solid precipitation and deposition.

Hydrate formation in the production system is an essential part of flow assurance studies because large amounts of solids can form immediately after hydrate formation onset, leading to production impairment and, if left untreated, to pipeline blockage. The operational procedure to remove the hydrate plugs threatens the structural integrity of the system — as during the hydrate dissociation operation, the hydrate plug can act as a projectile. In addition to the associated operational safety risks, the whole procedure can also be costly because of the removal time and production downtime. According to Freitas et al. (2002), it took six months for an injection well in the Campos basin to resume production after a gas hydrate plug had been formed, shutting the well down.

The increase in the length of the production lines as a consequence of the oil and gas explorations in increasingly deeper water depths — for example, the transport of reservoir fluids through long subsea tieback facilities — can intensify the risk of hydrate formation and flowline blockage since it is expected that the produced fluids could not retain their thermal energy, therefore approaching the external (seabed) temperature because of long residence times. Furthermore, hydrates can form as long as events such as dehydrator malfunction, inhibitor failure, temperature drops across valves or restrictions (because of the Joule-Thompson effect), and transient conditions such as shutdowns and restarts occur. The occurrence of hydrates in the production system (production tubing, flowline and riser) increases the pressure drop due to solids formation in the bulk flow, which increases fluid viscosity, and solids deposition on the inner pipe wall.

Historically, hydrate formation is prevented by flowline insulation and continuous or intermittent injection of chemical inhibitors such as methanol and glycol or low-dosage hydrate inhibitors (LDHI). All those strategies play a role in capital expenditure (CAPEX), operational expenditure (OPEX) and logistical planning. In addition, the amount of inhibitor required to keep the system inhibited might be significant in seawater operations (Sloan et al. 2011, 91–92), what might render this procedure unfeasible. In this context, the petroleum industry is moving from hydrate avoidance strategies towards risk management ones, focusing on transporting hydrates as a slurry without allowing either accumulation or wall deposition (Fossen et al., 2017). One of the advantages of allowing hydrate formation but controlling its accumulation is the elimination or reduction of the injection of chemicals into the production system, consequently reducing CAPEX and OPEX. However, it is essential to thoroughly understand the mechanism of hydrate formation and accumulation to define and quantify the risks involved in this operation.

The mechanisms of hydrate formation and accumulation in multiphase flow have been numerically studied with the purpose of creating numeric models (Song et al., 2018, Ravichandran and Daraboina, 2019, Bassani 2020); and to experimentally establish a phenomenological model through wheel flow (Vebenstad et al. 2005, Lund et al. 2008), flow loop (Dholabhai et al. 1993; Aman et al. 2016), or rock-flow cell experiments (Grasso et al. 2014; Straume 2017; Liu et al. 2021). Lachance et al. 2012



and Hatton et al. 2002 identified hydrate deposition on the inner pipe wall as the main mechanism involving loss of production due to localised build-up and hydrate plugging formation in pipelines. Understanding the hydrate deposition mechanism is key to developing hydrate management strategies.

Some factors affecting hydrate deposition are subcooling, adhesion and cohesion of hydrate particles, hydrodynamics of the system, heat and mass transfer, and fluid properties. Some studies focus on the mechanism of water migration leading to hydrate wall deposition (Grasso et al. 2014), the adhesion forces between hydrate particles and wall surfaces (Nicholas et al. 2009a), and the influence of the multiphase flow on the mechanism of hydrate deposition (Straume 2017). However, hydrate formation and accumulation in multiphase flow is still a major area of research in the oil and gas industry since lab findings are generally sensitive to the tested parameters — fluid properties, subcooling, flow conditions, presence of chemical additives, dominant flow phase — leading to an absence of an accurate and universal phenomenological model able to predict and characterise the whole behaviour of hydrate formation and evolution along the flow in different scenarios. A universal model will provide safe, reliable and cost-effective flow assurance strategies.

This work aims to enhance the knowledge on the mechanisms leading to hydrate wall deposition and subsequent plug build-up in multiphase flow. The characteristics of the hydrate formation and accumulation were studied for gas-water and oil-gas-water systems under different conditions (subcooling, shear, and water content) in a rock-flow cell. The smaller scale of the experimental apparatus allows better control of the system parameters (pressure and temperature when compared to a flow loop system, for example). Although the rock-flow cell may not reproduce the exact flow conditions of the flowlines (equivalent shear and the displacement of fluids, which is gravity-driven instead of pressure drop-driven, for example), the phenomena observed are expected to be qualitatively the same as in the flowlines.

## **1.1 Objectives and Motivation**

This work aims to broaden the knowledge about the main mechanism leading to hydrate accumulation in multiphase flow, focusing on hydrate wall deposition. To

achieve that, several experiments were carried out in a rock-flow cell for two-phase (water/gas mixtures) and three-phase systems (water/liquid hydrocarbon/gas mixtures) conditions before the onset of the hydrate formation to study the influence of subcooling, variable temperature gradient, liquid loading, water content (volume of water in the system given in percentage) and fluid compositions on the process of hydrate formation and accumulation. Amongst other findings, the present work presents:

- A study on the hydrate formation and accumulation in gas-water and oil-gas-water systems.
- A study on the main mechanisms involved in the process of hydrate wall deposition under dynamic conditions.
- An analysis on the wall temperature sensitivity to the formation of hydrate wall deposits.
- An estimation of the amount of hydrate formed, which gives some insights into the kinetic of hydrate formation and accumulation in the system.
- An observation of other hydrate phenomena, such as annealing and sloughing events, which might increase the plug formation risk in the pipeline.
- A description of a conceptual hydrate formation and accumulation model for gas-water and oil-gas-water systems.

The motivation of this study is the lack, to the best of the author's knowledge, of a consolidated model for hydrate formation and accumulation in multiphase flows. Additionally, an increase in the number of oil and gas offshore operations, which often provide favourable conditions for the formation of gas hydrates. Furthermore, the hazardous conditions posed by gas hydrate plugs and the search for cost-effective hydrate management strategy increased the interest in continued studies on hydrate formation and accumulation under dynamic conditions.

## 1.2 Structure of the thesis

This work is divided into six chapters. The first and present one, the present chapter, introduces the motivation of this work, highlighting the main objectives. Chapter 2 presents a summary of previous studies on hydrate formation and accumulation in different experimental apparatus, focusing on the studies emphasizing hydrate deposition. The main concepts (wettability of the phases, for example) addressed in the other chapters will also be reviewed.

Chapter 3 describes the experimental apparatus, the methodology used in this study, the properties of the fluids used in the experiments, the overall conditions of such experiments and a summary about the accuracy of the measured data.

In Chapter 4, the results and some conclusions observed for gas-hydrate-water systems will be presented. Such findings include: the characteristics of the flow before the beginning of hydrate formation, the morphology and the mechanism leading to hydrate wall deposition, the estimation of the amount of hydrate formed, and the flow risk index. The experiments performed at static conditions are also discussed in this chapter, given their importance in supporting the main conclusions obtained from the dynamic condition experiments.

Chapter 5 shows the findings when the system is in the presence of mineral oil. The flow conditions before the onset of the hydrate formation, and the morphology of hydrates after such onset is discussed, followed by the mechanisms involved in the process of hydrate wall deposition, the estimation of the amount of water converted to hydrates and the flow risk analysis. The final remarks and suggestions for future investigations are given in Chapters 6 and 7, respectively.

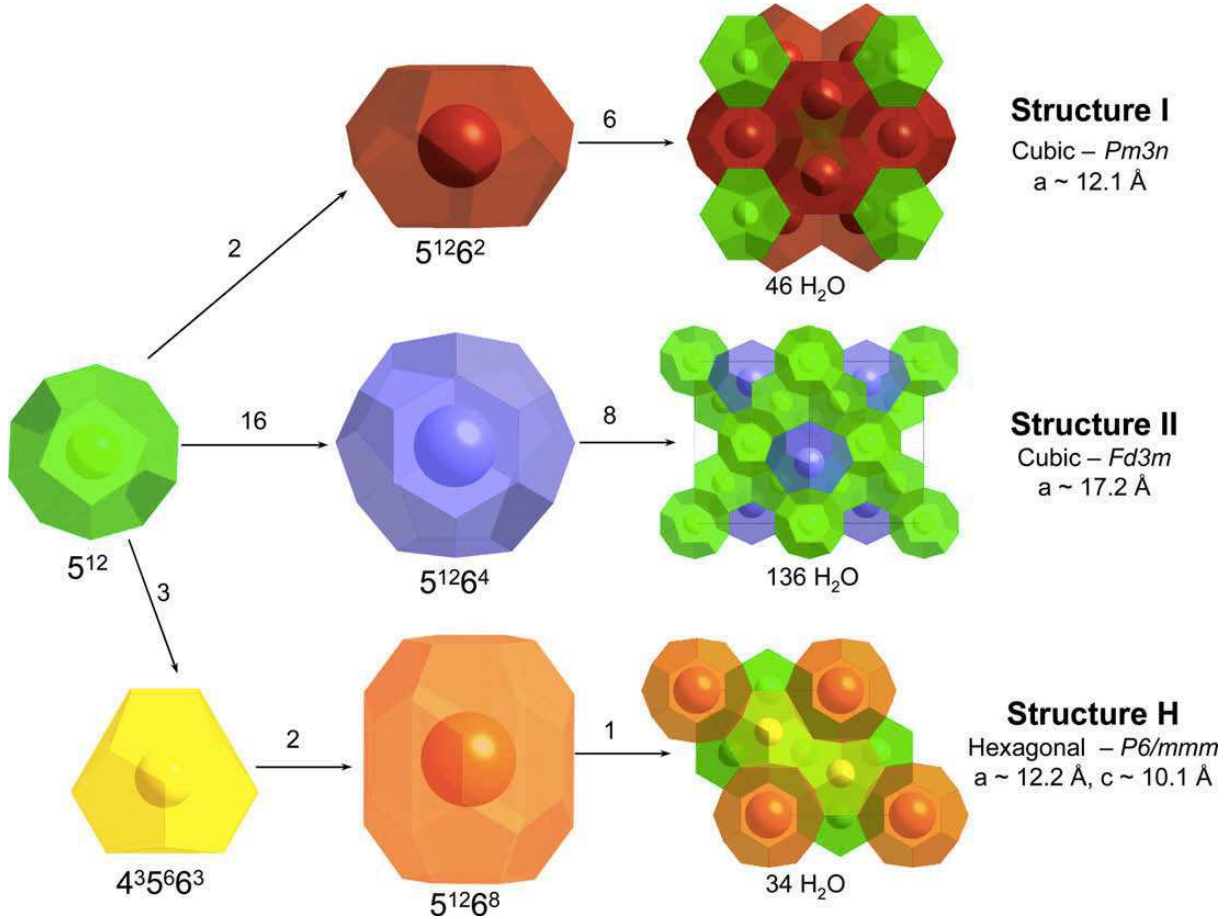
## 2. LITERATURE REVIEW

Some fundamental concepts related to gas hydrate and the scope of this thesis are presented briefly in this section. In the sequence, some relevant works published in the literature according to the investigated systems are discussed. For the sake of clarity, they were categorised into gas-hydrate-water and oil-gas-hydrate-water studies. Finally, the contributions of the present work to the literature are mentioned at the end of the section.

### 2.1 Fundamental Concepts

Clathrate hydrates, or gas hydrates, are crystalline compounds that may form depending on the temperature, pressure and presence of water and gas molecules ( $< 9 \text{ \AA}$  diameter) in the system (Sloan and Koh, 2008). There are no chemical bonds between the gas trapped inside the water cage and the water molecules; consequently, gas hydrates are not actually chemical compounds, and their formation and dissociation involve first-order phase transitions. The gas hydrate crystalline structure formed depends on the size of the gas molecules and can be defined as cubic structure I (sI), cubic structure II (sII) and hexagonal structure H (sH). Figure 2.1 shows a schematic of those gas hydrate structures.

Figure 2.1— Clathrate hydrate structures. Structure I consists of 46 molecules of water forming two types of cavities in the proportions of 2:6; the first has a tetradecahedron with pentagonal faces ( $5^{12}$ ) and the other a hexagonal truncated trapezohedron ( $5^{12}6^2$ ). Structure II comprises 136 water molecules forming two types of cavities in the proportion of 16:8. Structure H consists of 34 water molecules forming three types of cavities in the proportion of 3:2:1.



Source: Strobel et al. 2009.

In general, hydrates tend to nucleate on all gas-water interfaces as the interface reduces the Gibbs free energy of nucleation, but mainly because it is the site with the highest concentration of the compounds in relation to the bulk of either the gas or the water phase (Sloan and Koh, 2008). Generally, hydrates start forming when the temperature and the pressure of a system are above the hydrate equilibrium curve due to the metastability of the hydrate formation. The hydrate growth is mainly controlled by mass transfer.

Gas hydrates are of interest to several studies, specifically: carbon capture and storage (Rajnauth, 2013) to reduce its contribution to global warming; natural gas transportation and storage (Taheri et al., 2014) to reduce the gas flaring and pollution in offshore operations; desalination design (Sahu et al., 2018); refrigeration systems

(Zhang et al., 2017) and flow assurance strategies in offshore operations (Sloan et al., 2011; Olajire, 2020). The focus of this research is on flow assurance.

During the transport of the fluids or shutdowns, the pressure and temperature conditions of the production system may lie within the envelope of hydrate formation, producing the operational conditions necessary to form gas hydrate (presence of water, gas and adequate pressure and temperature conditions). Generally, the production fluids are oil, gas (lightweight elements of the natural gas, carbon dioxide - CO<sub>2</sub>, nitrogen - N<sub>2</sub> and hydrogen sulphide - H<sub>2</sub>S) and water (from water-saturated gas, connate water, aquifer or water injection). Hydrates may start forming when the temperature and the pressure of a system are above the hydrate equilibrium curve due to the metastability of the hydrate formation.

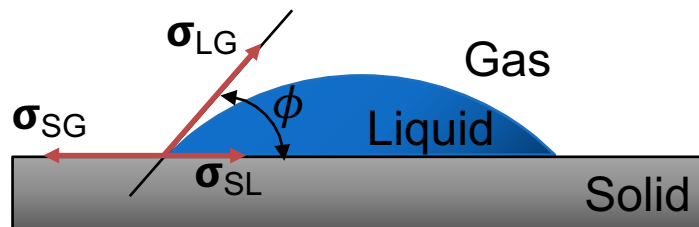
Capillary and adhesion forces, heat and mass transfer, presence of free water, flow patterns, phases and amount of the compounds present in the system are just examples of parameters that influence hydrate formation and accumulation during multiphase flow. Some fundamental works were performed to understand the influence of these mechanisms separately. The adhesion and cohesive forces between a hydrate particle and the wall (Nicholas et al., 2009a) and amongst hydrate particles (Aman et al., 2011), for example. The gas hydrate adhesion and cohesive forces is influenced by the temperature.

This study highlights the influence of flow conditions before hydrate formation since it evidences the water-wetted surfaces that will subsequently influence on the location of the hydrate deposit. In the present work, no studies with salt water were carried out, which according to Aspenes et al. (2008) may reduce the hydrate wall deposition. The authors studied the influence of the wettability of solid surfaces on the hydrate deposition mechanism for the following materials: stainless steel, aluminium, brass, glass, quartz and two epoxy-coated surfaces. They have concluded that increasing acid concentration decreased adhesion energy, and the contact angles of water drops moved towards more oil-wet conditions, reducing the possibility of hydrate deposition.

The wettability is associated to the tendency of the liquid to spread or not in a solid surface, and is assessed by the angle of contact of a droplet of liquid with a solid surface in the presence of another immiscible phase, for example gas-liquid-solid

contact. This way, the molecules of a liquid are exposed to the solid surface with no neighbouring molecules in all directions. The bottom molecules pull the others giving rise to internal pressure, and the shape of the drop will be determined by the surface tension of the liquid as the liquid contracts its surface area to maintain the lowest free surface energy. The greater the contact angle, the more the liquid moistens the solid surface in contact; in other words, the greater the wettability will be. Figure 2.2 shows an illustration of a liquid droplet in contact with a solid surface, where  $\phi$  is the contact angle,  $\sigma_{LG}$  the surface tension between liquid and gas,  $\sigma_{SG}$  surface tension between solid and gas, and  $\sigma_{SL}$  the surface tension between the solid and the liquid surfaces.

Figure 2.2— Representation of contact angle and surface tension among liquid, gas and solid surface.



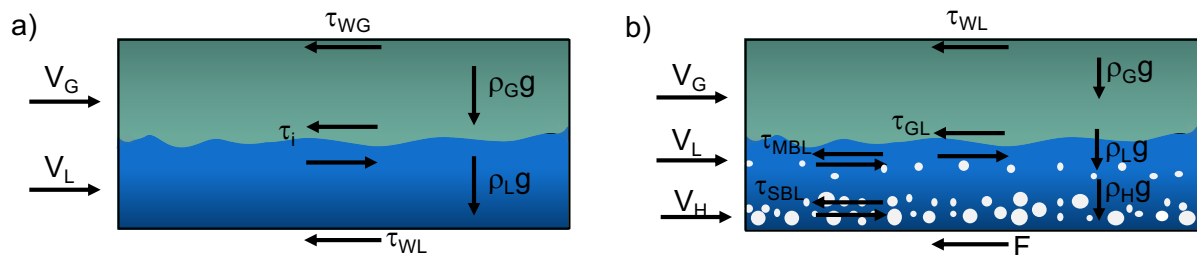
Source: own authorship.

The hydrate wall deposition is not only influenced by the wetted surfaces — because of the hydrophilic nature of the wall material — but also by the balance of the forces acting on the system — which impacts particle size, coalescence/disruption of agglomerates, deposit stability and, thus, the influence on the mechanisms of hydrate formation and accumulation (bedding, depositing, slurry for example). This is why the experiments presented herein were performed by varying the oscillation rates of the cell and liquid loading of the system. These parameters affect:

- The dispersion of the phases influencing the interfacial area and absorption of gas.
- The flow energy changing the wall shear and the impact of the flow at the extremities of the cell.
- The perimeter of the wetted surfaces.

Figure 2.3 shows the forces acting on the rock-flow cell. Before the onset of the hydrate formation, there is a two-phase system (water and gas) where the velocity of the gas and liquid phase, specific weight of each phase (gravity) and shear stress ( $\tau$ ) are the elements present in the system (Figure 2.3.a). The system becomes a three-phase system right after hydrate formation initiates, increasing the number of forces acting on the flow. At the beginning of hydrate formation (Figure 2.3.b), the same forces as described below for the two-phase system are present with the addition of the fluid friction force ( $F$ ) and the forces relative to the hydrate phase. The subscripts i, WL, WG, GL, MBL and SBL refer to shear stress, specific weight and velocity acting on the interface, wall-liquid, wall-gas, gas-liquid, moving bed layer and stationary bed layer, respectively.

Figure 2.3— Illustration of the forces presents in the rock-flow cell (a) before and (b) after the onset of the hydrate formation. Subscripts i, WL, WG, GL, MBL and SBL refer to shear stress ( $\tau$ ), specific weight ( $\rho g$ ) and velocity ( $V$ ) acting on the interface, wall-liquid, wall-gas, gas-liquid, moving bed layer and stationary bed layer, respectively.



Source: adapted from Hernandez (2006).

Upon hydrate formation, the hydrate phase can be split into a stationary bed layer and a moving bed layer depending on shear rate, hydrate agglomerates size, and fluid velocity. If the fluid flow energy is not enough to suspend the solids particles, hydrate agglomerates may settle; otherwise, they will be suspended in the liquid forming a moving bed layer, with a velocity smaller than that of the liquid velocity.

Later on, hydrate agglomerates in the bulk may deposit onto the pipe wall surface due to adhesive forces (wall deposition) as the system is a water-continuous one, once again changing the force balance in the rock-flow cell.



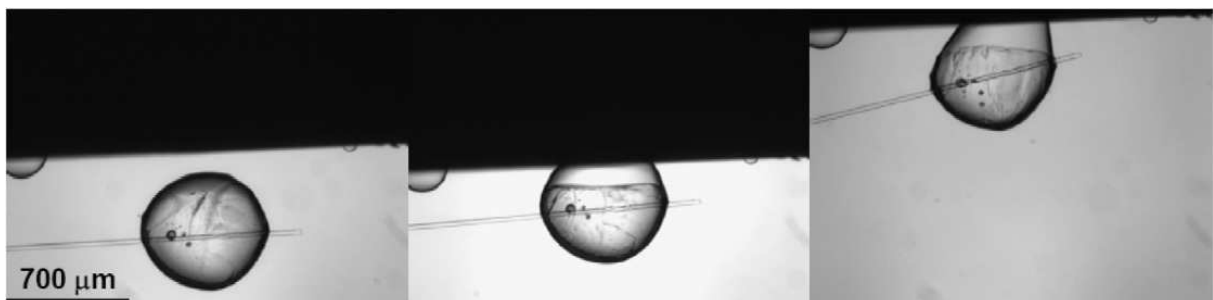
### 2.1.1 Cohesive and adhesive hydrates forces

The knowledge of the cohesion and adhesion between hydrate particles and between those particles and solid surfaces is pivotal to understanding hydrate deposition and sloughing — detachments of all the hydrates deposited on the wall or part of them — mechanisms. A few studies related to interfacial interaction are discussed below.

Nicholas et al. (2009a) measured the adhesive forces between cyclopentane (CyC5) hydrates and carbon steel (CS), assuming no free water in the system. It was found that entrained hydrate particles, 3-micron wide and larger, are not expected to deposit on the pipe wall under pipeline operational conditions in a methane system and 2 microns larger for condensate systems. Therefore, hydrate deposition is not likely to occur in cold (stabilised) flow conditions.

Moreover, although the adhesive forces between hydrate particles and carbon steel were weaker than the adhesive forces between CyC5 hydrate-CyC5 hydrate and ice-CS measurements, they may also be dominated by capillary forces, as evidenced in Figure 2.4 for ice and carbon steel experiments.

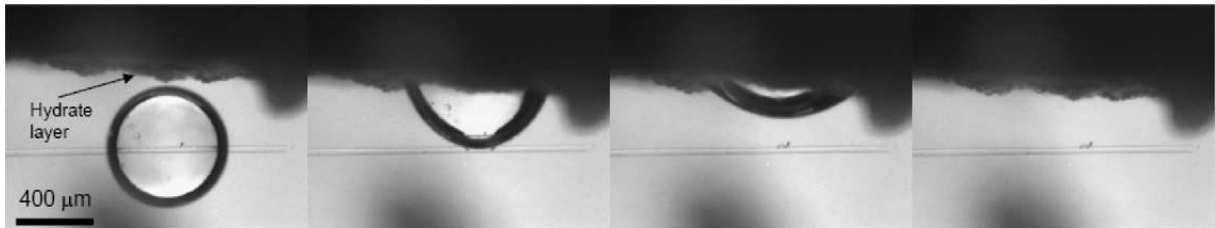
Figure 2.4 – Adhesive force measurement between ice and carbon steel near the melting point.



Source: Nicholas et al. (2009a).

They also noticed that if hydrates form directly on the steel surface, they will not be removed by the flow and, after being deposited, water might be absorbed by an existing hydrophilic hydrate layer, as shown in Figure 2.5.

Figure 2.5 – Tetrahydrofuran (THF)-water droplet being absorbed when brought into contact with hydrate-coated steel.



Source: Nicholas et al. (2009a).

Aman et al. (2011) measured CyC5 hydrate – CyC5 hydrate cohesion as a function of contact time, contact force and subcooling. Their results suggested that the cohesive force is dominated by capillarity during about the 30 s and, right after by sintering (growth of a crystal phase). According to the authors, hydrate growth may occur when the existing water outside the quasi-liquid layer is in contact with a hydrate former, and a pre-existing crystal exists near the interface. Moreover, they measured the hydrate cohesive force in the gas phase ( $9.1 \pm 2.1$  mN/m), which is approximately twice the strength of the liquid phase force ( $4.3 \pm 0.4$  mN/m).

According to Aman et al. (2016), managing flow regimes and the interfacial area is more cost-effective than minimising subcooling to reduce the risk of hydrate formation. Consequently, applying protective coatings on the interior of the pipelines or flowlines to prevent hydrate deposition is a technique to manage the risk of hydrate formation. Brown et al. (2017) observed that hydrate adhesion decreased for liquid and gas-phase systems, and hydrate deposition could be prevented for low-water content systems (5 %vol.) over the course of 24-hour experiments when using coated surfaces.

## 2.2 Hydrate wall deposition

Hydrate deposition on the wall is regarded as one of the critical mechanisms required to understand the increase in pressure drop observed during hydrate events and, in the worst-case scenario, the blockage of the flow. However, according to Lachance et al. (2015), it is one of the least well-known phenomena, neglected by most hydrate models or predictive tools.

The process of hydrate wall deposition may be influenced by the degree of subcooling, absolute temperature, flow parameters, the composition of the fluids, phase amounts, water production history, solid surface wettability and the presence of emulsifiers and inhibitors in the system. Liquid hydrocarbons with little tendency to form stable emulsions have shown a more favourable trend to form hydrate plugs when compared to the ones tending to form stable emulsions (Lingelem et al., 1994). Moreover, after hydrate formation, the flow regime will influence the hydrate distribution amongst the phases and the deposition along the flowline (Sum et al. 2002).

Hydrate deposition can be a slow process for systems under continuous operation, and there are two deposition mechanisms to consider: one is hydrate deposition on the wet solid surface and film growth; the other is the deposition of hydrate particles on the existing hydrate deposit due to constant wetting of the surface depending on the flow conditions (Sum et al. 2012).

The hydrate deposition acts as an insulating layer, thus reducing the effective wall heat flux. Since hydrate growth is mass-transfer or heat-transfer limited when the surface temperature of the deposit reaches the hydrate equilibrium temperature, hydrates may stop depositing and start annealing (Rao et al., 2013; Grasso et al., 2014; Straume et al., 2017).

Grasso et al. (2014) described three mechanisms which might govern water migration to the deposition surface. The first mechanism in Figure 2.6 consists of wetting the solid surface constantly, and once hydrates have formed, unconverted water remains trapped in the deposit pores; the second, a thin hydrate layer forms, and water reaches the deposit by capillarity and, in the third mechanism, water condenses on the upper surface to further form hydrate deposits.

Figure 2.6 – Mechanisms of water migration to the deposition surface.



Source: Grasso et al. (2014).

The occurrence of sloughing events is a concern when studying hydrate deposition. Song et al. (2018) proposed a quantitative way to calculate the hydrate

deposit stability, through which it might be possible to consider sloughing events in hydrate deposition models. According to the authors, the mechanical stability of hydrate deposits on pipe walls was reduced by increasing the flow rate or deposit thickness and could be improved by sintering. Moreover, the deposition length has little effect on the hydrate mechanical stability.

The formation of gas hydrates in multiphase flow conditions has been studied through numerical and empirical studies. In addition, empirical analyses can focus on a particular phenomenon, isolating it from the others or considering all the phenomena involved. Replicating field conditions in the laboratory is a challenging task for a variety of reasons, such as the need for a high-pressure gas source, a lengthy system to allow proper heat transfer, equipment limitation to mimic the actual shear in the system, and handling and storing field gas and liquid as well.

Austvik et al. (1997) conducted hydrate plug field tests at the Tommeliten Gamma gas-condensate field in the North Sea, and Hatton et al. (1997) carried out the same kind of tests in a gas-condensate flowline at the Werner Bolley well site in Wyoming. However, only some field tests have been conducted since operators might not be willing to promote hydrate blockage assessment in their fields given the hazards and costs involved in removing hydrate plugs.

Therefore, laboratory efforts have been made to replicate the operational field conditions as faithfully as possible. The mechanism of hydrate formation and accumulation can be divided into feasible experiments to study each phenomena involved separately — for example, the adhesion forces, agglomeration, wall deposition, etc — or to analyse all the phenomena involved at once — for example, through flow loop studies. However, although separating the phenomena involved in the process allows a better understanding of their effect on both hydrate formation and the accumulation mechanism, their interaction might be lost, thus masking what actually happens in the flowlines (Sum et al., 2012).

The study of hydrate deposition is divided among those who studied wall deposition through a Jerguson cell (Rao et al., 2013), rocking cell (Grasso et al., 2014; Straume, 2017) and flow loop experiments (Dholabhai et al., 1993; Nicholas et al., 2009b; Estanga et al., 2014; Aman et al., 2016). This work focuses mainly on studying the hydrate deposition process in multiphase flows through isochoric rock-flow cell

experiments. The oscillation rate was chosen to create a specific flow regime similar to the stratified wavy flow.

The differences between isochoric rock-flow cell experiments and pipeline operational conditions shall be emphasised; the former has a constant volume and number of components, thus resulting in less hydrate formation and reduced hydrate driving force, such as subcooling and pressure upon hydrate formation, whereas the latter has constant pressure and supply of water and hydrocarbons, resulting in continued hydrate formation. These differences should be considered when extending the rock-flow cell analyses to pipeline conditions.

### **2.3 Hydrate formation and accumulation in gas-hydrate-water system**

Rao et al. (2013) studied the hydrate formation and deposition on the outer surface of a cold pipe in water-saturated gas systems for pressures up to 11 MPa (1595.4 psi), bath temperature of 22°C and cold surface temperatures between 1 to 4°C yielding a maximum subcooling (difference between the hydrate surface temperature and the hydrate equilibrium temperature) of 12°C. The apparatus was kept inside a water bath, and the water-saturated gas (methane or methane/ethane mixture) circulated continuously over the steel pipe surface, which is the coldest point in the whole system, thus forcing hydrate deposition.

The authors observed that the hydrate deposition mechanism consists of water condensation on the cold surface following hydrate nucleation and film growth along the entire external surface of the pipe. Subsequently, hydrates grow with high porosity, and when the surface temperature of the deposit reaches the hydrate equilibrium temperature, hydrates stop forming and start annealing. This phenomenon decreases the porosity of the deposit because of water condensation, which fills the porous spaces. These observations follow the same trend of frost deposition on a cylindrical tube.

Moreover, they claimed that hydrate deposition is independent of the hydrate structure but depends on the heat transfer in the system, meaning that the deposit thickness is smaller for lower pressures since the hydrate equilibrium temperature is lower, thus reducing the driving force (subcooling) in the system. If the bath

temperature increases, the deposit thickness will also decrease because of the driving force reduction.

This experimental configuration is more convenient for analysing and quantifying the phenomenon. However, in an actual situation, the flow would be inward, and consequently, the hydrate deposits would grow inside the surface of the flowline.

Grasso et al. (2014) investigated the hydrate deposition mechanism through a rocking cell built with stainless steel with two polycarbonate inspection windows (50.8 mm of nominal pipe diameter and 254 mm long). The experiments were carried out with 50 %vol. water liquid loading, with subcooling between 5.5 and 11.5°C at an oscillation rate of 29 cycles per minute and a gas mixture composed of 74.7 mol% methane and 25.3 mol% ethane pressurising the cell up to 3.86 MPa (560 psig).

Initially, they found that the hydrate deposit was formed of a highly porous layer with accumulated water inside. Later, the deposit started annealing meaning that the porosity of the hydrate deposit was reduced. The annealing provided higher heat transfer across the deposit and consequently allowed more water to be converted to hydrates. Additionally, the thickness of the hydrate deposits increases by increasing the degree of subcooling. This behaviour was also observed by Rao et al. (2013).

Aman et al. (2016) carried out single-pass flow loop experiments to study the effect of gas velocity on hydrate formation and deposition rate in a gas-dominant system under an annular flow regime. The flow loop (2.54 cm OD pipe with 40 m of length) was initially pressurised up to 10.34 MPa (1500 psi) with gas mixture composed mainly of methane (87.3%mol of CH<sub>4</sub>), which was used as a substitute for natural gas, for subcooling ranges from 4.5 to 7.5°C.

According to the authors, by decreasing the gas phase velocity from 8.7 m/s to 4.6 m/s, the entrainment of the liquid water droplets in the gas phase was reduced. At constant subcooling, it reduced the total hydrate formation rate by a factor of six and increased the time to reach the maximum pressure drop allowed in the system. Consequently, the gas velocity reduction may delay the hydrate blockage in the system.

## 2.4 Hydrate formation and accumulation in oil-gas-hydrate-water system

Hydrate formation and deposition in condensate pipelines saturated with natural gas components were studied by Dholabhai et al. (1993) through a recirculation flow loop at temperatures from 3.5 to 5°C, water content from 0.5 to 5 %vol. and velocities of 0.9, 1.8 and 2.5 m/s emulating a slug of liquid. They observed hydrate deposits at one or more locations of the flow loop during the experiments with 3 and 5 %vol. water content but no hydrate deposition at 0.5 %vol. Moreover, as the sample fluid was not completely dewaxed, they suggested that there might be an interaction between wax precipitation and hydrate formation. However, recirculating flow loop tests are not suitable for understanding hydrate deposition because the depletion of the hydrate formers owing to their consumption during hydrate formation may reduce the hydrate deposition rates.

Nicholas et al. (2009b) studied hydrate deposition in a single-pass flow loop with an 85.3-m test section with a 9.3-mm ID pipe. The experiments were conducted with an industrial condensate mixed with propane and methane at temperatures between -21 and 3°C and flow rates of 0.3 m/s and 0.6 m/s, approximately. They noticed a gradual increase in the pressure drop above the liquid water saturation curve and a temperature increase caused by the solid deposit acting as insulation, which led to deposit propagation downstream. Furthermore, a localised hydrate/ice restriction and a fast pressure drop increase were observed below the liquid water saturation curve, resulting in free water coalescence (dissolved water in condensate).

Estanga et al. (2014) analysed hydrate deposition and evaluated a commercial LDHI- anti-agglomerate in a flow loop (7.4 cm ID and 49.4 m long) filled with gas-saturated kerosene and 30 or 60 %vol. of water content at 10.34 MPa (1500 psia). The loop was equipped with radioactive tracer detectors to locate hydrates deposits. They measured the average maximum tracer velocity before and after hydrate formation and compared it to the pressure drop and the fluid sampling criterion of deposition. The authors reported that experimental techniques relying on pressure drop might fail to identify hydrate deposition in liquid-full flowlines as the pressure drop cannot be split into its components associated to diameter reduction (caused by hydrate deposition) and increase in viscosity (due to hydrate particle growth in the bulk phase). They

pointed out that this issue could be circumvented through radioactive tracer techniques.

Srivastava et al. (2017) investigated hydrate formation and transportability through flow loop (9.65-cm ID, 89.92-m long) experiments under transient conditions. The flow loop was filled with crude oil and brine (60 %vol. liquid loading and water fractions between 30 to 90 %vol.) and pressurised up to 68.95 MPa (1000 psig) with methane at a chamber temperature of 3.3°C and mixture velocities between 0.73 - 2.86 m/s. Their results suggested that transient conditions could lead to higher pressure drops compared to steady-state conditions. During the transient experiments, they observed that hydrate formation might have destabilised the water droplets dispersion in the oil phase, raising the free water availability, which may promote hydrate agglomeration and faster bedding due to capillary and sintering forces (Aman et al., 2011).

Srivastava et al. (2017) found that a transportable hydrate slurry formed at high mixture velocities, suggesting that higher shear forces might have broken the hydrate agglomerates down, providing the required hydrodynamic drag force to carry the hydrate particles rather than allowing them to settle. Additionally, a transportable slurry flow was observed during the tests with 2 %vol. of AA for both transient and continuous experiments.

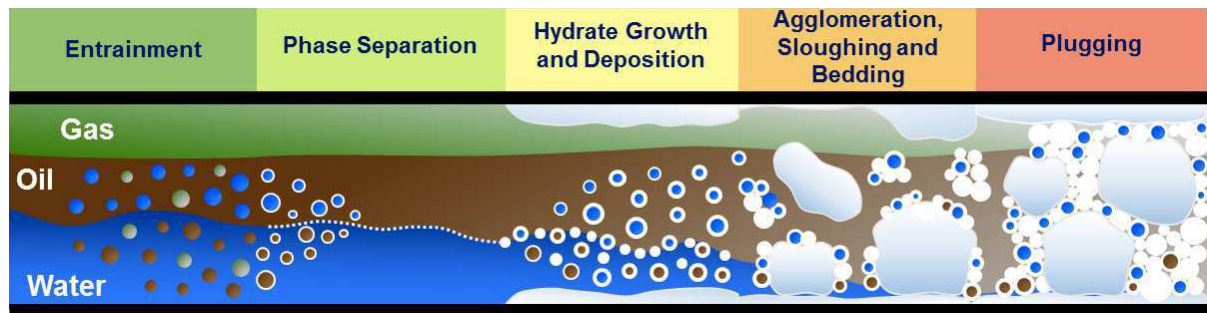
Straume (2017) conducted an experimental study in a rocking cell to investigate the hydrate deposition and sloughing in a multiphase flow – namely slug flow – for different systems, inhibited or not, composed mainly of water, methane, ethane and a liquid hydrocarbon phase made of mineral oil or gas condensate. The rocking cell was submerged in a temperature-controlled water bath, and hydrate deposition on the upper wall was induced by using a separate chiller to cool the upper surface of the rocking cell, causing a temperature gradient inside the cell. The cell was cooled down from an initial temperature of 20°C and a pressure of 3.9 MPa (565.65 psi) to conditions between 1 to 9°C at 35 oscillations per minute with an amplitude of  $\pm 10^\circ$  with an upper wall cooling temperature of 1°C. All experiments were performed with 70% liquid loading and 60% of water content.

Based on the experimental measurements and observations, the author calculated the porosity and amount of water converted to hydrates and proposed a



new conceptual model for hydrate formation and accumulation in a non-emulsifying system (Figure 2.7). The model included changes in the dispersion of the oil and water phases shortly after the hydrate formation onset and considered a combination of hydrate deposition and agglomeration instead of considering deposition as the fundamental mechanism for condensate systems and agglomeration for oil systems (Sum et al., 2012).

Figure 2.7 – Conceptual hydrate formation and accumulation model in a shear-stabilised dispersion.



Source: Straume (2017).

The author also noticed that high-temperature gradients and low subcooling gave rise to an intense occurrence of sloughing compared to high subcooling and no internal temperature gradient. A potential sloughing-free window was also found, which could be valuable for hydrate management strategies if validated.

Zhao et al. (2017) correlated the hydrate deposition morphologies to the hydrate porosity from an oil-dominated system with 70 %vol. liquid loading (oil + water) with a gas mixture composed of 74.7 mol% methane and 25.3 mol% ethane through isochoric experiments in a high-pressure rocking cell. The mineral oil has no surface-active components; therefore, water was present as droplets in the oil phase. These experimental conditions are similar to Straume (2017) work. Still, they investigated the hydrate formation under the pressures of 2.07, 2.76, and 3.45 MPa (300, 400, and 500 psig) with three different water volume fractions (10, 20, and 30%) at a chiller temperature set to 1°C.

They identified five different hydrate morphologies: stationary bedding layer, moving bedding layer, stationary hydrate sphere with stationary bedding layer, moving spherical hydrate sphere, and moving spherical hydrate sphere with a stationary bedding layer. They found out that the three first morphologies presented a higher

porosity because the hydrate chunks restricted the relative motion, and only part of their surface was affected by the shear and compression forces. Additionally, the water conversion and, consequently, the hydrate formation depend on the final hydrate accumulation morphology and its relative motion in the cell since the water conversion increased considerably in the experiments where a moving hydrate ball had formed.

Furthermore, they reported that the shear-stabilised emulsion was broken after hydrate formation onset; this phenomenon had previously been mentioned by Straume et al. (2015).

## **2.5 Final considerations of this chapter**

Hydrate wall deposition is considered a key mechanism to understanding the process of production impairment and pipeline blockage due to hydrate plugs formation. Temperature, fluid properties, flow pattern, cohesive and adhesive force, and shear force are among the parameters influencing hydrate wall deposition.

The literature review indicated that more work should be done to increase the comprehension of hydrate deposition and sloughing mechanisms mimicking an actual flowline condition as a unique and defined phenomenological model describing the process of hydrate formation and wall deposition under different flow, fluids and system conditions does not yet exist.

This work made relevant contributions to the knowledge of the main mechanisms — wave effect or agglomeration — leading to hydrate accumulation for water/gas mixtures and liquid hydrocarbon/ water/ gas mixtures. In addition, it brought a new conceptual model for hydrate formation and accumulation under multiphase flow conditions. The present work also highlighted the importance of the hydrodynamics on the process of hydrate wall deposition. The flow conditions before the beginning of the hydrate formation have a significant role on the location of the deposit as it indicates the water-wetted areas in the flowline. The lower wall temperature, when compared to the bulk temperature, has a minor influence on the formation of hydrate wall deposits. Table 2.1 synthesises some works on hydrate formation and accumulation presented in this chapter.

Table 2.1— Syntheses of some studies on hydrate formation and accumulation.

<b>Authors</b>	<b>Fluids/ Material</b>	<b>Experimental apparatus</b>	<b>Study objectives</b>	<b>Findings</b>
Nicholas et al., 2009a	Cyclopentane (CyC5) hydrates and carbon steel (CS)	Adhesive forces balance	The adhesion force of hydrate particles on a carbon steel surface	The adhesive forces between cyclopentane (CyC5) hydrates and carbon steel (CS) is lower when compared to CyC5 hydrate–CyC5 hydrate.
Aman et al., 2011	CyC5 and steel	Micromechanical force apparatus	The adhesion and cohesive forces amongst hydrate particles	Hydrate cohesive force in the gas phase is approximately twice the strength of the magnitude of the liquid phase force
Aspenes et al., 2008	Crude oil and solid surface (stainless steel, aluminum, Brass, glass, quartz and two epoxy surfaces)	Contact angles determined from image analysis	The influence of the wettability of solid surfaces on the hydrate deposition mechanism	Petroleum acids are found to render all the surfaces more oil wet. It indicated that hydrates adhesion to the wall will be less when acids are present in the oil.
Brown et al., 2017	Omniphobic composite polymer, methane-ethane gas mixture and mineral oil	Micromechanical force apparatus and Rock-flow cell	The effect of coating surfaces on hydrate adhesion	Hydrate deposition can be prevented over the course of 24 hours experiment using coated surfaces.
Grasso et al., 2014	Water and methane-ethane gas mixture	Rock-flow cell	The hydrate deposition mechanisms	The water reaches the deposition surface through direct liquid contact, liquid capillarity and water evaporation/condensation
Austvik et al., 1997	Gas-condensate	Field tests	Hydrate plug formation and removal	Hydrate plugs were formed in most of the experiments, but transported hydrates were also observed.
Hatton et al., 1997	Gas-condensate	Field tests	Hydrate plug dissociation	All the plugs were found to be porous. The data will be analysed to determine the parameters relating to hydrate

Table 2.1— Syntheses of some studies on hydrate formation and accumulation.

<b>Authors</b>	<b>Fluids/ Material</b>	<b>Experimental apparatus</b>	<b>Study objectives</b>	<b>Findings</b>
				blockages and dissociation processes.
Rao et al., 2013	Water-saturated gas systems	Jerguson cell	Hydrate formation and deposition on a cold surface	Hydrate deposition is independent of the hydrate structure, but depends on the heat transfer in the system.
Straume, 2017	Mineral oil or gas condensate and methane, ethane gas mixture	Rock-flow cell	Hydrate deposition and sloughing in a multiphase flow	The experiments demonstrated combination of various mechanisms with agglomeration as the most dominant in certain systems and deposition in others.
Nicholas et al., 2009b	Liquid condensate mixed with propane and methane	Single-pass flow loop	Hydrate/ice plugging and deposition mechanisms	Two different hydrate/ice plugging mechanisms were observed: rapid plug formation when cooling below the liquid-water saturation curve, and uniform deposition, acting as insulation on the wall, from a dissolved-water phase
Estanga et al., 2014	Methane-Ethane-Propane gas mixture, Kerosene, and LDHI-anti-agglomerant	Flow loop	Hydrate deposition in liquid system	Radioactive tracer can identify hydrate deposition in liquid pipelines.
Aman et al., 2016	Gas-dominant system	Single-pass flow loop	The rate of hydrate growth and particle deposition	The entrainment of liquid water droplets in the gas phase is important to assess the hydrate growth rate and blockage risk.
Srivastava et al., 2017	Crude oil, brine, methane and anti-agglomerant	Flow loop	Hydrate formation and transportability in transient operation	The rapid hydrate formation and agglomeration and water-in-oil emulsion destabilization may indicate a higher

Table 2.1— Syntheses of some studies on hydrate formation and accumulation.

<b>Authors</b>	<b>Fluids/ Material</b>	<b>Experimental apparatus</b>	<b>Study objectives</b>	<b>Findings</b>
				operational risk for transient conditions compared to continuous operation.

Source: own authorship.

### 3. METHODOLOGY

This study focuses on the experimental characterisation of hydrate wall deposition in multiphase flow. The experiments were carried out in a high-pressure rock-flow cell, and the effect of temperature (subcooling), liquid loading, water content and gas (pure methane or a mixture of methane/ ethane) on the hydrate formation and accumulation were investigated. A total of seventy-one experiments were performed under dynamic conditions, twelve for water and pure methane systems, twenty-seven for water and gas mixture systems and thirty-two for water, oil and gas mixture systems. These classifications is related to the system conditions before the hydrate formation begins because, after the formation, the presence of hydrates in the system must be taken into account. This chapter presents a description of the experimental apparatus followed by the properties of the materials, the procedure and experimental conditions used in the experiments reported herein. The uncertainties of the measured data are presented at the end of this section.

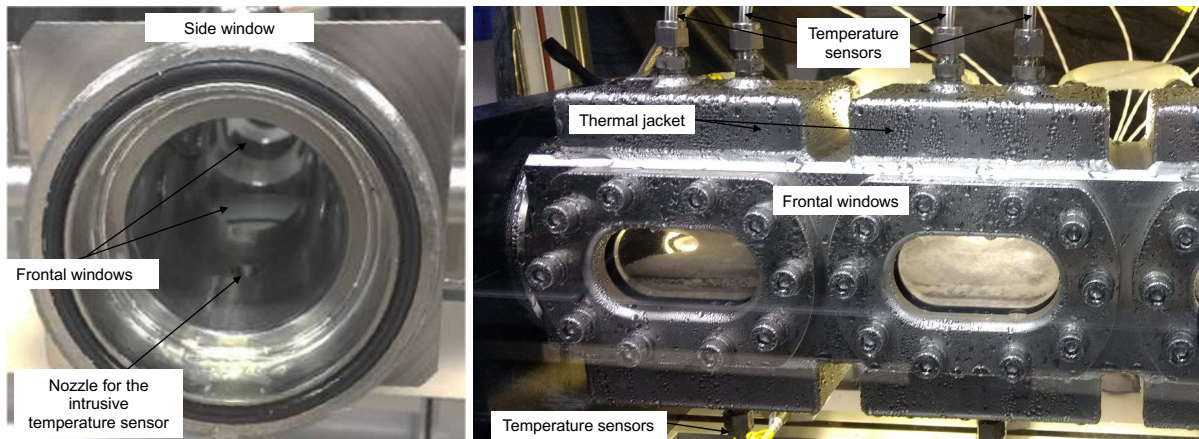
#### 3.1 Apparatus description

The experimental investigation was carried out in two different high-pressure rock-flow cells with cylindrical shape located in the Multiphase Flow Research Center (in portuguese Núcleo de Escoamento Multifásico - NUEM) of the Federal University of Technology – Paraná (UTFPR). The cells have an internal diameter of 51 mm and an internal length of 500 mm, yielding a total volume of approximately 1020 ml. The main difference between the rock-flow cells is the size and number of viewing windows.

##### 3.1.1 Rock-flow cell with six front viewing windows

The rock-flow cell has a cylindrical shape, see Figure 3.1, and comprises eight viewing windows, three at each side (0.08 x 0.041 m) and two at each end (0.042 m in diameter), for lighting and visual observation of the mechanisms involved in the process of hydrate formation and accumulation under different flow conditions. The windows are made of polycarbonate, and cameras are installed in front of these windows to allow footage of the experiments.

Figure 3.1— Rock-flow cell with visualisation capabilities and cylindrical shape.



The rock-flow cell system allows the refrigeration of the upper and bottom walls at different temperatures to simulate the heat transfer through the pipeline wall under seabed conditions owing to the forced gradient of temperature created inside the cell. The rock-flow cell system, as shown in Figure 3.2, is composed of:

- A visual high-pressure rock-flow cell which can be pressurised up to 100 bar.
- An electric motor connected to the cell structure through a metal shaft.
- Thermal jackets located on the upper and bottom wall of the cell connected to two circulation baths (thermostat) responsible for the internal temperature control of the cell.
- An air conditioning unit to control the external temperature of the cell (that is, to refrigerate the chamber where the cell is located) and to avoid liquid condensation on the surface of the cell.
- Nine Resistance Temperature Detector (RTD PT100) — three to measure the upper wall surface, three intrusive ones to measure the gas phase and three to measure the bottom wall surface— disposed along the length of the cell. The temperature sensors are logged into the data acquisition system.
- A controller unit responsible for the data acquisition and motor rotation control.

- An image capturing system composed of four video cameras to monitor and record the experiments. The cameras oscillate together with the rock-flow cell structure. As they were installed in front of the windows, the images presented herein show only the region to which the camera was assigned.
- One pressure transmitter. The pressure sensor is logged into the data acquisition system.
- A pressure safety (release) valve.

Figure 3.2— Rock-flow cell system with six front viewing windows.



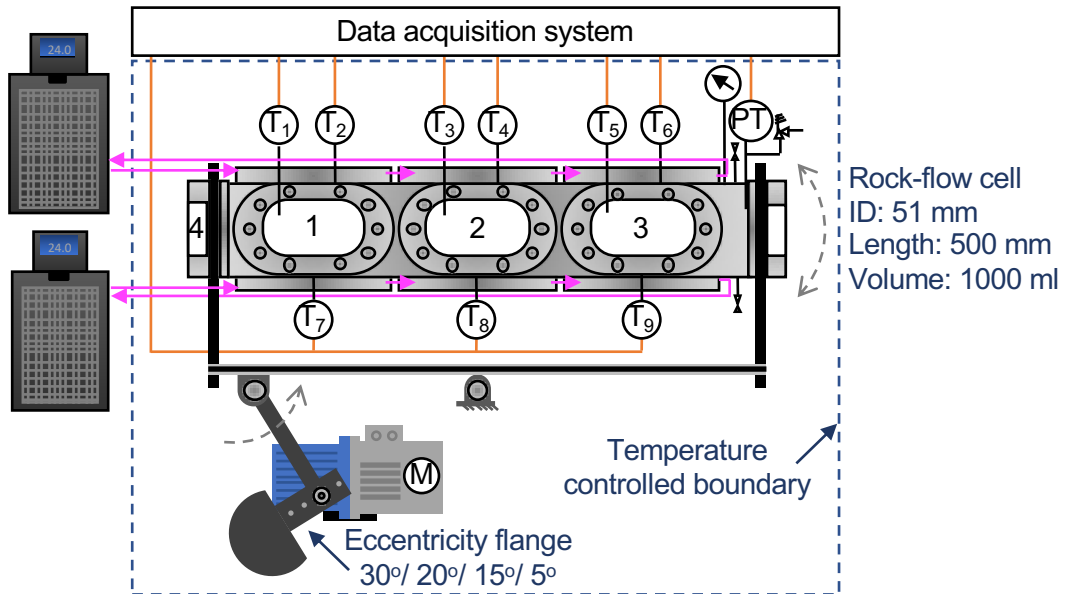
Source: own authorship.

The angle of the cell can be adjusted at 5°, 15°, 20° and 30°, allowing different flow conditions and shear rates. The electric motor coupled to the cell oscillates between positive and negative cell inclinations at an oscillation rate between 2 to 22.5 rpm. The oscillation enhances the mixing inside the cell and creates a gravity-driven flow which creates different flow and shear conditions that could promote hydrate formation, accelerates the thermodynamic equilibrium process, and increases the surface contact among the phases. A flexible line connects the rock-flow cell to a gas



booster system connected to the gas cylinder containing the gas mixture used in the experiments. The gas booster system increases the supply gas pressure and has the same operating principle as hydropneumatics pumps. Figure 3.3 shows the experimental setup, and the numbers on the viewing windows, 1 to 4, indicate the location of the cameras.

Figure 3.3— Schematic of the setup of the rock-flow cell apparatus with six front viewing windows.



Source: own authorship.

An air conditioning chamber surrounds the rock-flow cell. The thermostatic bath allows the thermoregulation of the cell by circulating a thermal fluid which transfers the temperature set for the rock-flow cell wall through the thermal jackets located at the top and bottom of the cell. Because of the low experimental temperatures required, the thermal fluid used is a mixture of water and monoethylene glycol (MEG).

The thermal jackets in the upper and bottom regions of the cell are connected to separate chillers — two thermostat circulation baths — that can be set to different temperature conditions to force a gradient temperature inside the cell. On doing it, it is expected to locally induce hydrate deposits due to the lower temperature wall. Table 3.1 presents some technical specifications of the equipment of the experimental configuration.

Table 3.1— Specifications of the experimental equipment.

Item	Provider	Note
Rock-flow cell	Sejin Young Tech	Stainless steel 316 ID 51mm x 500mm Max. Pressure 100 bar
Pressure Transmitter	Wika Model A-10	Measuring range from 0 to 160 bar Non-linearity 0.5% span
Temperature Sensor	Intelligent Sensor Line	PT100Ω Class A Material SUS304
Nutating Mixer Motor	Motovario	AC Motor 400W Actual rpm: 2 – 22.5 rpm
Paperless recorder FX1000	Yokogawa	Measurement Accuracy : 0.05% of Reading(DCV) and 0.15% of Reading(TC, RTD) Scan Interval: 1s, 2s, 5s
Circulating Baths	Polyscience AP 15R-40	Reservoir capacity: 15 l Temperature range: -40°C to 200°C Temperature Stability ±0.005°C
Camera	Logitech HD Pro C920	Max resolution: 1080p/ 30 fps - 720p/ 30 fps Diagonal field of view: 78°

Source: own authorship.

Most of the experiments discussed herein were performed with this experimental apparatus.

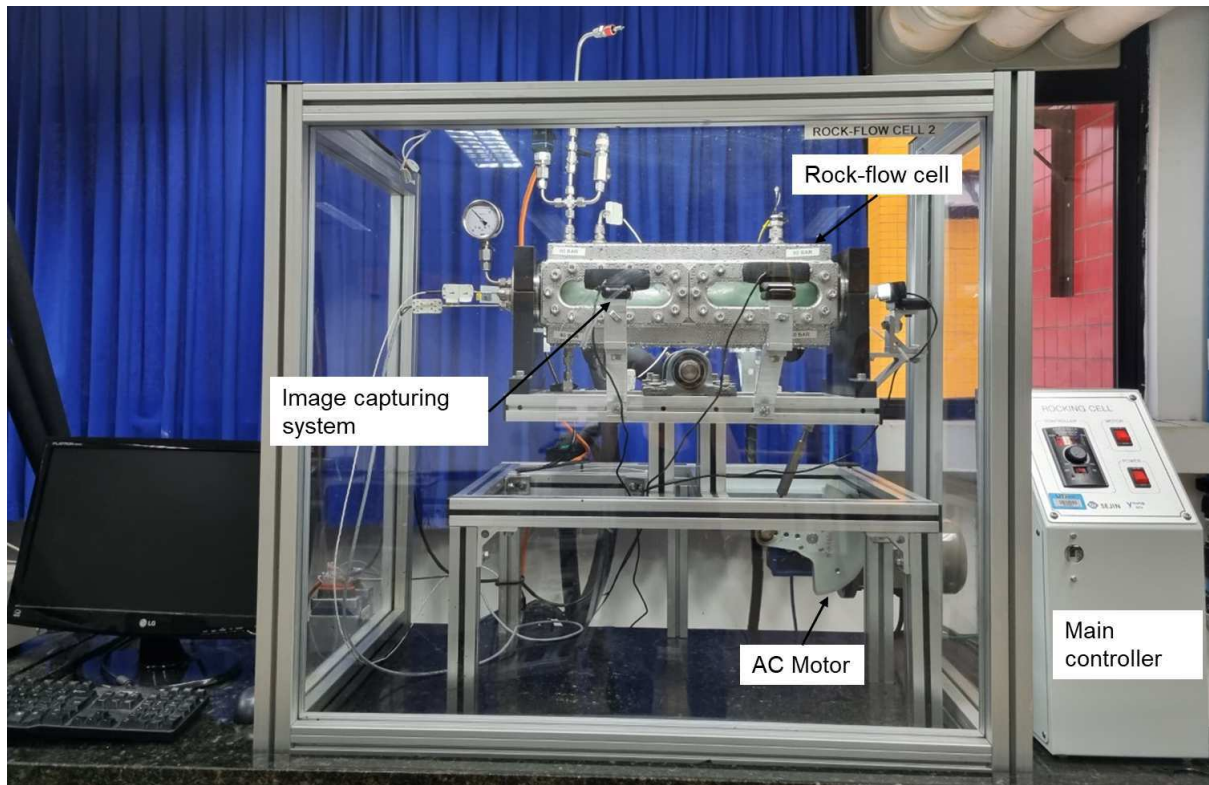
### 3.1.2 Rock-flow cell with four front viewing windows

This rock-flow cell was designed with a larger front window to allow a larger experimental viewing area. The cell has a cylindrical shape and comprises six viewing windows, four at each side (0.175 x 0.040 m) and two at each end (0.042 m in diameter), for lighting and visual observation of the mechanisms involved in the process of hydrate formation and accumulation under different flow conditions. The windows are made of polycarbonate, and cameras are installed in front of these windows to allow footage of the experiments.

Figure 3.4 shows a photo of the experimental bench. The experimental system consists of a pressure transmitter, six temperature sensors (two to measure the upper

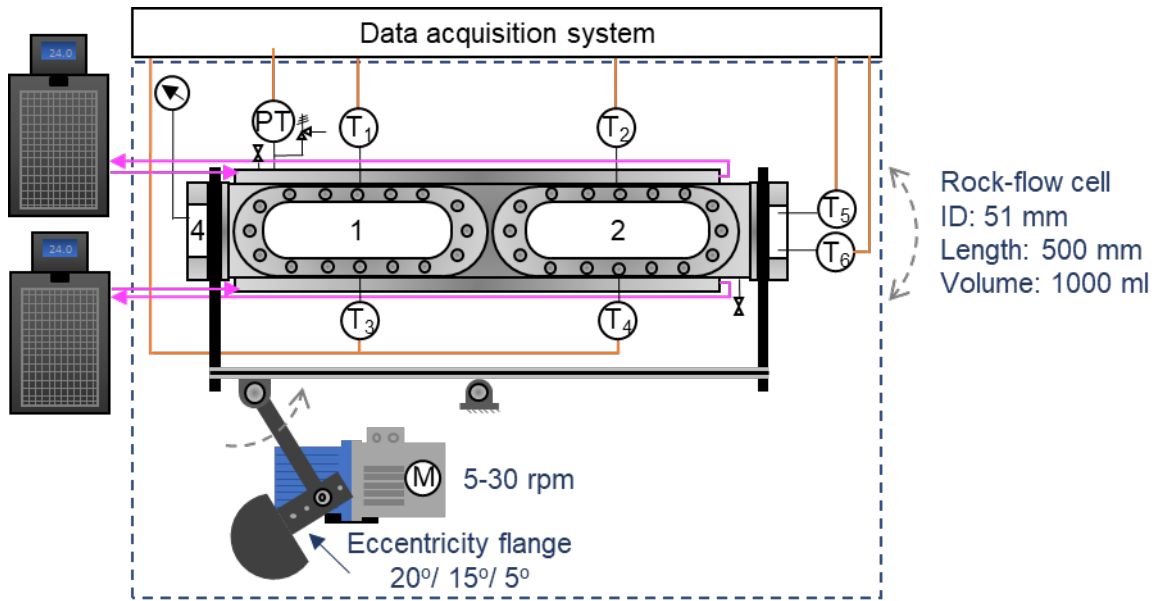
wall surface, two to measure the bottom wall surface and two intrusive ones to measure the gas and liquid phase, respectively), a nutating mixer motor, two circulating baths and three cameras. The specification of these equipments were mentioned above, section 3.1.1. Figure 3.5 presents the experimental setup.

Figure 3.4— Rock-flow cell system with two viewing windows.



Source: own authorship.

Figure 3.5— Schematic of the setup of the rock-flow cell apparatus with four front viewing windows.



Source: own authorship.

The rock-flow cell with four front viewing windows was used to perform the experiments for the oil-gas-water system, condition before the onset of hydrate formation, with the liquid loading ranging from 40 to 60 %vol.

### 3.1.3 Rock-flow cell setups

The experimental apparatus can be configured to allow:

- Studying the influence of the temperature gradient on hydrate formation and wall deposition by setting different temperatures for the upper and lower region of the cell.
- Analysing the effect of subcooling on hydrate formation and accumulation by varying the temperature throughout the experiment or along the whole length of the apparatus by isolating the thermal jackets in each section of the cell.
- Investigating the influence of flow conditions on hydrate formation and accumulation by varying the liquid loading, pipe inclination or oscillation frequency.

- Examining the effect of fluid properties, chemical additives, emulsions or non-stable emulsions on the mechanism of hydrate formation and accumulation.
- Evaluating hydrate formation and accumulation during transient operations such as shut-in/restart of flowlines (Kakitani et al., 2021; Pickarts et al. 2022).
- Studying the mechanism of hydrate formation and accumulation in different systems: oil continuous, gas continuous or water continuous.
- Switch between experimental methodologies, either isobaric or isochoric, with minor changes in the system setup.

The output data of the experimental system described above are pressure and temperature data recorded for each selected time step and the footage obtained through the cameras located along the length of the cell.

### **3.2 Experimental procedure**

After cleansing the rock-flow cell with water and liquid dishwasher (whenever necessary) followed by a rinse with distilled water, the sample fluid was admitted at room temperature with the help of a glass syringe. The amount of liquid admitted is known by previously weighing the fluid on an electronic analytical balance (JKI model JK-EAB-2204N). Because the sample fluids (water and mineral oil) are colourless, the aqueous phase was dyed with a blue hydrophilic dye and the hydrocarbon liquid phase with a yellow lipophilic dye for better contrast of the liquid phases. This will help to identify the fluids trapped inside the porous hydrate structure at a later time.

Subsequently, the cell was evacuated for approximately 30 minutes, whilst the air conditioning was turned on, and the chillers were set to the starting experimental temperature. To guarantee that the sample was above the hydrate formation region, all the experiments with gas methane started at 20°C, whereas the gas mixture experiments started at 24°C. These differences in the initial temperature conditions are related to the differences in the hydrate formation temperature between the gas

samples used. The gas booster line was connected, and the cell was pressurised up to 70 bar. The equation of state for a real gas was used to estimate the mass of gas admitted into the cell. The gas compressibility factor ( $Z$ ) was given by Multiflash<sup>TM</sup>. The experiments were carried out under isochoric conditions; therefore, the system's composition was constant throughout the experiments. Consequently, any variation in physical properties is a function of the temperature and pressure applied.

The experiments were performed at a constant oscillation rate between 06 to 18.75 rpm with an inclination angle of  $\pm 20^\circ$ . These conditions create a gravity-driven flow comparable to a stratified wavy flow pattern in a pipeline. The rock-flow cell was left oscillating for about one hour at a constant temperature to guarantee the liquid phase saturation with the gas mixture. When the pressure stops decreasing as liquid/gas solubility reaches its equilibrium, the data acquisition begins and the experiment starts. The data-acquisition system was set to scan intervals of 2s (time step). The video cameras were turned on, and the chillers' temperature changed from the initial temperature to the desired experimental temperature, which was kept constant throughout the experiment.

In the experiments, the bottom wall temperature ranged from 4°C to 10°C to induce hydrate deposition on the upper wall. However, the upper temperature was kept constant at 4°C. The upper wall temperature was chosen to simulate the seabed conditions as the average temperature of the sea water decreases as the water depth increases. Although hydrate could form at higher temperatures depending on the local pressure, in Brazil, the seabed stabilises at around 4°C for water depths of 800 m (Oliveira 2018). Exceptions occurred for the gas methane experiments, where the upper and bottom thermal jackets were set to the same cooling conditions, ranging from 1.7°C to 5.7°C, because of the lower subcooling (a maximum subcooling of approximately 9.7°C at 70 bar according to Multiflash®) when compared to the gas mixture (approximately 17.2°C at 70 bar according to Multiflash®).

When hydrates start forming in an isochoric and isothermal system, the pressure decreases because of the gas consumed to form the gas hydrate. After about 48 hours from the beginning of the hydrate formation or when the pressure decrement is low indicating that a steady-state condition is reached, the hydrate dissociation starts. The system is reheated to the initial temperature to dissociate the gas hydrate

and to assure that no leakage has occurred, which is confirmed by measuring the same initial pressure and temperature condition. This signals the end of the experiment. Supposing a new experiment with the same fluids was planned, then the new experiment starts after at least 12 hours from the time at which all the hydrates had dissociated and the initial temperature and pressure from the former experiment had been stabilised. Otherwise, the system is depressurised and the liquid fluid drained and properly discarded.

The hydrate formation was hard to initiate during some experiments, especially for pure water and methane gas systems. For this kind of system (pure water and methane gas), before the investigation started, the temperature was reduced to above zero Celsius degrees to increase the subcooling (driving force) that would ease the hydrate formation. After the hydrate formation onset, the hydrates dissociated at a temperature slightly above the hydrate equilibrium temperature to retain some “memory effect”. Hydrates preserve a “memory” of their structure when melted at moderate temperatures – as long as the melting time is not too long. Therefore, the experiments obtained from melting hydrates tend to form hydrates more quickly than those with fresh water or, in other words, with no previous hydrate history (Sloan and Koh 2008).

With the data acquired, it is possible to estimate the amount of hydrate formed through the pressure drops and temperature data with the aid of a software or knowing the hydration number. Through the footage, it is possible to observe the phenomenological behaviour involved in the process of hydrate accumulation under different conditions.

### **3.3 Materials**

The experiments were performed under dynamic conditions. The three systems studied are composed of (i) distilled water and gas methane (99.995% purity); (ii) distilled water and a gas mixture consisting of  $74.7 \pm 0.2$  mol% methane/  $25.3 \pm 0.2$  mol% ethane; and (iii) a combination of distilled water and mineral oil as the liquid phase and the gas mixture as the gas phase. The mineral oil, which was supplied by Sigma-Aldrich, is composed mainly of saturated and aromatic hydrocarbons. Table 3.2

presents its properties. In the experiments, the mineral oil forms a shear stabilised dispersion with the distilled water. White Martins provided the gases used in the experiments, and the water was distilled in our laboratory.

Table 3.2— Specification of the mineral oil.

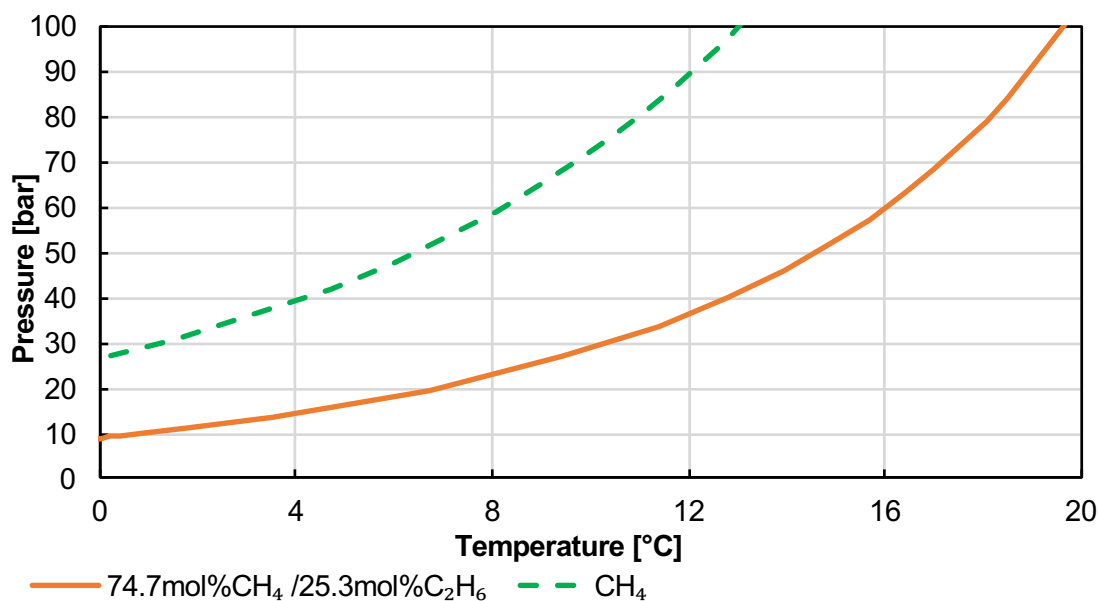
<b>Property</b>	<b>CAS Number</b>	<b>Appearance</b>	<b>Specific Gravity [g/ml] at 25°C</b>	<b>Viscosity [cst] at 40°C</b>
Mineral Oil	8042-41-5	Colourless	0.838	14.20-17.00

Source: Sigma-Aldrich.

The gas mixture was chosen because its components are found in natural gas and form hydrate structure II whilst pure methane is a primary component of natural gas and forms structure I (Holder and Hand 1982, Sum et al. 1997). In addition, the pressure and temperature are important parameters related to the driving force for hydrate formation: generally speaking the higher the pressure and the lower the temperature conditions, the greater the driving force to begin the hydrate formation. The hydrate equilibrium temperature of the gas mixture used in the experiments is higher than that of pure methane at the same pressure. According to Figure 3.6, the hydrate equilibrium temperature at 70 bar is 9.7°C for pure methane and 17.2°C for the gas mixture. Consequently, the gas mixture's driving force (subcooling) is higher, forming hydrates more quickly in systems under the same pressure and temperature conditions, when inside the envelope of hydrate formation. Note that subcooling is defined as the difference between the hydrate equilibrium temperature and the experimental temperature (Sloan et al. 2011). Generally, it is necessary to cool the system some degrees below the hydrate equilibrium temperature — at constant pressure — to induce hydrate formation due to hydrate metastability, which prevents its formation under hydrate equilibrium conditions.



Figure 3.6— Hydrate equilibrium condition for water and pure methane and for water and a gas mixture composed of 74.7mol% methane and 25.3mol% ethane.



Source: Multiflash version 6.1.35.

### 3.4 Experimental conditions

The experiments were performed at different subcooling, liquid loading — ratio of the total volume of liquid admitted into the cell divided by the total volume of the cell — and oscillation rate conditions to investigate their influence on the mechanism of hydrate formation and accumulation. Hydrate formation occurs under conditions above the hydrate equilibrium curve because of the hydrate metastability. Hence, all the experiments were carried out at temperatures below the hydrate equilibrium condition. Table 3.3 summarises the seventy-one experiments discussed herein and the two performed under static conditions (with a still the rock-flow cell).

Table 3.3— Experimental grid of the rock-flow cell.

Gas phase	Liquid phase	Water content [%]	Liquid Loading [%vol]	Oscillation [rpm]	Cooling Bath/wall	
					Upper [°C]	Bottom [°C]
CH <sub>4</sub>	Water	100	30	11.25	1.7	1.7
CH <sub>4</sub>	Water	100	30/ 40/ 50	18.75	1.7/ 3.7/ 5.7	1.7/ 3.7/ 5.7
CH <sub>4</sub> +C <sub>2</sub> H <sub>6</sub>	Water	100	20/ 40/ 60	06/ 11.25/ 18.75	4	4/ 7/ 10

Gas phase	Liquid phase	Water content [%]	Liquid Loading [%vol]	Oscillation [rpm]	Cooling Bath/wall	
					Upper [°C]	Bottom [°C]
CH <sub>4</sub> +C <sub>2</sub> H <sub>6</sub>	Water	100	60	-	4	10
CH <sub>4</sub> +C <sub>2</sub> H <sub>6</sub>	Water and mineral oil	20/ 45/ 70	40/ 60/ 80	06/ 11.25/ 18.75	4	4/ 10

Source: own authorship.

The experiments were limited to temperatures above the ice-formation temperature to ensure only hydrate crystal formation and exclude any ice crystal formation. For the gas mixture, some experiments were designed to force a gradient of temperature inside the rock-flow cell by keeping the upper wall at a temperature lower than that of the bottom wall. A higher bottom wall temperature means less driving force (subcooling) for hydrate formation. In addition, the system pressure after the beginning of the hydrate formation decreases because of the gas consumed to form hydrates (a result of the isochoric methodology employed); as a consequence, the driving force of the system is reduced throughout the experiment, what influences the amount of hydrate formed.

Additionally, two experiments were performed with the rock-flow cell fixed in a position (static experiments) to investigate the influence of water evaporation/ wall condensation, capillary force, and flow condition on the formation of hydrate deposits. In one experiment, the rock-flow cell was stopped horizontally; in the other, the cell stood inclined at 11°. The experimental condition was 60%vol of liquid loading, 100% of water content, the gas mixture (74.7%mol methane and 24.5%mol ethane) as the gas phase with the bottom wall at about 10°C and the upper wall temperature at about 4°C.

### 3.5 Accuracy in the measured data

Every experimental measurement is associated with experimental uncertainty, which comes from random errors (for example, from the user or the environment) and systematic errors (for example, from the inherent variations in the performance of the instruments). Systematic errors must be corrected and minimised whenever possible.

The system's pressure and temperature are measured from a pressure transmitter and a resistance temperature detector (RTD PT100), respectively. By the standard error of the instrumentation, it is possible to scale the magnitude of the data inaccuracy through the error propagation technique. The sample fluids were weighted before being admitted to the rock-flow cell. The densities of the fluids at the inlet temperature are used to convert weight into volume. In this context, the measurement uncertainty in the rock-flow cell apparatus is:

- Temperature sensor measurements have an uncertainty of  $\pm 0.1^\circ\text{C}$ .
- The pressure transmitter measurement uncertainty is  $\pm 0.5\%$ .
- The uncertainty of the balance used to weigh the fluids is  $\pm 0.1$  mg.
- The uncertainty related to the gas mixture composition is  $\pm 0.2$  mol%.
- The data acquisition system, Yokogawa FX1000 Paperless Recorder, has a measurement accuracy of  $\pm 0.05\%$  for DCV (Direct Current Voltage) reading and  $\pm 0.15\%$  for RTD (Resistance Temperature Detectors)/TC (thermocouple) reading.

The methodology employed to estimate the amount of hydrate formed is also a source of uncertainty (Straume, 2017), as follows:

- Errors from the measured data as the ones listed above.
- Errors in gas composition due to minor gas leakages.
- In the estimation procedure, errors in the assumption of equilibrium conditions at each pressure-temperature step.
- Errors in the premise of the pressure and temperature conditions at which hydrate started forming (input data).
- Errors in the flash calculations, which were performed with the Cubic-Plus-Association (CPA) equation of state, in the density data of the fluids in the system, and under the hydrate equilibrium conditions. All this information is given by the Multiflash® (KBC, 2014) software.

Multiflash® (KBC, 2014) is a commercial software, and the error related to the predictions is unclear. The Multiflash user guide mentioned that the hydrate nucleation measurements result, in general, in an experimental error of  $\pm 2^\circ\text{C}$  and its predictions are usually within this error range.

Moreover, because the composition of the hydrocarbon liquid used in the experiments is not fully known, the effect of the lightweight components on the estimation of the hydrate formed was neglected. However, it can bring supplementary errors during the estimation of the hydrate formed.

In this context, there are many unknown uncertainties related to the experimental procedure and the methodology employed to estimate the amount of hydrate formed which jeopardise the reliability of the overall experimental uncertainty. Therefore, the propagation of uncertainties has not been estimated. However, the size of the error does not affect the objectives of this study.

## 4. RESULTS AND DISCUSSION OF WATER AND SYNTHETIC GAS SYSTEMS

In this chapter, hydrate formation and accumulation in gas-water systems are evaluated by investigating the influence of hydrate structure, liquid loading, subcooling and temperature gradient inside the pipeline under different flow rate conditions to highlight important aspects of hydrate formation and accumulation in multiphase flow. Several experiments for systems composed of fresh water and methane, and fresh water and 74.7 mol% methane / 25.3 mol% ethane gas mixtures were carried out.

The main results and considerations based on these experimental data are presented in the subsection 4.1. From the image processing, the flow conditions of the gas-water systems before hydrate formation and its influence on the hydrate formation and accumulation are studied and presented in subsection 4.2. The effect of parameters such as temperature and liquid loading on the morphology of hydrates deposition and consequently on sloughing and annealing events is discussed in subsection 4.3.

Moreover, in subsection 4.4, the water conversion to hydrates is estimated through pressure and temperature data, giving an approximated amount of hydrates formed. The method applied is the one proposed by Straume (2017). The calculations were carried out in a Microsoft Excel<sup>®</sup> spreadsheet by calling Multiflash<sup>®</sup> (v.6.1.35, 2017) libraries. Subsection 4.5 shows the hydrate formation and accumulation under static conditions, and subsection 4.6 presents a flow risk analysis based on the experimental data.

### 4.1 Hydrate formation in freshwater systems

The experiments presented in this chapter were composed of fresh water and two different gases: (i) pure methane (99.995%), which forms an sI structure, and (ii) a mixture of 74.7 mol% methane / 25.3 mol% ethane, which forms an sII structure. The gas mixture allows reaching higher subcooling compared to pure methane gas under the same pressure conditions, as observed in the hydrate equilibrium curve presented in subsection 3.3. A total of 39 experiments were conducted by varying the liquid

loading from 20 %vol. to 60 %vol., the rock-flow cell oscillation from 6 to 18.75 rpm, and the bottom wall temperature from 4 to 10°C. The level of pressure and temperature in the system was kept close to 70 bar and 24°C at the beginning of the experiment. The set of experiments performed in gas-water systems and the exact pressure of each experiment during the onset of the hydrate formation are presented in Table 4.1.

The experiments ran for 48 hours after the onset of the hydrate formation or until the pressure decrement was too low, indicating that a steady state was reached. The time of the experiment from the beginning of the hydrate formation to the beginning of the dissociation process is presented in Table 4.1 as  $\Delta t$ . The time elapsed between the time the system entered the hydrate-forming region and the beginning of hydrate formation,  $t_{\text{hydrate onset}}$ , is also shown in the table. The discrepancies in the elapsed time where the system remains within the hydrate formation zone without forming hydrates varied among the experiments, indicating the stochastic nature of hydrate nucleation.

Table 4.1 also presents the water converted to gas hydrates at the end of each experiment. Most of the experiments were performed without the water memory effect — as the effect will not be present when a hydrate system is heated sufficiently above the hydrate equilibrium temperature, and it does not exist for freshwater systems with no previous hydrate history (Sloan and Koh 2008). The exceptions are experiments #2 to #5 and #8 to #12, where the memory effect was preserved. These experiments are composed of pure methane as gas phase and therefore present a lower driving force, which means that several hours can be needed to promote the hydrate nucleation. Therefore, preserving the hydrate memory effect is a way to promote the formation of hydrates quickly.

The rock-flow cell oscillation allows the simulation of the flow in pipelines. The main difference brought by using the rock-flow cell apparatus regarding pipelines comes from the fluid collision with the walls at the sides of the cell, forming a recirculation region. The predominant flow pattern in all experiments before the onset of the hydrate formation was stratified wavy flow (SW). The gas-water ratio (GWR) is the ratio between the volumes of the gas and the water under the same temperature and pressure conditions. In the oil and gas industry, it is a valuable parameter for characterising the flow behaviour, thence its inclusion in Table 4.1.

Table 4.1— Summary of experiments performed with the respective measured data, estimated water converted and flow risk analysis for fresh water and gas systems.

Exp.	Gas Phase	Hydrate Structure	LL [%vol]	$\omega$ [rpm]	Flow Regime <sup>a</sup>	P <sub>ONSET</sub> [bar]	T <sub>average</sub> [°C]	Subcooling Onset [°C]	t <sub>Hydrate Onset</sub> [h]	$\Delta t$ [h]	Water Converted [%]	GWR	Final Morphology <sup>b</sup>	Flow Risk <sup>c</sup>
1	CH <sub>4</sub>	sI	30	11.25	I	63.82	2.2	6.6	26.46	47.28	30.12	2.36	I	8
2	CH <sub>4</sub>	sI	30	18.75	II	64.82	6.0	3.0	1.14	143.17	43.98	2.36	II <sup>d</sup>	8
3	CH <sub>4</sub>	sI	30	18.75	II	63.32	2.0	6.8	1.58	12.97	23.34	2.36	II	8
4	CH <sub>4</sub>	sI	30	18.75	II	64.08	4.6	4.3	1.62	40.32	36.21	2.36	II <sup>d</sup>	7
5	CH <sub>4</sub>	sI	30	18.75	II	65.2	7.6	1.4	1.55	35.30	17.64	2.36	II <sup>e</sup>	4
6	CH <sub>4</sub>	sI	40	18.75	III	62.46	2.0	6.6	5.65	56.93	29.78	1.50	II <sup>d</sup>	8
7	CH <sub>4</sub>	sI	40	18.75	III	63.58	4.1	4.7	1.55	37.65	27.25	1.50	II <sup>e</sup>	5
8	CH <sub>4</sub>	sI	40	18.75	III	64.22	6.0	2.9	1.73	30.12	14.74	1.50	III	4
9	CH <sub>4</sub>	sI	40	18.75	III	64.46	6.4	2.5	1.15	13.18	18.57	1.50	III <sup>f</sup>	4
10	CH <sub>4</sub>	sI	50	18.75	IV	63.50	6.2	2.6	1.77	31.12	31.41	1.02	III <sup>g</sup>	4
11	CH <sub>4</sub>	sI	50	18.75	IV	61.76	6.0	2.5	1.87	37.62	14.47	1.02	III <sup>h</sup>	3
12	CH <sub>4</sub>	sI	50	18.75	IV	61.70	6.1	2.4	1.88	28.22	09.64	1.02	III <sup>h</sup>	3
13	CH <sub>4</sub> +C <sub>2</sub> H <sub>6</sub>	sII	20	18.75	II	64.71	14.4	2.1	0.40	60.90	18.51	3.71	II <sup>e</sup>	5
14	CH <sub>4</sub> +C <sub>2</sub> H <sub>6</sub>	sII	20	18.75	II	61.05	5.4	10.7	1.87	48.12	98.00	3.63	II	8
15	CH <sub>4</sub> +C <sub>2</sub> H <sub>6</sub>	sII	20	18.75	II	63.89	14.3	2.2	1.92	48.39	21.61	3.63	II <sup>e</sup>	5

Table 4.1— Summary of experiments performed with the respective measured data, estimated water converted and flow risk analysis for fresh water and gas systems.

Exp.	Gas Phase	Hydrate Structure	LL [%vol]	$\omega$ [rpm]	Flow Regime <sup>a</sup>	P <sub>ONSET</sub> [bar]	T <sub>average</sub> [°C]	Subcooling Onset [°C]	t <sub>Hydrate Onset</sub> [h]	$\Delta t$ [h]	Water Converted [%]	GWR	Final Morphology <sup>b</sup>	Flow Risk <sup>c</sup>
16	CH <sub>4</sub> +C <sub>2</sub> H <sub>6</sub>	sII	20	11.25	I	63.81	14.2	2.3	1.82	48.91	20.48	3.63	I	5
17	CH <sub>4</sub> +C <sub>2</sub> H <sub>6</sub>	sII	20	11.25	I	63.76	14.1	2.3	1.85	47.65	19.62	3.63	I	5
18	CH <sub>4</sub> +C <sub>2</sub> H <sub>6</sub>	sII	20	11.25	I	63.81	14.3	2.2	1.84	48.82	22.66	3.63	I	5
19	CH <sub>4</sub> +C <sub>2</sub> H <sub>6</sub>	sII	20	06	I	62.93	14.1	2.3	1.87	48.18	20.40	3.63	I	4
20	CH <sub>4</sub> +C <sub>2</sub> H <sub>6</sub>	sII	20	06	I	60.79	13.3	2.8	1.89	48.25	19.26	3.63	I	4
21	CH <sub>4</sub> +C <sub>2</sub> H <sub>6</sub>	sII	20	06	I	60.49	13.8	2.3	1.88	48.20	20.58	3.63	I	4
22	CH <sub>4</sub> +C <sub>2</sub> H <sub>6</sub>	sII	40	18.75	III	57.74	4.0	11.7	1.84	48.16	37.62	1.41	II	8
23	CH <sub>4</sub> +C <sub>2</sub> H <sub>6</sub>	sII	40	18.75	III	57.86	5.5	10.3	1.87	48.04	35.39	1.41	II <sup>i</sup>	8
24	CH <sub>4</sub> +C <sub>2</sub> H <sub>6</sub>	sII	40	18.75	III	58.33	7.0	8.8	1.66	50.33	34.88	1.41	II <sup>i</sup>	7
25	CH <sub>4</sub> +C <sub>2</sub> H <sub>6</sub>	sII	40	11.25	III	57.32	4.0	11.6	1.89	48.22	34.89	1.41	II	8
26	CH <sub>4</sub> +C <sub>2</sub> H <sub>6</sub>	sII	40	11.25	III	57.70	5.5	10.2	1.91	48.13	36.93	1.41	II <sup>i</sup>	8
27	CH <sub>4</sub> +C <sub>2</sub> H <sub>6</sub>	sII	40	11.25	III	58.09	7.0	8.8	2.74	48.11	35.34	1.41	II <sup>i</sup>	6
28	CH <sub>4</sub> +C <sub>2</sub> H <sub>6</sub>	sII	40	06	III	57.02	4.0	11.6	2.86	48.79	31.21	1.41	II	7
29	CH <sub>4</sub> +C <sub>2</sub> H <sub>6</sub>	sII	40	06	III	57.26	5.5	10.2	2.81	48.15	36.63	1.41	II <sup>i</sup>	6
30	CH <sub>4</sub> +C <sub>2</sub> H <sub>6</sub>	sII	40	06	III	57.58	6.9	8.8	2.76	49.74	32.62	1.41	II <sup>i</sup>	6



Table 4.1— Summary of experiments performed with the respective measured data, estimated water converted and flow risk analysis for fresh water and gas systems.

Exp.	Gas Phase	Hydrate Structure	LL [%vol]	$\omega$ [rpm]	Flow Regime <sup>a</sup>	P <sub>ONSET</sub> [bar]	T <sub>average</sub> [°C]	Subcooling Onset [°C]	t <sub>Hydrate Onset</sub> [h]	$\Delta t$ [h]	Water Converted [%]	GWR	Final Morphology <sup>b</sup>	Flow Risk <sup>c</sup>
31	CH <sub>4</sub> +C <sub>2</sub> H <sub>6</sub>	sII	60	18.75	IV	61.97	8.7	7.6	2.56	48.10	19.08	0.66	III	4
32	CH <sub>4</sub> +C <sub>2</sub> H <sub>6</sub>	sII	60	18.75	IV	63.27	12.2	4.2	2.73	48.10	18.39	0.66	III	5
33	CH <sub>4</sub> +C <sub>2</sub> H <sub>6</sub>	sII	60	18.75	IV	63.46	14.4	2.1	2.64	48.29	16.64	0.66	III <sup>f</sup>	5
34	CH <sub>4</sub> +C <sub>2</sub> H <sub>6</sub>	sII	60	11.25	IV	60.22	5.5	10.5	2.70	48.38	18.22	0.66	III <sup>f</sup>	4
35	CH <sub>4</sub> +C <sub>2</sub> H <sub>6</sub>	sII	60	11.25	IV	60.10	5.6	10.4	2.68	48.16	18.13	0.66	III	4
36	CH <sub>4</sub> +C <sub>2</sub> H <sub>6</sub>	sII	60	11.25	IV	60.42	7.0	9.1	2.61	48.03	17.67	0.66	III	4
37	CH <sub>4</sub> +C <sub>2</sub> H <sub>6</sub>	sII	60	06	IV	59.30	4.0	11.9	2.41	48.16	16.14	0.66	III	4
38	CH <sub>4</sub> +C <sub>2</sub> H <sub>6</sub>	sII	60	06	IV	59.51	5.5	10.5	2.68	48.25	17.23	0.66	III	4
39	CH <sub>4</sub> +C <sub>2</sub> H <sub>6</sub>	sII	60	06	IV	62.87	15.0	1.3	2.82	48.09	17.23	0.66	III	6

<sup>a</sup> Refer to the map of Figure 4.4, which classifies the water flow regime in the rock-flow cell before the beginning of hydrate formation.

<sup>b</sup> Refer to the map of Figure 4.6, which classifies the final morphology of the gas-hydrate-water system.

<sup>c</sup> Refer to the risk of disruption under the given experimental conditions based on the morphology and associated risk, Figure 4.30.

<sup>d</sup> More pronounced observations of the annealing process. The hydrate wall deposits pack in the centre of the pipe.

<sup>e</sup> In these experiments, the cross-section of the rock-flow cell was not fully blockaded by the hydrate deposit. Upper wall hydrate deposit at the edge and bottom wall deposit in the middle of the cell were observed.

<sup>f</sup> Absence of a liquid phase at the end of the experiment.

<sup>g</sup> Sloughing events occurred throughout the experiments. The last detachment of the hydrate deposit led to a blockage of the cross-section of the pipe with a flowable water phase.

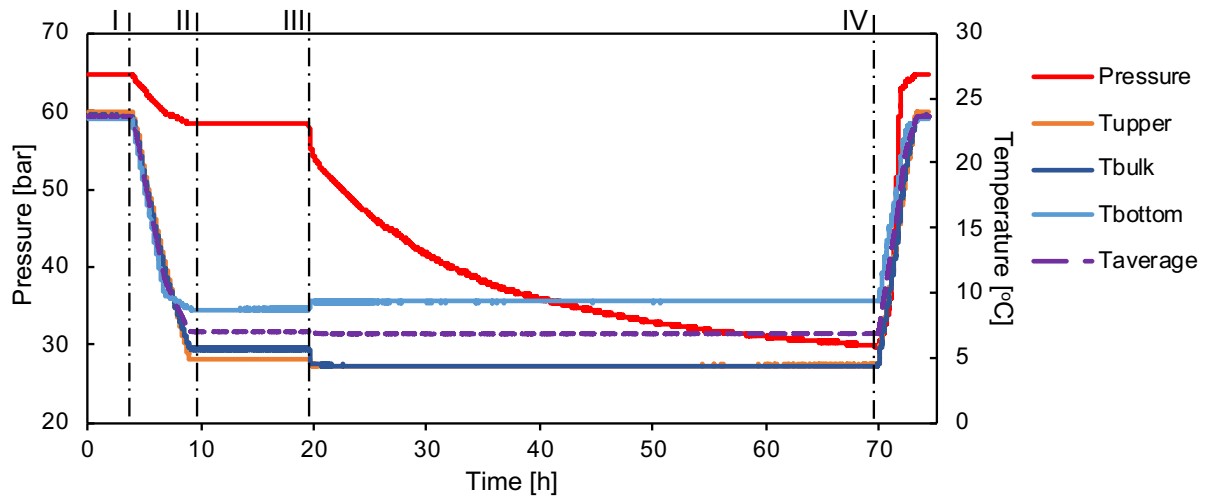
<sup>h</sup> Sparse hydrate wall deposit at the beginning of the hydrate formation — which persisted only for experiment #11— and a non-viscous flowable slurry was observed at the end.

<sup>i</sup> The gradient of temperature imposed in the cell benefits the packing of the hydrate deposit in the upper region at the end of the experiment.

Typical pressure and temperature profiles measured during an experiment are presented in Figure 4.1. The experiments can be split into four stages (vertical dash-dotted lines in the figure). The methodology used, forcing a temperature gradient inside the rock-flow cell to promote upper wall deposition, interferes with the estimation of the internal temperature of the rock-flow cell. The average experimental temperature,  $T_{average}$ , is estimated as the median between the average temperature of all bottom wall sensors and the average temperature of all upper wall and bulk sensors, Eq.4.1.

$$T_{average} = \frac{1}{2} \left\{ \frac{1}{2} \left[ \frac{T_{upper1} + T_{upper2} + T_{upper3}}{3} + \frac{T_{bulk1} + T_{bulk2} + T_{bulk3}}{3} \right] + \frac{T_{bottom1} + T_{bottom2} + T_{bottom3}}{3} \right\} \quad \text{Eq.4.1}$$

Figure 4.1— General pressure and temperature variations trends over time for experiments conducted under isochoric conditions. Stage I is the time required for liquid/gas solubility. Stage II is the beginning of experiment #24 (40 %vol. LL and 18.75 rpm). At stage III, the system remains inside the hydrate formation region without visible hydrate formation. Stage IV represents the end of the experiment, which occurred approximately 48 hours after the beginning of the hydrate formation.



Source: own authorship.

During stage I in Figure 4.1, the system is kept under oscillatory motion and under constant pressure and temperature conditions. At this point, gas is solubilised into the water. The rock-flow cell is cooled down to the experimental temperature in stage II. Because the experiments are isochoric, the pressure drops as the gas compressibility and solubility ratio change at this stage.

The onset of the hydrate formation occurs when the pressure and temperature conditions are within the hydrate formation envelope delimited by the pressure-temperature equilibrium curve. However, hydrate nucleation is a stochastic process. Cooling down the system a few degrees below the hydrate equilibrium condition is often necessary to promote enough driving force to initiate hydrate formation (Sloan and Koh 2008).

The system is meta-stable in stage III; that is, the system is inside the envelope of hydrate formation, but hydrates have not yet formed. The time elapsed between the fluid cooled below the hydrate equilibrium temperature and the hydrate formation onset is also known as *induction time*. That time stands for the initial clustering process until it reaches the critical nuclei size, and the growth time is the time until a crystal volume that can be macroscopically detected is formed. Because of the stochastic clustering process, the start of the hydrate formation can also occur during stage II, when the system is still being cooled, as long as the system is within the hydrate formation zone.

A steep slope identifies the onset of the hydrate formation in the pressure curve — a consequence of the gas consumption required to form the crystals in an isochoric procedure. Another indicator is the temperature increment owing to the exothermic nature of hydrate formation. This is indicated in Figure 4.1 by a vertical dash-dotted line and marks the transition to stage IV.

As it can be seen in Figure 4.1, the hydrate formation rate is higher in the first hours of the experiment and then it slows down, causing an asymptote in the pressure measurement. At the end of stage IV, the pressure and temperature reach steady conditions, or the elapsed time between the beginning of the hydrate formation exceeds 48 hours. Hydrates are then dissociated. The dissociation process returns the cell to the initial conditions, assuring that no leakage had occurred during the experiment.

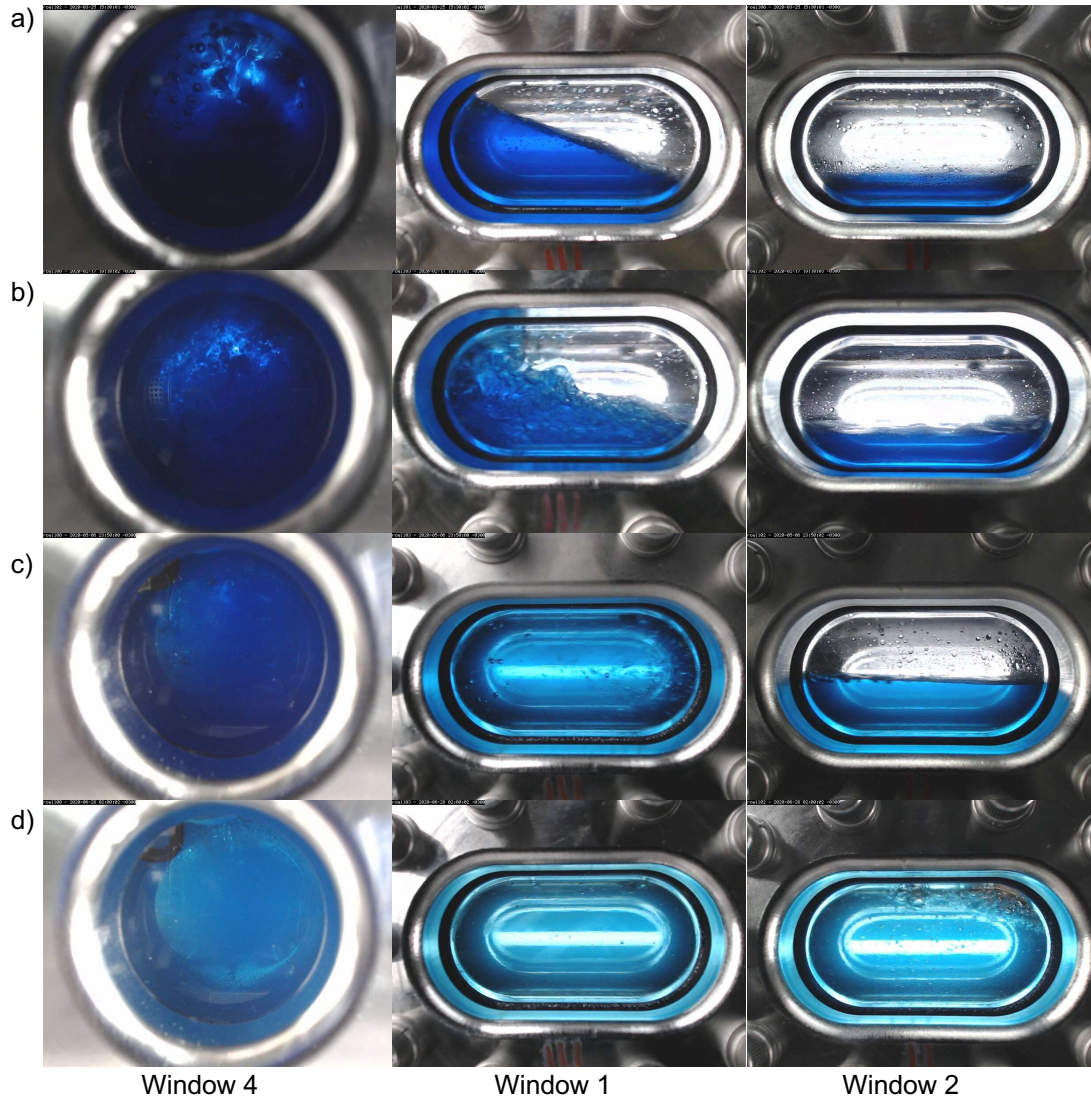
## **4.2 Flow conditions before hydrate formation onset**

This section presents the gas-water flow conditions before the beginning of the hydrate formation by varying the liquid loadings (20 %vol. to 60 %vol.) and the rock-flow cell oscillations (6, 11.25 and 18.75 rpm). This would prove important to

understand the system morphology in the presence of gas hydrates. The different oscillation rates and liquid loading affects the dispersion of the phases (interfacial area and gas diffusion), flow energy (wall shear stress and impact of the fluid at the extremities of the rock-flow cell) and changes the wet surface perimeter, thus influencing the upper wall hydrate deposition.

Figure 4.2 presents photos of the gas-water flow conditions before the onset of the hydrate formation. Four distinct flow conditions were observed. They are all stratified-wavy flows in varied shapes, differing mainly with regard to the wall surfaces where the water can wet or not. The main goal here is to understand the ability of the water to touch the upper wall, depending on the liquid loading and the rock-flow oscillation rate. This will be later related to where the hydrate deposits form.

Figure 4.2— Captured images of the rock-flow experiments showing the highest liquid level in each window before the onset of the hydrate formation. a) Water never touches the upper wall of windows 1 and 2 (experiment #18, 20 %vol. LL and 11.25 rpm). b) Water partially touches the upper wall of window 1, but does not touch window 2 (experiment #13, 20 %vol. LL and 18.75 rpm). c) Water completely touches the upper wall of window 1, but does not touch window 2 (experiment #27, 40 %vol. LL and 11.25 rpm). d) Water touches all walls of the rock-flow cell (experiment #36, 60 %vol. LL and 11.25 rpm).

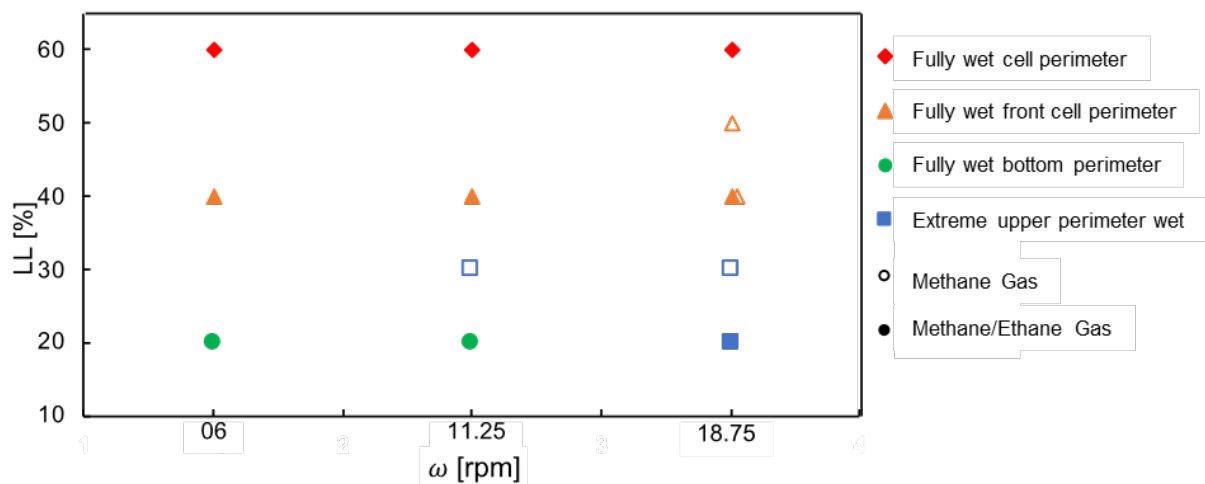


Source: own authorship.

Based on the footage, the classification of these four flow conditions based on liquid loading versus oscillation rate is presented in Figure 4.3. In the legend, the fully wet cell perimeter (red rhombus) means that the water phase wetted all windows during the motion of the rock-flow cell. The fully wet front cell perimeter (orange triangles) means that the water does not touch the upper wall of window 2. The fully wet bottom perimeter (green circles) means that only the bottom region of all windows is wetted except window 4, which is thoroughly wetted by the water because of the

motion of the rock-flow cell. Extreme upper perimeter wet (blue square) means that the upper wall of the edge windows (windows 1 and 2) is wetted, and the water does not wet the upper wall of the window 2. Solid symbols represent the experiments with water and gas mixture, whereas hollow symbols represent the ones with water and methane gas.

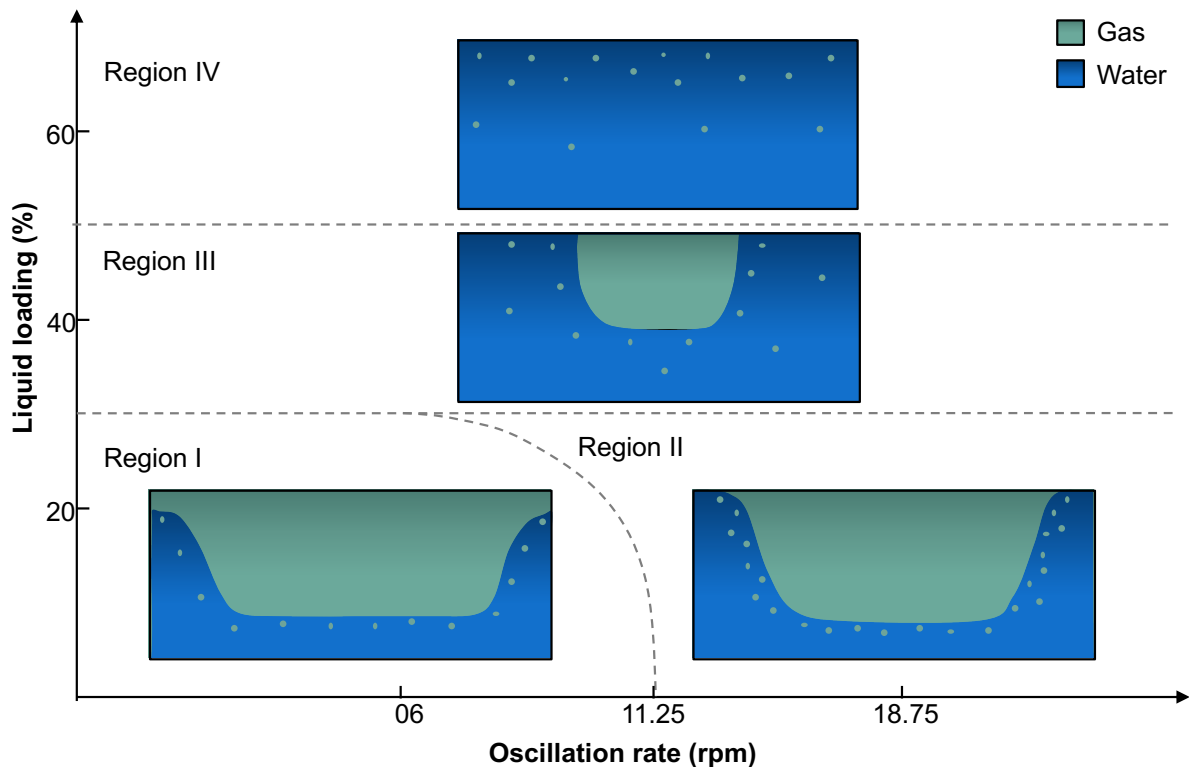
Figure 4.3— Classification of the wet perimeter for the gas-water system based on liquid loading and oscillation rate in the rock-flow cell before the onset of the hydrate formation. In the legend, rhombic symbols mean that all windows were wetted during the motion. Triangular symbols: the water phase does not touch the upper wall of the window 2. Circular symbol: the bottom of all windows was wetted except window 4. Squared symbols: the upper wall of the edge windows was wetted (windows 1 and 3). Solid symbols represent methane/ethane gas mixture, whereas hollow symbols represent methane gas experiments.



Source: own authorship.

The description of the flow conditions before the onset of hydrate formation described in Figure 4.2 and Figure 4.3 were summarised in a flow map as the one presented in Figure 4.4.

Figure 4.4— Illustration of a gas-water flow map in the rock-flow cell before the onset of the hydrate formation as a function of the liquid loading and of the oscillation rate. The categorisation was based on the footage of the rock-flow cell experiments.



Source: own authorship.

The four regions in the flow map were classified mainly according to:

- Region I: The fluid never touches the upper wall, Figure 4.2 (a). According to Figure 4.3, it happens for liquid loadings lower than 30 %vol. at oscillation rates below 11.25 rpm.
- Region II: The liquid partially touches the upper wall of the edge windows (windows 1 and 3), but it does not touch window 2, Figure 4.2 (b). From Figure 4.3, that happens for liquid loadings lower than 30 %vol. at oscillation rates above 11.25 rpm.
- Region III: The fluid completely touches the wall of the edge windows (window 1 and 3) but does not touch the upper wall of window 2, Figure 4.2 (c). From Figure 4.3, that happens for liquid loadings in between 30 %vol. and 50 %vol. regardless of the oscillation rate.

- Region IV: The liquid touches the upper wall in all windows of the rock-flow cell, Figure 4.2 (d). As presented in Figure 4.3, that happened for higher liquid loadings, greater than 50 %vol., regardless of the oscillation rate.

Basically, higher liquid loadings and/or higher oscillation rates favour the wetting of the top wall region by the fluid flow. Afterwards, these classifications provided insight into the process of hydrate wall deposition in gas-water systems based on the wetted wall surface, as discussed in subsection 4.3. Besides, the hydrate growth rate is controlled by the mass transfer, thence the gas-liquid interface must be considered, which is influenced by the flow conditions, as it affects the diffusion of the gas molecules from the gas phase to the bulk phase, and from the dissolved gas to the hydrate interface.

### **4.3 Characterization of hydrate formation and accumulation**

The mechanism of hydrate formation and accumulation is a crystallisation process. Hydrates may nucleate on all gas-water interfaces because of the lower Gibbs free energy of nucleation on the interface and because it is the site of the highest concentration of the compounds (water and gas) with regard to the bulk of either the gas or the water phase (Sloan and Koh, 2008). Notice that the motion of the fluids increases the interfacial surface among gas-liquid-hydrate crystals and promotes the entrance of these structures into the liquid, deceiving the researcher into believing that the hydrate formation has occurred in the bulk.

Moreover, once the pipe wall is water-wet and when in contact with the gas phase, a natural site for hydrate nucleation is formed because of the pipe wall roughness, which can favour the nucleation, and the lower temperature when compared to the bulk flow temperature. Consequently, hydrate forms on the gas-water interface and on the pipe surface, sticking to the wall. In addition, the formed hydrate crystals may act as a solid surface creating new nuclei.

Hydrate nucleation, which is a stochastic event, occurs somewhere between the beginning of the pressure signal drop and the visual detection of the first hydrate seeds. However, hydrate nucleation is out of the scope of this thesis, and the



experimental apparatus was not equipped to detect it. Following the nucleation, hydrate crystals start to grow. Hydrate growth is mass- and heat-transfer limited. In this process and for hydrate particles in the bulk, the gas should diffuse from the gas-liquid interface to the liquid bulk, then from the liquid bulk to the hydrate-liquid interface to be incorporated into the hydrate water-wet interface. The gas consumption is due to the formation of hydrates (new particles) and the conversion of the water trapped inside capillaries in the hydrate structure near a particle's outer surface (hydrate growth). Hence, the motion of the fluid in the pipe (high or low turbulence), the liquid loading and the cell temperature might influence the growth rate and, consequently, the hydrate morphology.

Therefore, for the rock-flow cell experiments herein described, the hydrate growth rate is higher at the beginning of the crystallisation process and slows down throughout the experiment — five minutes to one hour after the onset of formation — reaching an asymptotic behaviour at the end. The formation and growth of hydrates lead to increased liquid viscosity and result in shear rate changes.

The porous hydrate structure may form liquid bridges that can stick the hydrate particle to the wall, causing the particle to crystallise on the said wall (particle deposition). This process is also known as *consolidation*. If the liquid flow is able to wet the upper surface, hydrate particles may stick to the upper region of the pipe as a consequence of the flow energy which will be discussed soon (subsection 4.3.1).

The particle sticking on the wall forms a solid structure. When this structure is wetted again because of the motion of the rock-flow cell, hydrate particles in the bulk adhere to the solid structure forming liquid bridges again, which can consolidate increasing or disrupting the deposit by washing the hydrate particles which were weakly attached or by detaching pieces of the solid hydrate structure because of the shear caused by the flow. The consolidation efficiency will depend on the cohesive force between hydrate-hydrate particles, contact time to consolidate the liquid bridge and the shear stress, which causes the disruption of the aggregates because of the flow motion.

In the case of gas-hydrate-water systems, a macroscopic agglomeration of gas hydrates does not occur because no liquid bridge forms between particles in the absence of another liquid phase (oil phase, for example). Those bridges promote the

necessary force for hydrate agglomeration in oil-gas-water systems, for instance, differing from what is herein described. Therefore, for the gas-water system, the hydrate accumulation process is more related to the aggregation of hydrate particles followed by their consolidation.

The experiments herein described presented the following conditions: (i) hydrate plug formation, (ii) cross-section reduction due to wall deposition, (iii) upper wall deposition, (iv) sloughing events and (v) a transportable hydrate slurry. Each of these conditions will be analysed separately in the following subsections.

Figure 4.5 presents photos of the rock-flow cell experiments #20 (20 %vol. LL and 06 rpm), #25 (40 %vol. LL and 11.25 rpm), and #39 (60 %vol. LL and 06 rpm) showing the main morphologies observed at the end of most of the experiments presented in Table 4.1. Therefore, the hydrate morphology can be summarised into three main categories: bottom wall deposit, upper wall deposit, and a mixed condition presenting upper and bottom wall deposits. The separation of the temperature control of the top and bottom walls of the rock-flow cell does not appear to have a considerable effect on the location of the hydrate deposit. The process of hydrate deposition might be more sensitive to parameters other than the wall temperature.

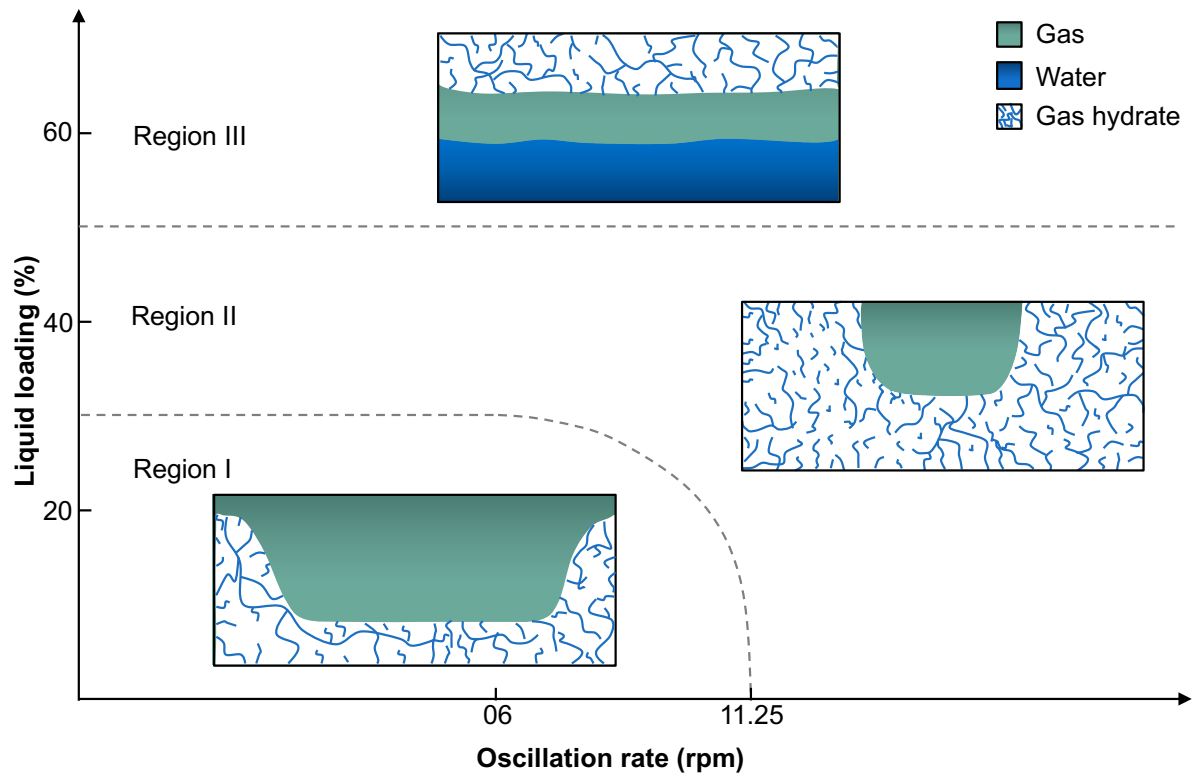
Figure 4.5— Captured images of the rock-flow cell experiments taken 48 hours after the beginning of the hydrate formation showing the final hydrate morphology: a) experiment #20 (20 %vol. LL and 06 rpm) presents a bottom wall deposit, b) experiment #25 (40 %vol. LL and 11.25 rpm) shows a plug formation at the edges of the rock-flow cell, c) experiment #39 (60 %vol. LL and 06 rpm) show a thicker upper wall deposit with some unconverted water at the bottom.



Source: own authorship.

Based on the footage, the morphology of the hydrate deposits observed in the rock-flow cell windows at the end of the experiments as a function of liquid loading and oscillation rate were presented in Figure 4.6. It can be observed that the transition curves are similar to the ones of the gas-water flow map shown in Figure 4.4, except for Regions II and III which were united because they presented the same final hydrate morphology — the hydrate deposition occurred in the region where the aqueous phase could arrive according to the flow conditions before the beginning of the hydrate formation. This emphasises that the hydrodynamics of the gas-water flow before the onset of the hydrate formation has a significant role in forming the hydrate deposits.

Figure 4.6— Final hydrate morphology as a function of liquid loading and oscillation rate based on a characteristic gas-water flow map for rock-flow cell experiments. The captured images at three different positions of the rock-flow cell — side window —(window 4), left front window (window 1), and window 2 (window 2) were the basis for the categorisation.



Source: own authorship.

Three distinct regions were observed:

- Region I: the combination of the liquid loading and the oscillation rate does not allow the liquid phase to touch the upper surface of the pipeline, promoting only bottom wall deposition.
- Region II: is a transition region, as the set of liquid loading and oscillation rate hampers the deposition in the upper middle region of the cell, whereas varies in the edge of the cell from bottom to complete wall deposition.
- Region III: the liquid phase wets the entire surface of the pipe wall regardless of the oscillation rate. Hydrate particles accumulate in the upper wall region, forming an upper wall deposition with or without a liquid phase at the bottom of the cell.

#### 4.3.1 Wave effect

Figure 4.7 shows the captured images from an experiment illustrating the mechanism leading to the formation of hydrate deposits. The first picture is on the verge of the onset of the hydrate formation (Figure 4.7.a). The beginning of the hydrate formation, by visual observation, occurred in the liquid phase (Figure 4.7.b) and stacked to the wall with the contraction of the flow (Figure 4.7.c). Basically, hydrate particles are driven onto the wall by waves due to the flow conditions and the liquid bridges which hold them attached to the wall. Gradually, the liquid bridge, that keeps the hydrate particles adhered to the wall crystallises, consolidating the particles on the wall. The expansion of the flow, that is, a second wave, ends up bringing some of the hydrate particles in the bulk whilst dragging some of the hydrate particles attached to the surface of the hydrate deposit (Figure 4.7.d). The successive waves gradually increase the surface of the deposit, Figure 4.7 (e) and (f). The hydrate particles tend to accumulate and aggregate in the pipe's upper region, forming a thicker hydrate deposit because of the lower flow energy in this region and the gas phase contact. The waves and their frequency influence the hydrate deposit profile. Figure 4.7 (g) and (h) show the state of the wall 140 and 200 seconds after the beginning of the hydrate formation (Figure 4.7.b).

Figure 4.7— Images captured before the onset of the hydrate formation a) of experiment #28 (40 %vol. LL and 06 rpm), at the beginning of the hydrate formation b), hydrates adhered to the wall c), after the first wave due to the oscillation of the rock-flow cell d), second wave e), third wave f), 140 and 200 seconds after the beginning of the hydrate formation g) and h), respectively.

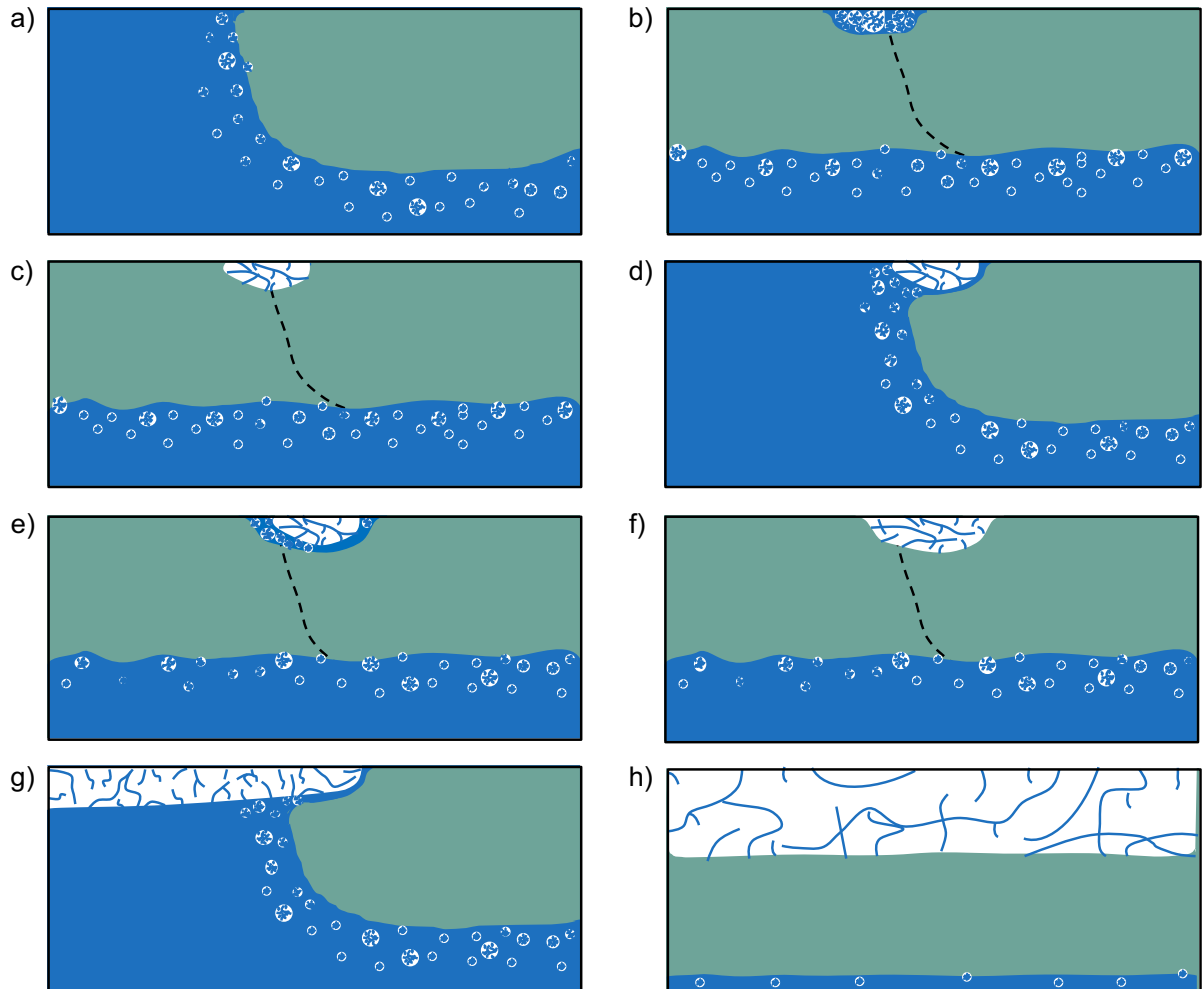


Source: own authorship.

Through the analysis of these captured images, a scheme for the process of hydrate wall deposition was devised and implemented by fixing one of the windows of the rock-flow cell (window 1). Figure 4.8 (a) shows the wavy motion of the gas-liquid interface occurring in the rock-flow cell apparatus. When the particles nucleate in the water bulk, they tend to float on the gas-water interface. The wavy motion causes the collision of the particles against the wall. The impact of the fluid (water with hydrate

particles) on the wall when in contact with the gas phase causes the formation of liquid bridges. The retraction of the fluid owing to the flow motion, Figure 4.8 (b), added to the consolidation of the liquid bridge, which is time-dependent, causes the hydrate particles to adhere to the wall as the energy required for detachment is low, Figure 4.8 (c). The expansion of the fluid, the second wave due to the motion of the rock-flow cell, Figure 4.8 (d), moistens the surface of the hydrate deposit and renews the surface with hydrate particles presented in the bulk. But the expansion of the fluid also provides energy to detach the hydrate deposit or wash away the particles of hydrates, if they are not consolidated, in the surface of the hydrate deposit depend on the flow conditions. The retraction of the liquid phase promotes the crystallisation of the hydrate particles and the growth of the deposit, Figure 4.8 (e-f). The continuous motion of the rock-flow cell supplies the surface of the deposit with hydrate particles that float in the bulk, moisten the surface of the deposit with the water phase during the wave expansion, and expose the deposit surface to the gas phase during the retraction of the wave. Consequently, the hydrate deposit grows continuously, Figure 4.8 (g). The dotted line represents the gas-liquid interface position before the contraction of the flow because of the motion of the rock-flow cell.

Figure 4.8— Illustration of the process of hydrate particle attachment to the wall observed during the experiments: a) hydrate particles in the bulk; b) hydrate particles, which have collided with the wall due to the motion of the cell, adhered to the pipe wall because of the formation of a liquid bridge; c) the retraction of the liquid phase favours the consolidation of the liquid bridge on the wall; d) hydrate deposits being wetted by the second wave of the flow; e) the retraction of the liquid phase causes the growth of the deposit because of the contact with hydrate formers and the adhesion of the hydrate particles that were floating in the bulk; f-g) the motion of the cell continues to bring hydrate formers and hydrate particles to the surface of the deposit which grows continuously; h) formation of thicker hydrate deposits at the end. The illustration of the process of hydrate formation and accumulation was restricted to one of the windows of the rock-flow cell (window 2). The dotted line represents the previous gas-liquid interface before the contraction of the flow due to the motion of the rock-flow cell.



Source: own authorship.

This mechanism was hypothesised by Bassani (2020) and called the *wave effect*. This is the first study that experimentally confirms its existence. The wave effect causes the rapid deposition of hydrates, especially in the upper regions of the wall, whenever the flow conditions allow the particles to collide with the upper wall. It must be emphasised how important it is as the formed deposits can frequently endure gravity forces. The exception is when sloughing occurs a few hours after the deposit



formation, which is peculiar to some experiments and will be discussed in a separate section. The formed deposits reduce the cross-sectional area of the pipeline because of their volume, impairing the flow and increasing the head losses, Figure 4.8 (h).

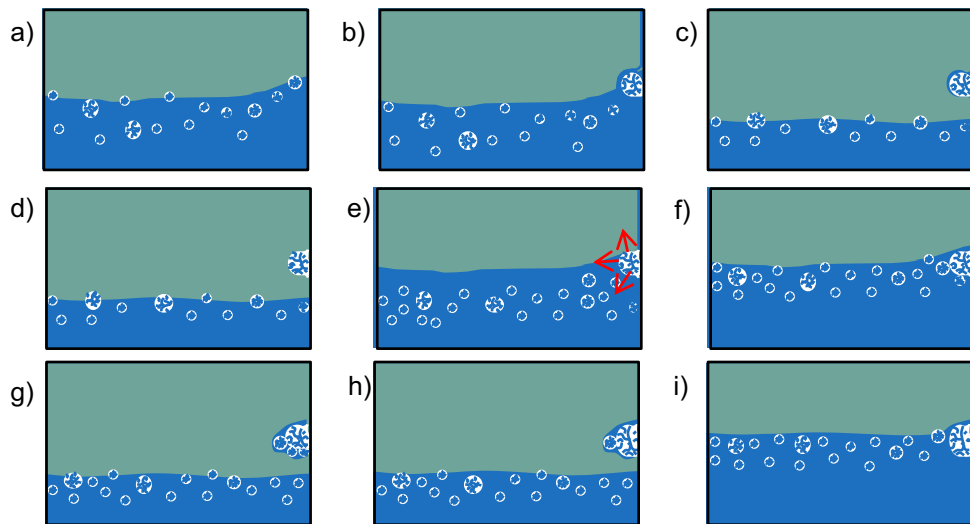
Experiments #6 and #9 (40 %vol. LL and 18.75 rpm) were performed under the same conditions, but different hydrate accumulation behaviours were observed. In one, the hydrate accumulation led to pipeline blockage, whereas in the other the hydrates deposited on the upper wall, leading to a reduction in the cross-sectional area of the pipe. The differences between those two behaviours might originate under subcooling conditions at the onset of the hydrate formation — 6.6°C and 2.5°C for experiments #6 and #9, respectively — which promoted higher hydrate formation for experiment #6. However, the same mechanism involved in the process of hydrate wall deposition, the wave effect, was observed.

Moreover, the gas consumption due to hydrate formation under isochoric conditions decreases the pressure of the system, consequently reducing the driving force and the subcooling throughout the experiment. However, the same hydrate formation and accumulation mechanisms in gas-water systems were observed under isobaric conditions (see Kakitani et al. 2021). Under these conditions, the driving force, that is, the subcooling, is kept constant throughout the experiments — likely an evidence of the low influence of the subcooling on the process of hydrate deposition in gas-hydrate-water systems.

The efficiency of the wave effect in the process of hydrate formation and deposition depends on the collision of the first particle against the wall (flow conditions) and on the rate of crystallisation (time-, mass- and heat-dependent) of the formed liquid bridge. The deposit then grows because more particles collide with it; the flow conditions can keep bringing particles, developing liquid bridges and consolidating with the already-formed deposit. Moreover, the flow conditions can wet the surface of the deposit, providing water, which can crystallise when in contact with the gas phase, increasing the deposit thickness. Figure 4.9 depicts a general process of hydrate deposition as a consequence of the wave effect: a) hydrate particles dispersed in the bulk are carried away by the liquid-phase flow; b) particles collide against the wall and stick to it because of the liquid bridges c); d) the contraction of the liquid phase exposes the particle to the gas phase favouring the fast crystallisation of the liquid bridge and

creating the first layer of the deposit; e) the liquid phase expansion, that is, a second wave, wets the deposit surface providing water to crystallisation; f) the liquid phase flow carried away particles which can collide against the deposit, feeding it with hydrate particles g); if the liquid bridge between the provided particles and the deposit consolidates, the deposit grows h); or the flow may wash hydrate particles out of the outer surface of the deposit, i).

Figure 4.9— Description of the particle deposition process on the wall called wave effect. a) particles dispersed into the bulk; b) collision of the particle against the wall; c) contraction of the flow whereas the particle remains attached to the wall because of the liquid bridge formed on the particle interface, wall and gas phase; d) consolidation of the liquid bridge forming the first layer of the deposit; e) the liquid-phase wets the surface of the deposit once again providing water and new particles which are dispersed into the bulk; f) new particles adhere to the deposit and that may or may not consolidate; g), h) deposit growth due to the crystallisation of the water provided by the flow, conversion of the water trapped inside the porous hydrate particle and the attachment of new particles; i) eventually, the flow motion can wash particles out of the deposit if they are not consolidated and depending on the shear rate.



Source: own authorship.

The liquid bridge causes a binding force that keeps the hydrate particle adhered to the wall. It depends on the time required to consolidate the liquid bridge, the flow energy to avoid the disruption of the liquid bridge, and subcooling. The energy supplied by the gas flow that contributes to the detachment of the hydrate particle that is already adhered to the wall is low, since it comes from the gas motion with low inertia. Furthermore, as the deposit surface is in direct contact with the gas, the crystallisation presents no mass transfer resistances, promoting a fast consolidation of the liquid bridges. The consolidation is so fast, and the gas motion has such a low inertia that deposition is observed within the first minutes after the onset of the hydrate formation.

In a few cases, the deposits are washed out (detached) from the wall during the liquid flow. Those cases will be discussed separately in a section called “Sloughing” (when the deposit forms but detaches after a few hours) or “Transportable hydrate slurry” (when the deposits do not even form, that is, when the detachment caused by the wavy motion of the gas-liquid interface is sufficient to prevent consolidation). These cases are marked by a weaker adhesion force, causing a lesser “fixation” of the hydrate particles to the wall and decreasing their stability.

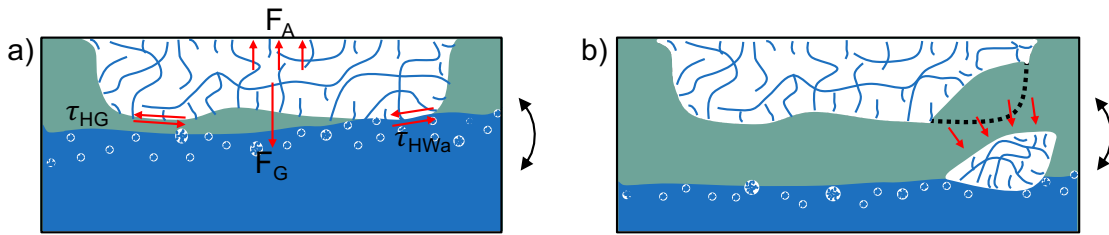
In this context, the flow map presented in Figure 4.4 gives important insight into where the hydrate deposits will form because of the wave effect. Increasing the liquid loading, that is, higher shear rate, the entire cell wall is wetted, and a thicker hydrate deposit on the upper pipe wall was observed, see region III in Figure 4.6.

Under actual conditions, the slug flow pattern is the flow type that more faithfully reproduces the condition described above: intermittent gas/liquid flow and a free hydrate deposit surface with hydrate particles presented in the liquid phase. Yet, it may also occur in restricted flow conditions, possibly leading to the blockage of the pipeline.

#### 4.3.2 Sloughing

The detachment of the hydrates deposits from the upper wall is called *sloughing* and is depicted in Figure 4.10. It is yet another phenomenon observed during the experiments. The sloughing events occur as a structural failure of the hydrate deposit caused by the combination of hydrate porosity, gravity force, flow impact and shear forces acting on the hydrate deposit. The main forces are presented in Figure 4.10 (a): gravity force ( $F_G$ ), adhesion force ( $F_A$ ), shear stress acting on the hydrate deposit due to the gas phase ( $\tau_{HG}$ ), and the liquid phase, which in this case is the water phase ( $\tau_{HWa}$ ). In a sloughing event, the deposit detaches partially or even completely detached from the wall. This leads to pressure drop fluctuations and can quickly trigger flowline plugging threats owing to the release of large chunks of hydrates which can get stuck in flowline restrictions such as curves or valves. Therefore, sloughing events may lead to pipeline blockage being a threat to flow assurance.

Figure 4.10— Illustration of a sloughing event and the forces involved in the mechanism. a) forces presented in the hydrate deposit structure and b) sloughing event.



Source: own authorship.

Figure 4.11 shows the images captured on the verge of the sloughing event, Figure 4.11 (a), during the detachment of a chunk of the hydrate deposit, Figure 4.11 (b) and a second sloughing event right after the first one, Figure 4.11 (c). Higher liquid loading and low subcooling might have increased the unconverted water inside the hydrate deposit structure in the water-methane systems, thus reducing its mechanical stability and promoting sloughing events. In this experiment, a fourth sloughing event occurred approximately 26 hours after the beginning of the hydrate formation, leading to the blockage of a section of the cell. The plug location is marked with a red rectangle in Figure 4.11 (d) and a transportable hydrate slurry flows before the plugging position.

Figure 4.11— Photos from the experiment #10 (50 %vol. LL and 18.75 rpm) showing the rock-flow cell before the sloughing events (a), two consecutive sloughing events (b, c) with time between shots of 2 and 26 seconds after the beginning of the hydrate formation. The red arrow shows the window where the rupture of the hydrate deposit occurred. The red rectangle highlights the window where the plug formation occurred.



Source: own authorship.

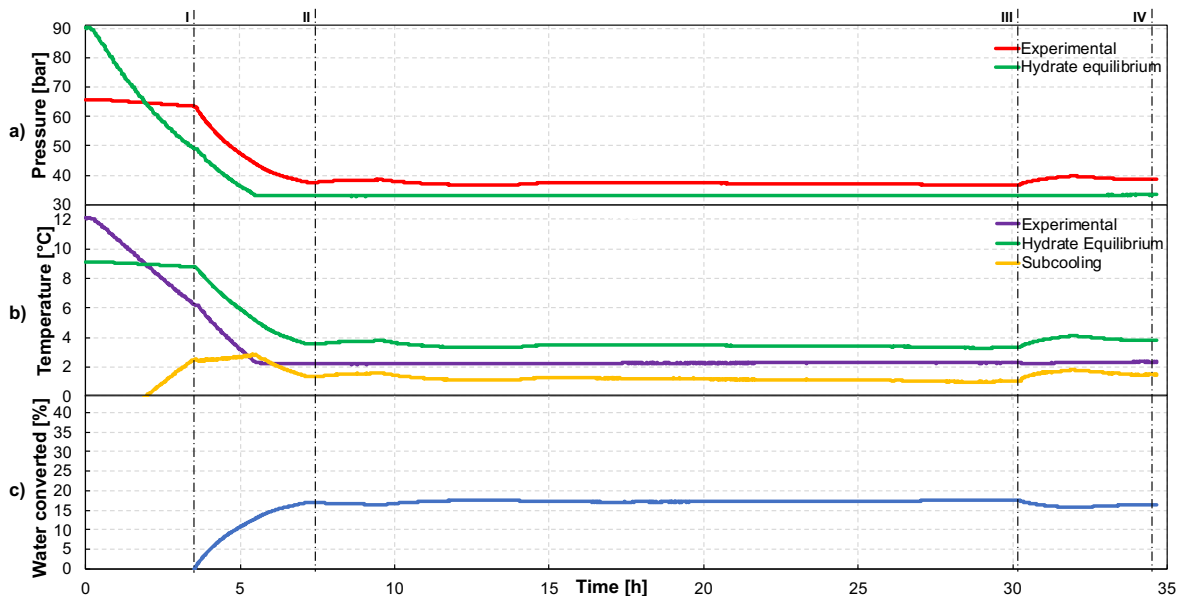
The hydrate sloughing events were only observed in methane gas-water systems, not being observed in the gas mixture-water experiments. The high subcooling imposed by the water-methane/ethane gas system reduces the unconverted water inside the hydrate structure, thus promoting faster water conversion to hydrates and contributing to the stability of the deposit.

The sloughing events were observed in the typical experimental curve as an increase in the pressure curve. It might be due to the release, into the system, of the gas trapped inside the hydrate deposit structure, thus increasing the pressure (red line in Figure 4.12) whilst the temperature remained constant (purple line in Figure 4.12). Two sloughing events occurred during the experiment shown in Figure 4.12, the first corresponding to 13.2 hours (stage II in Figure 4.12) and the second to 29.7 hours (stage III in Figure 4.12). Next, the system pressure decreases as the hydrate rupture

of the deposit increases the contact area between the unconverted water and the formation gas, promoting the formation of new hydrate particles.

In this experiment, the onset of the hydrate formation occurred during the cooling of the systems. This can be identified as the change in the slope of the pressure curve — red line in Figure 4.12.a) whilst the green line presents the hydrate equilibrium pressure curve under experimental temperature conditions.

Figure 4.12— Pressure (a), temperature (b) and water converted (c) into hydrate of experiment #10 (50 %vol. LL and 18.75 rpm). a) the red line is the pressure of the system, which drops as the temperature decreases and gas is consumed to form hydrates; the green line represents the hydrate equilibrium pressure under the same conditions; b) the temperature of the system (purple), hydrate equilibrium temperature (green) and subcooling (yellow), the difference between purple and green lines; c) amount of water converted to hydrates during the experiment. The vertical dashed lines, I to IV, refer to specific events related to hydrate formation and accumulation observed throughout the experiment.



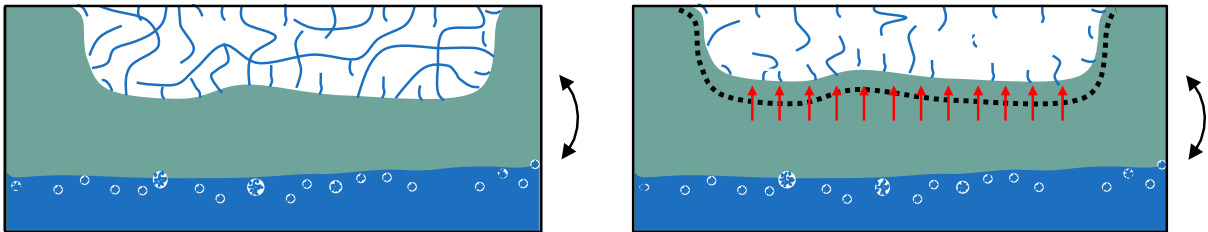
Source: own authorship.

### 4.3.3 Annealing

Rao et al. (2013), Grasso et al. (2014), and Straume (2017) noticed a reduction in the porosity, with consequent structure hardening, of the hydrate deposit during their experiments. The hydrate deposition layer acts as an insulating layer reducing the effective wall heat flux. Since hydrate growth is mass or heat-transfer limited, hydrates eventually stop depositing and start annealing. The annealing process can also be explained as an ageing process. As time passes, gas diffusion occurs in the porous

medium, raising the conversion of the water trapped inside the porous hydrate structure. The porous medium becomes poorer in liquid and, therefore, more resistant to shear. In addition, the conversion of the water trapped inside the porous spaces into hydrates causes a differential of pressure, squeezing the remaining water in the porous pool and shrinking the volume of the hydrate deposit. Consequently, the annealing process decreases the porosity of the hydrate structure leading to the formation of a solid hydrate deposit. Figure 4.13 shows a schematic image of the annealing process in the hydrate deposit structure.

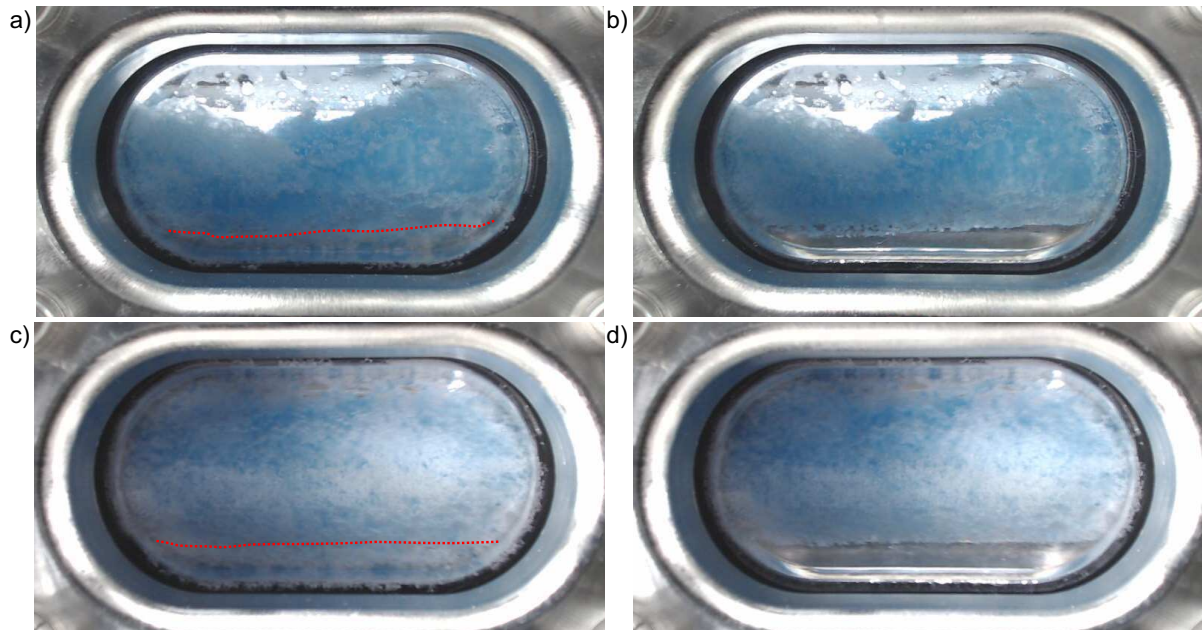
Figure 4.13— Illustration of the annealing process in the hydrate deposit.



Source: own authorship.

As Song et al. (2018) discussed, the annealing process increases the mechanical stability of the deposit, preventing the sloughing events because liquid bridge forces progressively change into solid bridge forces. Some photos of the annealing process are presented in Figure 4.14. The fact that the upper wall temperature in this experiment is lower than the bottom one contributes to the hardening of the hydrate structure in the upward direction. Figure 4.14 a) presents a photo of window 2 of the rock-flow cell, and Figure 4.14 b) presents the same experiment after 24 hours. The same is shown for window 1 in Figure 4.14 c) and Figure 4.14 d) for a 24-hour time lapse between the photos.

Figure 4.14— Photos of experiment #27 (40 %vol. LL and 11.25 rpm) showing the annealing process of the hydrate deposit on windows 2 (a, b) and 1 (c, d). The photos were captured 24 hours (the leftmost figures) and 48 hours (the rightmost figures) after the onset of the hydrate formation. The dotted line in a) and c) shows the height of the deposit after 24 hours (b and d, respectively).



Source: own authorship.

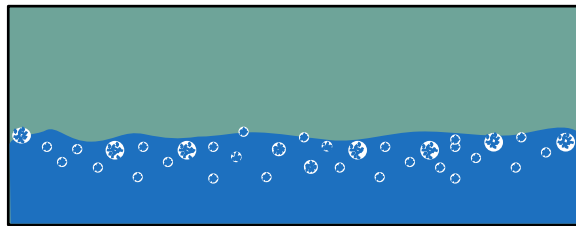
#### 4.3.4 Transportable hydrate slurry

A transportable hydrate slurry was found in the experiments with higher liquid loading (above 50% of liquid) at an experimental temperature close to the hydrate equilibrium temperature. The experiments reached the equilibrium condition a few hours after the hydrate formation onset. These results might indicate that the combination of shear rate and subcooling is important to hydrate management strategies, such as cold flow. However, the conditions are very restricted, at least within the scope of the parameters tested in this study. Only two formed the transportable hydrate slurry, experiments #11 and #12. These experiments were performed with methane as the gas phase. The low hydrate equilibrium temperature inherent to methane gas (low subcooling when compared to a gas mixture under the same experimental condition, for clarity see Figure 3.6) added to the isochoric experimental procedure (which causes the reduction of the subcooling throughout the experiments as the pressure drops because of the consumption of the gas to form hydrates) might be the reason to the formation of a transportable hydrate slurry. In this scenario, there



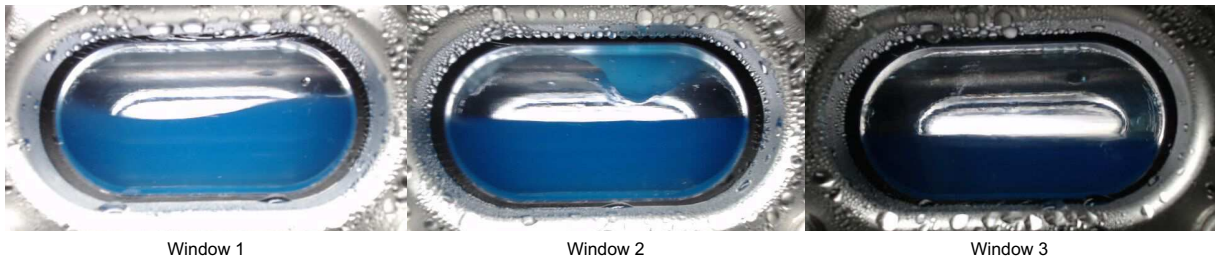
might have been an insufficient driving force to promote the consolidation of the liquid bridges on the wall because of the wave effect. Therefore, the deposit does not form, and the hydrate particles remain dispersed in the flow. However, further studies must be conducted to assess the validity of this statement. Figure 4.15 illustrates a transportable hydrate slurry, whereas Figure 4.16 presents a photo of experiment #11 (50 %vol. LL and 18.75 rpm).

Figure 4.15— Illustration of the formation of a transportable hydrate slurry.



Source: own authorship.

Figure 4.16— Photos from the experiment #11 (50 %vol. LL and 18.75 rpm) where a transportable hydrate slurry was formed.



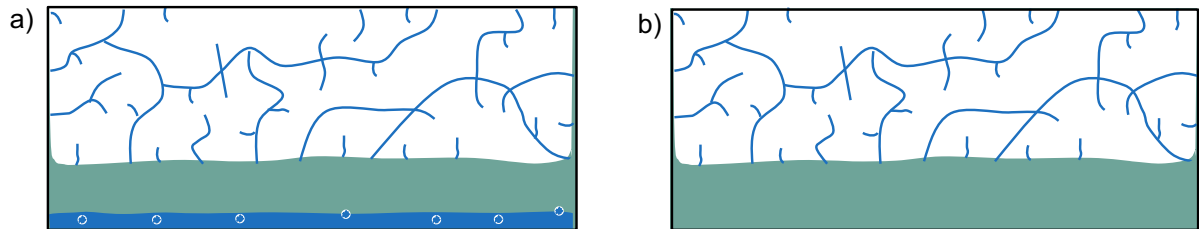
Source: own authorship.

#### 4.3.5 Free water film at the end of the experiment

Upon increasing the liquid loading, a thicker hydrate deposit on the upper pipe wall was observed for the experiments carried out with the methane/ethane mixture as the gas phase. Figure 4.17 illustrates this observation. The wave effect added to the higher liquid flow energy, as high liquid loadings increase the energy of the liquid-phase flow, might have contributed to the accumulation of hydrate particles at the upper region of the pipe, promoting the formation of a thicker and more stable deposit. However, when the liquid loading is sufficiently high (from Figure 4.6, of 60 %vol. or above), the hydrate deposit structure cannot trap all existing water in the system. In

those cases, a free water film remains at the bottom of the rock-flow cell until the end of the experiment.

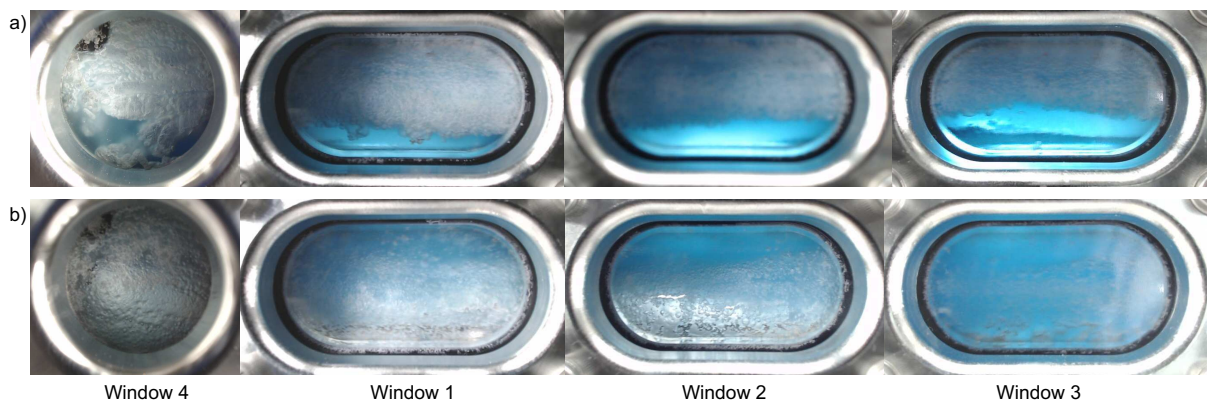
Figure 4.17— Illustration of the thicker hydrate deposit a) with and b) without a free water film observed at the end of some experiments.



Source: own authorship.

However, a free water film was not observed in two experiments, namely #32 and #33 (60 %vol. LL and 18.75 rpm), in Table 4.1. This might be due to the lower subcooling at the beginning of the hydrate formation compared to the other experiments carried out at the same liquid loading, which might have helped to trap all the free water phases inside the hydrate porous deposit. Figure 4.18 shows the thicker hydrate deposits with and without a free water layer at the end of experiments #31 and #32, respectively.

Figure 4.18— Photos of experiment #31 (60 %vol. LL and 18.75 rpm): a) showing the thicker hydrate deposit with a free water film and experiment #32 (60 %vol. LL and 18.75 rpm) and b) without the free water film.

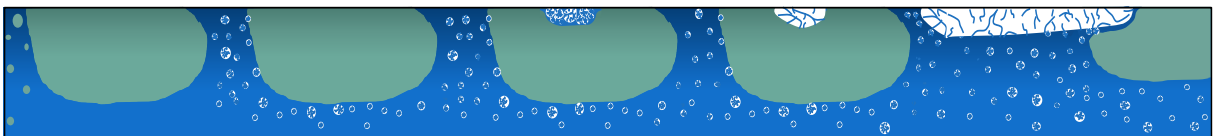


Source: own authorship.

#### 4.3.6 Conceptual model of hydrate formation and accumulation in water-dominated system

The driving forces promoting hydrate nucleation, growth and accumulation depend on the gas composition, the heat and mass transfer rates, the pressure and temperature conditions, the fluid hydrate history (that is, the memory effect of the water phase), and on flow features (Sloan et al., 2011). Figure 4.19 summarises, concisely, the process of hydrate formation and accumulation observed in water-continuous systems. The flow causes the gas-liquid phases to disperse, whilst inside the hydrate formation envelop hydrates can form at any time. With the onset of the hydrate formation on the gas-water interface, the particles dispersed in the bulk are carried away by the liquid-phase flow. Eventually, the particles collide against the wall, stick to it because of the liquid bridge and consolidate. The continuous supply of water and hydrate particles on the surface of the deposit provided by the intermittent flow and the consequent consolidation of the particles due to the wave effect and the conversion of the water particles to hydrates increases the deposit thickness. Looking closely to a fixed region of the pipe, where is intermittently exposed to the gas phase and liquid phase because of the flow pattern or operating conditions, for example, and knowing that the flow characteristics change because of hydrate formation and deposition, the extent of the deposit increases both horizontally and vertically. Therefore, the accumulation of the hydrates occurs on the gas-liquid interface, and the surface needs to be water-wetted so that the hydrate deposition can occur.

Figure 4.19— Conceptual model of hydrate formation and accumulation in the water-continuous system as a function of time considering a slug flow pattern. The illustration reflects the impact of the slug flow pattern on the growth of the deposit: system condition before the beginning of the hydrate formation; the onset of the hydrate formation on the gas-water interface; hydrate particles stick to the wall surface because of the liquid bridge formed and consolidated; the intermittent passage of the flow causes the collision of hydrate particles which were floating in the flow and continuously expose the surface of the deposit to hydrate-forming compounds (water and gas) eventually causing the growth of the deposit.



Source: own authorship.

The conceptual model was formulated based on the rock-flow cell experiments for specific systems; see Table 4.1. The mechanism of hydrate accumulation for gas-

hydrate-water systems, described above as the wave effect, was also observed under isobaric experimental conditions; see Kakitani et al. 2021. Under actual flow conditions, this conceptual model and the time to reach a stable morphology may differ from the rock-flow cell system. A few possible reasons are:

- The hydrodynamics of the systems are different, what implies different nucleation and growth rates.
- The constant volume and number of components in the experiments described herein result in less hydrate formation and reduced driving forces for the crystallisation, such as the temperature and pressure, upon the hydrate formation. That differs from flowline operational conditions, which usually operate under a constant pressure profile and present a continuous supply of water and hydrocarbons (oil and gas), resulting in a continuous hydrate formation in the system. Moreover, the volume of the pipeline remains constant whilst the production is halted, and if hydrates start forming, a local pressure drop might occur. However, the time required for hydrate formation under static conditions is high, and the hydrate growth rate will be low.

These differences must be considered when extending the rock-flow cell analyses to flowline conditions. The phenomena observed are nevertheless expected to be qualitatively the same. The wave effect promotes, mainly, a deposition on the upper wall as long as the gas-water flow conditions are able to touch the upper wall (e.g., in the case of slug flow). The expected differences between a flowline and the rock-flow cell come from the frequency of the wave effect. That is, depending on the actual hydrodynamics (velocity, shear rate) and thermodynamics (local subcooling) in the flowline, the wave effect and all other discussed phenomena will happen either faster or slower than in the rock-flow cell. The quantification of such phenomena falls outside the scope of this study, however.

#### **4.4 Estimation of the amount hydrate formed**

To estimate the amount of hydrates formed during the experiments, it is important to know the total amount of water inside the liquid phase and present as

vapour in the gaseous phase, as well as the total amount of the gas component inside the gaseous phase and dissolved in liquid water. Those depend on the pressure and temperature conditions during the experiment. The experiments performed did not have an inline chromatograph to read the amounts of water and gas in each phase to determine the amount of hydrate formed. Therefore, the methodology proposed by Straume (2017) to estimate the experimental rate of hydrate formation is applied in this study. The method is briefly summarised in this section, and further details can be found in Appendix A — Procedure for the estimation of the Amount of Hydrate Formed and in the original study.

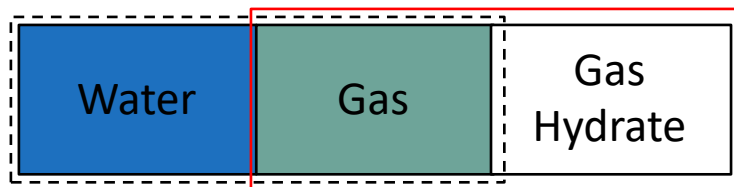
The experiments were carried out by following the isochoric methodology; that is, the difference between the initial value of the component and its value in the liquid and gaseous phases determines the amount of these components that are converted to hydrates. Therefore, the amount of hydrate can be estimated by considering the hydration number, which depends on the type of the crystalline structure formed, and the difference between the initial value of each component (water and gas) and the updated value of each element (water and gas) in the aqueous and gaseous phases under determined pressure and temperature conditions.

The amount of the components in each phase upon hydrate formation was estimated by flash calculations for each time step using the composition data from the previous time step. This approach assumes that the fluids are under equilibrium conditions at each recorded pressure and temperature points. This assumption introduces some errors which are considered minor ones because the time steps between data recordings are small (2 s), and the hydrate growth rate is considerably slow. A commercial software, Multiflash™, performed the flash calculations. The CPA (Cubic Plus Association) equation of state is used to determine the fluid phases' data. The CPA model consists of the Soave-Redlich-Kwong equation coupled with the association term based on Wertheim's theory. The calculations were carried out with the Multiflash-Excel Interface, which provides functions that can be called by a Microsoft Excel® spreadsheet.

Immediately before the onset of the hydrate formation, the rock-flow cell is a two-phase system. However, upon the beginning of hydrate formation, the system turns itself into a three-phase one: water, gas and hydrates. That considerably

increases the complexity of the estimations. To circumvent this complexity, the three-phase system is split into two simpler systems, one composed of water and gas phases and the other of gas and hydrate phases, as shown in Figure 4.20. As the volume and quantity of the components in the rock-flow cell are constant throughout the experiments, the mass balance equation can be applied to each of the two-phase systems. In this case, the volume and composition in each two-phase system studied must be adjusted to guarantee that the total composition and volume remain constant throughout the experiment.

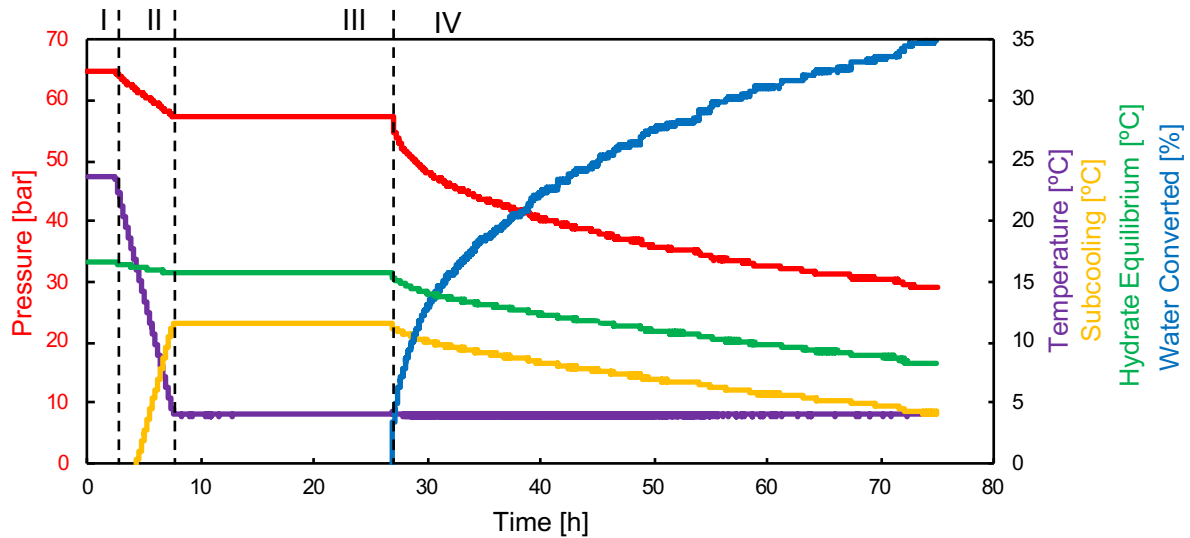
Figure 4.20— A three-phase system. The black dashed line represents the equilibrium condition for the water and gas system, and the red continuous line represents the equilibrium condition for the gas and hydrate phases.



Source: own authorship.

Figure 4.21 presents the measured and calculated parameters for an isochoric experiment of hydrate formation. Region I to IV were described in subsection 4.1: region I is the pressure and temperature condition at the beginning of the investigation, region II represents the system's cooling region, region III determines the induction time, and region IV is the hydrate formation region. The commercial software, Multiflash, calculated the hydrate equilibrium temperature (green line) at the system pressure condition (red line). Subtracting the hydrate equilibrium temperature curve from the average experimental temperature curve (purple line) yields the subcooling of the system (yellow line). Because the average experimental temperature (purple line in Figure 4.20) is considered an average of the gradient temperature inside the cell, it may introduce errors when calculating both the subcooling and the amount of hydrate formed. The percentage of water converted to hydrates is shown in the blue line. This percentage represents the amount of water converted to hydrates and was estimated through the method described above.

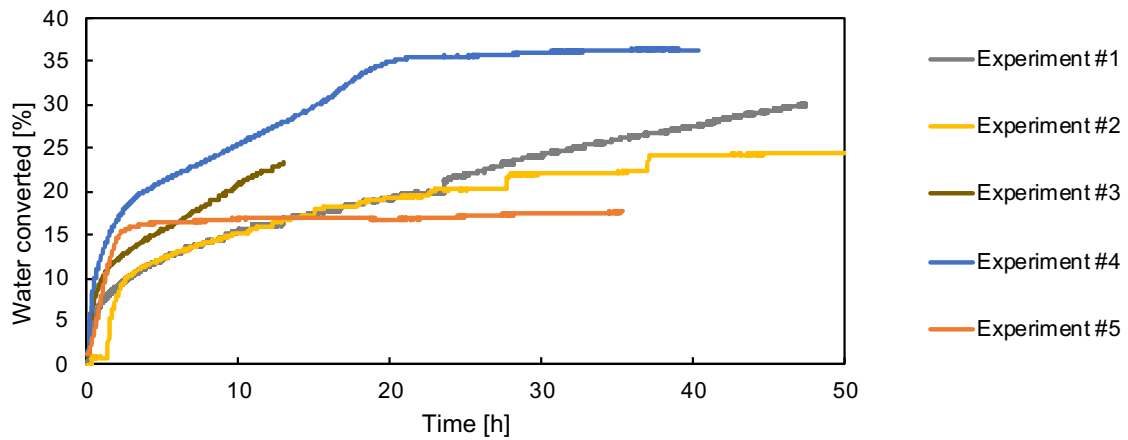
Figure 4.21— Pressure, temperature and water converted to hydrate of experiment #25 (40 %vol. LL and 11.25 rpm). The red line is the pressure of the system which drops as the temperature decreases and gas is consumed to form hydrates. The temperature of the system (purple), hydrate equilibrium temperature (green) and subcooling (yellow) — difference between purple and green lines. The blue line is the amount of water converted to hydrates during the experiment. The vertical dashed lines refer to: gas solubility in the liquid phase (region I), the system temperature decrease to the experimental temperature (region II), system conditions are inside the hydrate equilibrium curve (region III) without visible hydrate formation, the onset of the hydrate formation (region IV).



Source: own authorship.

The rate of water converted to hydrates as a function of time for gas-water systems is presented in Figure 4.22 to Figure 4.27. The rate of hydrate formation is higher at the beginning of the formation, i.e., from one to five hours and slows down later, showing an asymptotic behaviour. Experiment #4 (30 %vol. LL and 18.75 rpm) in Figure 4.22 showed the highest rate of hydrate formation among the experiments with 30% vol. of LL, and the footage showed that the blockage of the cross-section area of the cell took longer time to occur when compared to the other experiments at the same liquid loading. The transportable hydrate slurry formed at the beginning of experiment #4 might have contributed to the highest water conversion to hydrates. The subcooling at the beginning of the hydrate formation in experiments #1 (30 %vol. LL and 11.25 rpm) and #3 (30 %vol. LL and 18.75 rpm) was similar, but it was observed a higher rate of conversion of experiment #3 compared to experiment #1. This difference may come from the higher oscillation rate of the rock-flow cell, which increases the shear rate of the system, thus reducing the mass transfer resistances.

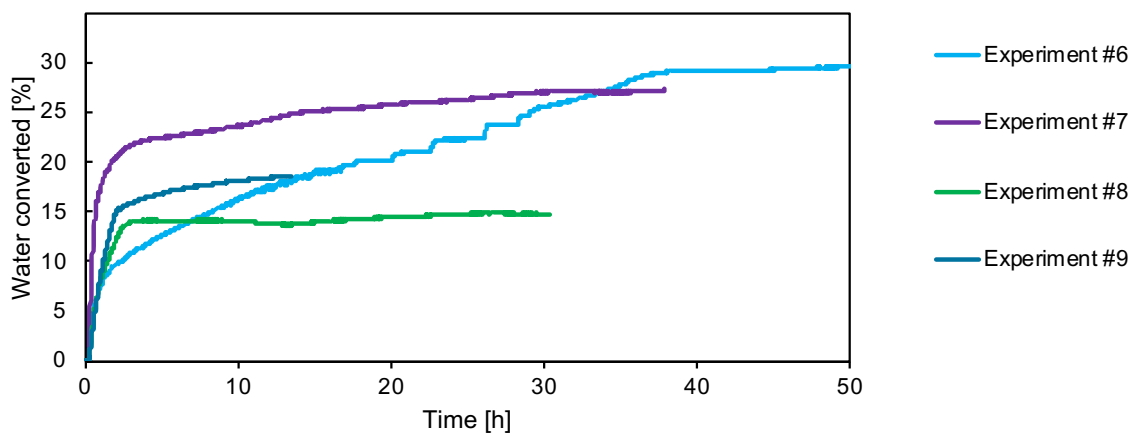
Figure 4.22— Water converted to hydrates for 30 %vol. LL of water and gas methane as the gas phase at different experimental temperatures and 18.75 rpm (except experiment #1, which was performed at 11.25 rpm).



Source: own authorship.

Figure 4.23 presents the water-converted data for 40 %vol. of water and gas methane systems. The difference in the subcooling condition at the beginning of the hydrate formation led to a variation in the initial rate of hydrate formation of experiments #6 and #9 in Figure 4.23, which were carried out under the same experimental conditions. Moreover, the differences in the morphology of the final hydrate accumulation of these experiments were linked to the difference in subcooling at the beginning of the hydrate formation. Therefore, hydrate formation is highly influenced by the driving force (subcooling) during the beginning of the hydrate formation.

Figure 4.23— Water converted to hydrates for 40 %vol. LL of water and gas methane as the gas phase at different experimental temperatures.



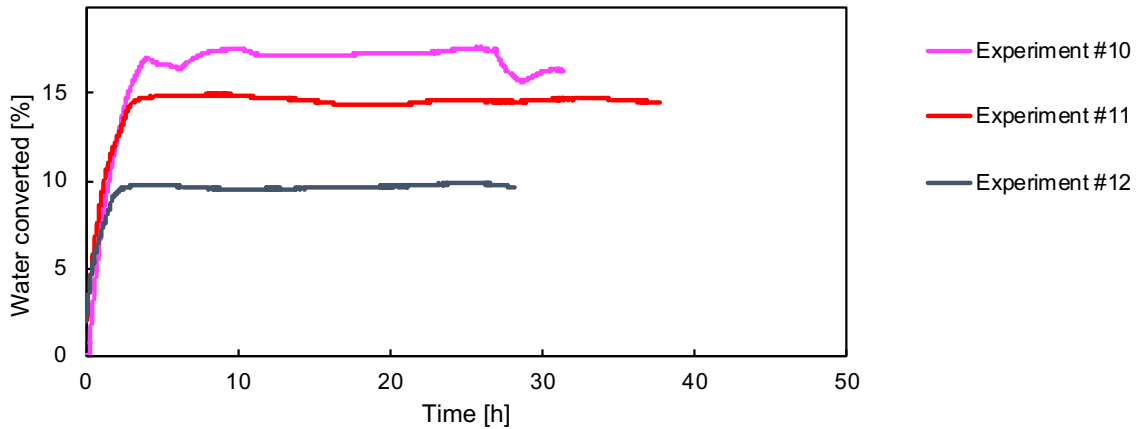
Source: own authorship.



Experiments #6 and #7 presented the highest subcooling conditions at the beginning of the hydrate formation, 6.6°C and 4.7°C, respectively, among the 40 %vol. water and gas methane experiments. As a consequence of the higher driving force, the pipe was blocked during the first hour after the onset of the hydrate formation, and both experiments presented higher water conversion to hydrates, being experiment #6 (40 %vol. LL and 18.75 rpm) the one with a higher amount of hydrates formed as its experimental temperature is higher than that of the experiment #7 (40 %vol. LL and 18.75 rpm).

Experiments #10, #11 and #12 were performed at similar liquid loadings and oscillation rates (50 %vol. LL and 18.75 rpm); see Figure 4.24. The onset of the hydrate formation occurred for a similar subcooling of approximately 2.5°C. As a consequence, the rate of hydrate formation in the first two hours was very close, thus emphasising the importance of the driving force at the onset of the hydrate formation in the case of an isochoric procedure. The lower experimental temperature conditions promoted the formation of transportable hydrate slurries (experiments #11 and #12). In Experiment #10, the unstable condition due to sloughing events led to a local blockage of the cross-section area of the cell. The final morphology of the hydrate formation may have impacted mass and heat transfer inside the cell, and the variation of the experimental temperature conditions among the experiments restricted the water conversion to hydrates. Experiment #10 is the one with highest hydrate formation, as Figure 4.24 shows. The sloughing events may have contributed to the highest water conversion to hydrates. The detachment of the hydrate chunks causes an increase in the pressure curve because of the release into the system of the gas trapped inside the hydrate deposit structure (increasing the system-driving force) whilst increases the gas-water contact area, promoting the formation of hydrates.

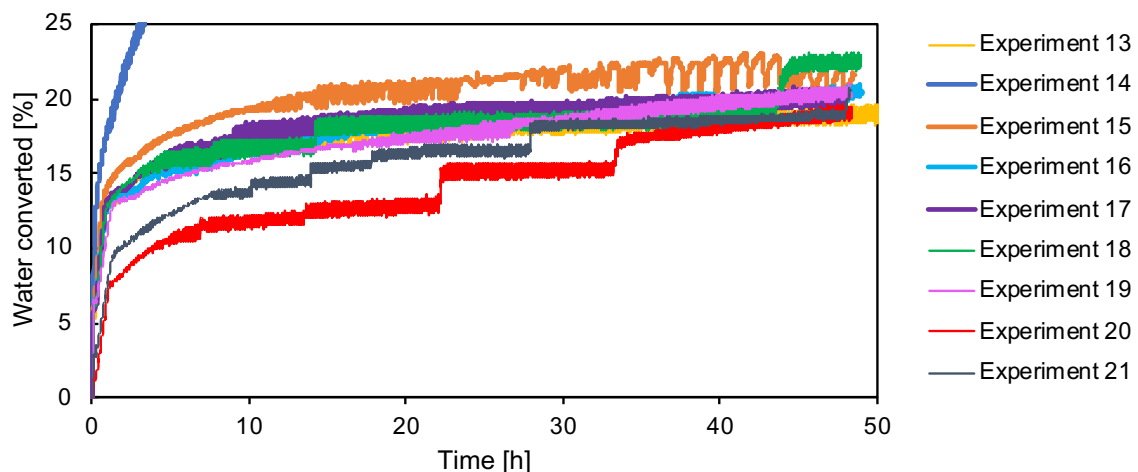
Figure 4.24— Water converted to hydrates for 50 %vol. LL of water and gas methane as the gas phase at different experimental temperatures.



Source: own authorship.

The beginning of the hydrate formation for the 20 %vol. of water and methane/ethane gas mixture system occurred for a subcooling of approximately 2.2°C in all experiments, Figure 4.25, except experiment #14 (20 %vol. LL and 18.75 rpm), where the water converted to hydrates remained around 20% regardless of the oscillation rate and the temperature of the system. The highest subcooling at the onset of the formation in this experiment, of approximately 10.7°C, contributes to the highest rate of hydrate formation compared to the other experiments

Figure 4.25— Water converted to hydrates for 20 %vol. of water and methane/ethane gas mixture system under different temperatures and oscillation rate conditions.

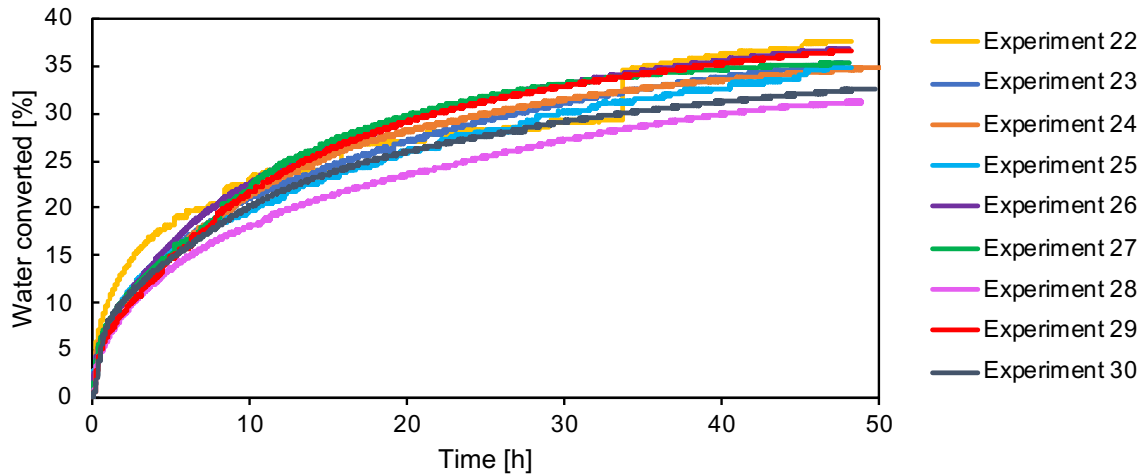


Source: own authorship.

For the 40 %vol. of water and methane/ethane gas mixture system, the estimated amount of hydrate formed remained within the range of 31% to 38%, and

the formation rate at the beginning varied little amongst the experiments, as shown in Figure 4.26.

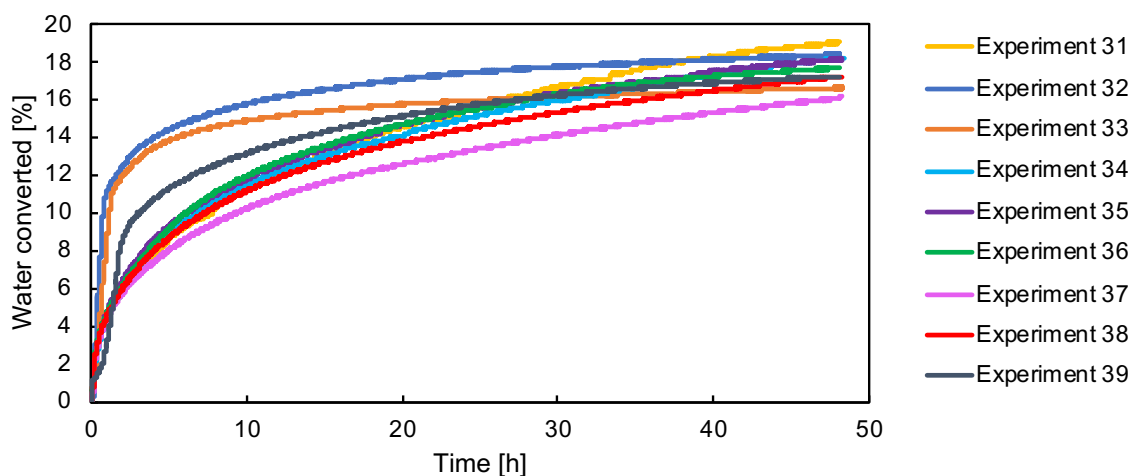
Figure 4.26— Water converted to hydrates for 40 %vol. of water and methane/ethane gas mixture systems at different temperatures and oscillation rate conditions.



Source: own authorship.

The results for the water converted to hydrates for the 60 %vol. of water and methane/ethane gas mixture systems are shown in Figure 4.27. In those experiments, the higher formation rate occurred for the lowest subcooling conditions, as observed in experiments #32, #33 and #39. In these experiments, a hydrate slurry formation was observed even after 15 min of the beginning of the hydrate formation and the thicker hydrate deposits took longer to form. The lowest subcooling influences the heat transfer rate of the system taking longer to form the thicker hydrate deposit on the upper wall. On the other hand, the presence of the slurry influences the mass transfer rate of the system leading to a higher hydrate formation rate. It demonstrates the influence of the earlier hydrate accumulation on the rate of hydrate formation. At the end of these experiments, no free water film was observed in the footage.

Figure 4.27— Water converted to hydrates for 60 %vol. of water and methane/ethane gas mixture systems under different temperatures and oscillation rate conditions.



Source: own authorship.

Higher liquid loading means higher turbulence and shearing levels caused by the flow, reducing the hydrate formation rate. In the water and gas mixture system, the formation of a thicker hydrate deposit may have impaired the mass and heat transfers, decreasing the formation rate. In the case of water and methane gas experiments, the decrease in the water conversion for the 50 %vol. of LL might be due to the combination of low subcooling with the formation of a transportable hydrate slurry.

The morphology of hydrate accumulation influences the growth rate of the hydrate formation as the mass and heat transfer are impacted by it. Overall, the water conversion to hydrates did not exceed 30% in most experiments regardless of the gas phase (pure methane or methane/ethane gas mixture). The experiments with higher liquid loading (> 50% vol LL) have the lowest water conversion rate.

#### 4.5 Static experimental conditions

Most of the gas-hydrate-water experiments performed under dynamic conditions presented hydrate wall deposition in the first hour after the beginning of hydrate formation. Grasso et al. (2014) described three mechanisms responsible for water migration to the upper surface of the deposit: (i) direct liquid contact, (ii) liquid capillarity, and (iii) water evaporation with further condensation on the wall (cold surface).

Two experiments with 60 %vol. of LL were carried out under static conditions. In these experiments, a temperature gradient was forced inside the cell with the bottom wall temperature at about 10°C and the upper wall temperature at 4°C. In one experiment, the rock-flow cell was stopped horizontally. In contrast, in the second experiment, the cell was stopped at an angle of 11° as an alternative to decrease the interfacial area and approach the gas-liquid interface with the upper wall. The objective of these experiments is to understand the central mechanisms leading to hydrate deposit formation under dynamic conditions.

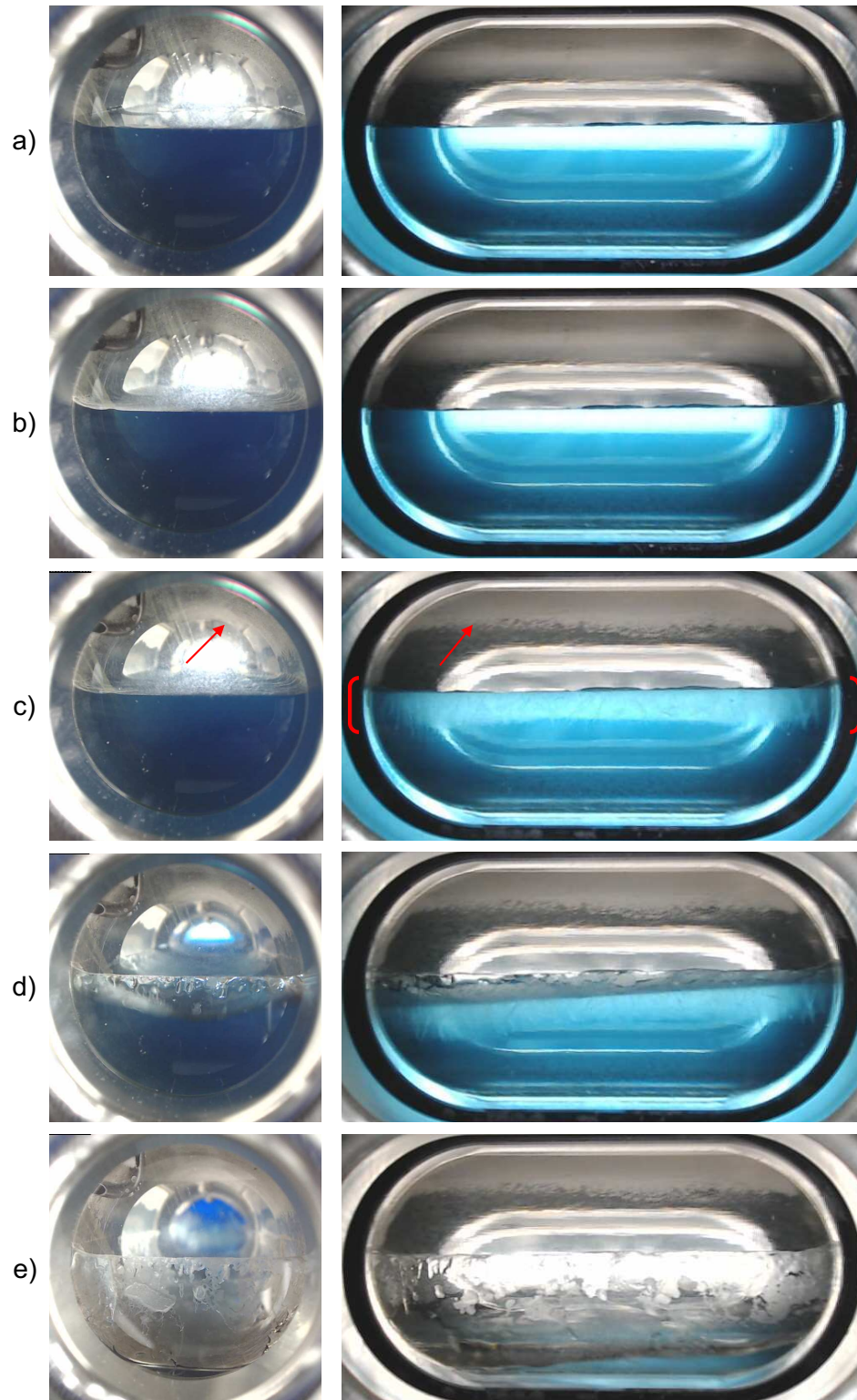
Through the analysis of the experiments performed under static conditions, the hydrate formation occurred close to the gas-liquid interface and apparently without hydrate formation on the top of the wall. In one of the experiments, during the solubilisation process, the upper wall was wetted by the water phase, resulting in the formation of a thin deposit layer, which seems not to have increased throughout the test. In the other experiment, in which care was taken not to allow the water phase to reach the top area, the formation of a hydrate deposit in the upper region was not observed. However, when the rock-flow cell movement began at the end of the experiment, the hydrate particles, which were accumulated in the bulk, started to adhere to the wall, forming hydrate deposits. Let us suppose that the hydrate deposits result primarily from water permeation on the wall (ii) or water evaporation followed by water condensation on the wall (iii). In that case, a thicker hydrate deposit should have been observed in the static systems.

Therefore, it is reasonable to say that mechanisms such as water evaporation/condensation (diffusion) and liquid capillarity (water permeation on the wall) present little influence on hydrate deposition. Consequently, these mechanisms can be neglected for static and dynamic conditions alike.

Figure 4.28 shows the process of the hydrate formation and accumulation in window 4 and window 1 under static horizontal conditions. The photos were taken a) before the onset of the hydrate formation, b) three minutes after such onset, showing the formation on the gas-liquid interface, and c) 13 hours after the aforementioned. The red bracket shows the height of the hydrate layer formed in the bulk, and the arrows show the thin hydrate layer on the upper wall. The liquid phase has previously wetted the upper region of the rock-flow cell. Therefore, the thin hydrate deposit layer

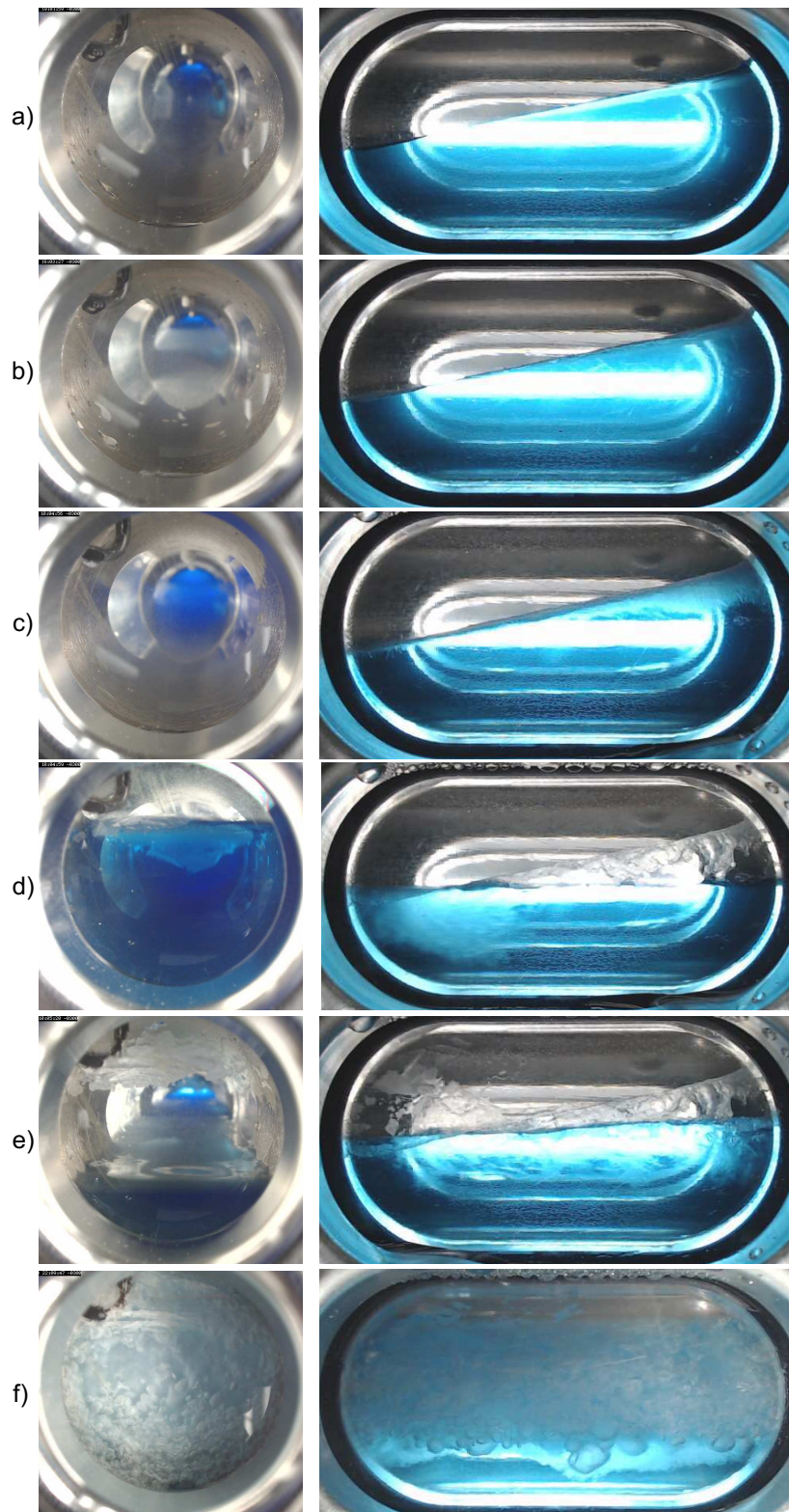
at the top does not present a hazardous condition if no extra water is added. Afterwards, the rock-flow cell was set to oscillate at 2 rpm, thus evidencing the formation of hydrates on the gas-liquid interface d), and the flow promotes the collision of the particles in the bulk against the wall where they can consolidate, leading to the deposition of hydrate into the wall. Under dynamic conditions, the wave effect can lead to the formation of a thicker hydrate deposit. Figure 4.29 shows the process of the hydrate formation and accumulation under static inclined conditions: a) gas-liquid interface before the hydrate formation onset; b) the beginning of the hydrate formation on the gas-liquid interface; c) a layer of hydrates is observed in the bulk and a thin hydrate layer on the upper wall (window 4) after 15 hours; d) shortly after the start of the rotation of the rock-flow cell at 2 rpm; e) particles consolidated on the wall; f) end of the experiment 12 hours after.

Figure 4.28— Photos showing the process of hydrate formation and accumulation under static conditions for 60 %vol. of LL and upper wall temperature at around 4oC and bottom wall temperature at about 10oC: a) before the onset of the hydrate formation; b) the onset of the hydrate formation on the gas-liquid interface; c) 13 hours after the onset of the hydrate formation, a layer of hydrates is observed in the bulk (red bracket) and a thin hydrate layer on the upper wall (red arrow); d) the oscillation of the rock-flow cell begins, showing the consolidation of hydrates on the wall; e) the contraction of the flow, due to the motion, drags particles that deposit on the wall. The photos are from windows 4 and 2.



Source: own authorship.

Figure 4.29— The photos show the hydrate formation and accumulation process when the rock-flow cell stops at 11o. a) before the onset of the hydrate formation; b) the onset of the hydrate formation on the gas-liquid interface; c) 15 hours after the onset of the hydrate formation, a layer of hydrates is observed in the bulk and a thin hydrate layer forms on the upper wall (window 4); d) shortly after the start of the rotation of the rock-flow cell at 2 rpm; e) the flow carries the particles that shall consolidate on the wall; f) end of the experiment twelve hours after. The photos are from windows 4 and 2.



Source: own authorship.



#### 4.6 Flow risk analysis

The experiments described herein brought new insights into the mechanism involved in the process of hydrate formation and accumulation in gas-water systems. They highlighted that the presence of a water-free phase may cause pipe blockage when inside the hydrate formation zone, since the wave effect promotes hydrate deposition on the wall. Visual observations can be biased as they depend on subjective interpretations. In addition, the range of experimental apparatuses presented in the literature to study hydrate formation and accumulation in different systems makes the analysis of potential risk conditions harder. Therefore, a systematic method for assessing the process of hydrate accumulation regardless of the limitations of the experimental apparatus and for identifying the conditions that threaten the flow assurance is important in the development of risk management strategies assuring continuous, safe, and cost-effective transport of hydrocarbons throughout all stages of oil & gas production.

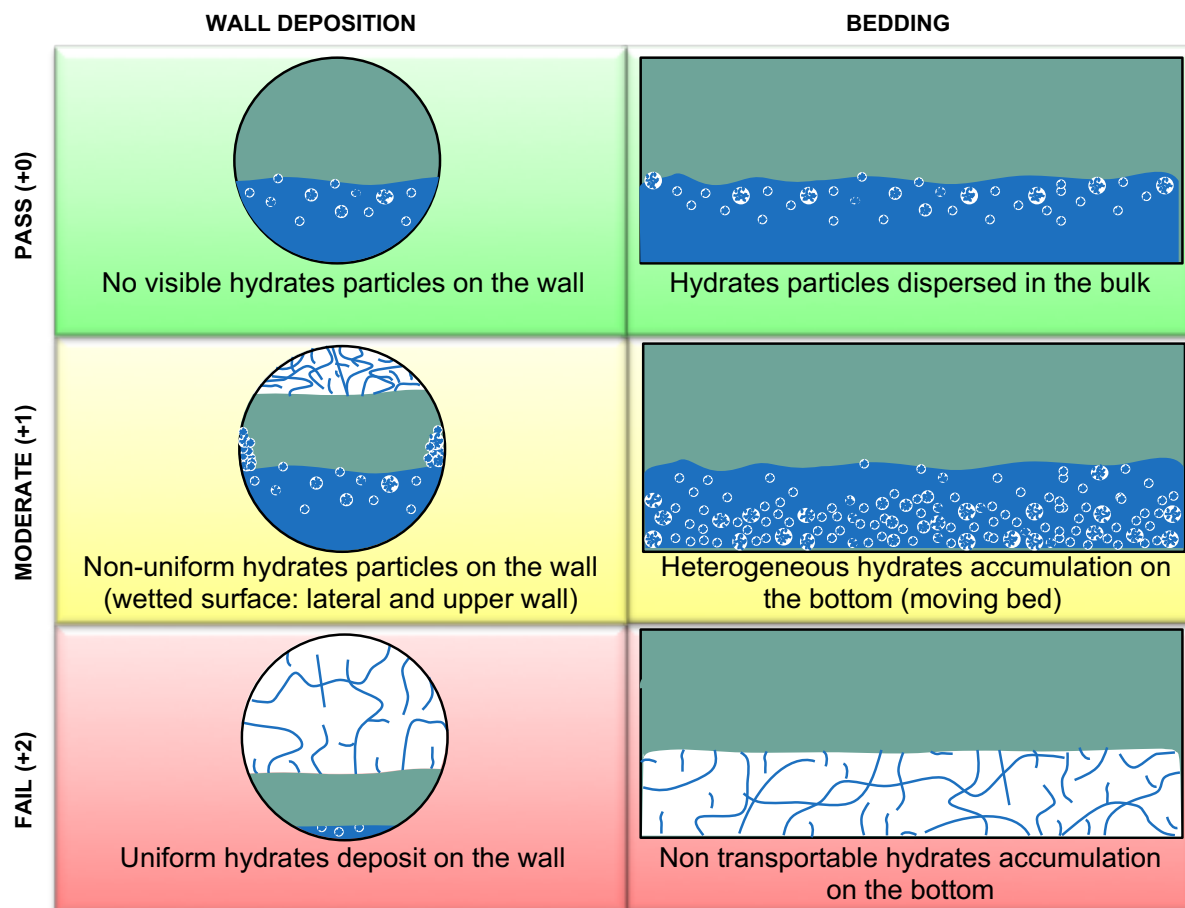
Melchuna et al. (2020) developed a flow risk index that evaluates the risk of developing a pipeline plug for oil-gas-hydrate-water systems. The analysis is based on three categories (aggregation, wall deposition and bedding) which lead to pipeline plugging formation. The absence of visible, solid hydrate particles with varying sizes (hydrates chunks) in the gas-hydrate-water systems required some adaptations to better adjust to the flow risk index developed by Melchuna et al. (2020). The aggregation mechanism, as described by the authors, does not occur for gas-water systems because of the absence of a second fluid (oil for example) to form the liquid bridge between the solids particle that holds the particles attached, forming an agglomerate (hydrate chunks). Therefore, the failure condition described for the aggregation mechanism does not occur in this kind of system. Their methodology was used as the basis for the flow risk analysis for the gas-hydrate-water systems. Instead of three, two categories (wall deposition and bedding) were outlined for analysing the flow risk. The adaptations in the flow risk index methodology changed the highest risk index from 12 for oil-gas-hydrate-water systems to 8 for gas-hydrate-water systems. Despite the lower maximum flow risk index for the gas-hydrate-water systems, a more hazardous conditions were observed in these systems (with some experiments

presenting a total blockage of the pipe cross-section area) when compared to Melchuna et al. (2020) footage for oil-dominant experiments.

Because of the evolution of hydrate particle-particle interactions throughout the experiment, the flow risk analyses were conducted in two different stages of the experiment. The footage was analysed 5 minutes after the hydrate formation onset, because of the fast water conversion to hydrates at the beginning of the hydrate formation, and at the end of the experiment. Even though the morphology is well defined after 1 hour from the beginning of the hydrate formation for almost all experiments, the analysis of the final stage was chosen because of the sloughing and annealing events presented in some experiments, as discussed above.

Figure 4.30 summarises the classification of the mechanisms of hydrate accumulation in gas-hydrate-water systems with the aim of analysing the flow risk. The risk assessment is achieved by assigning the system condition (0-pass, 1-moderate, 2-fault condition) for each of the mechanisms observed (wall deposition and bedding) under two different conditions: 5 minutes after the beginning of the hydrate formation and at the end of the experiment. The total risk is determined by adding each value. The maximum flow risk index, eight (8), corresponds to the highest risk of production interruption, whereas the zero (0) index represents the lowest risk. The scale of colours (red, green and yellow) was employed to facilitate the visual assessment of the flow risk: green (pass, +0) represents a risk-free condition; yellow (moderate, +1) indicates a potential threat, being therefore considered as a mixed condition; and red (fail, +2) a high-risk condition. The lateral view was neglected in this analysis because of the edge effect that masks the actual condition of the cross-section of the pipe.

Figure 4.30— Classifications of wall deposition and bedding mechanism for flow risk analysis of gas-hydrate-water systems. Blue represents the water phase; green is the gas phase; white is the hydrate deposits or particles. The background colours (green, yellow and red) were used to facilitate risk identification. The circle shape represents the view of the cross-section area, and the rectangular shape represents the length of the cell.



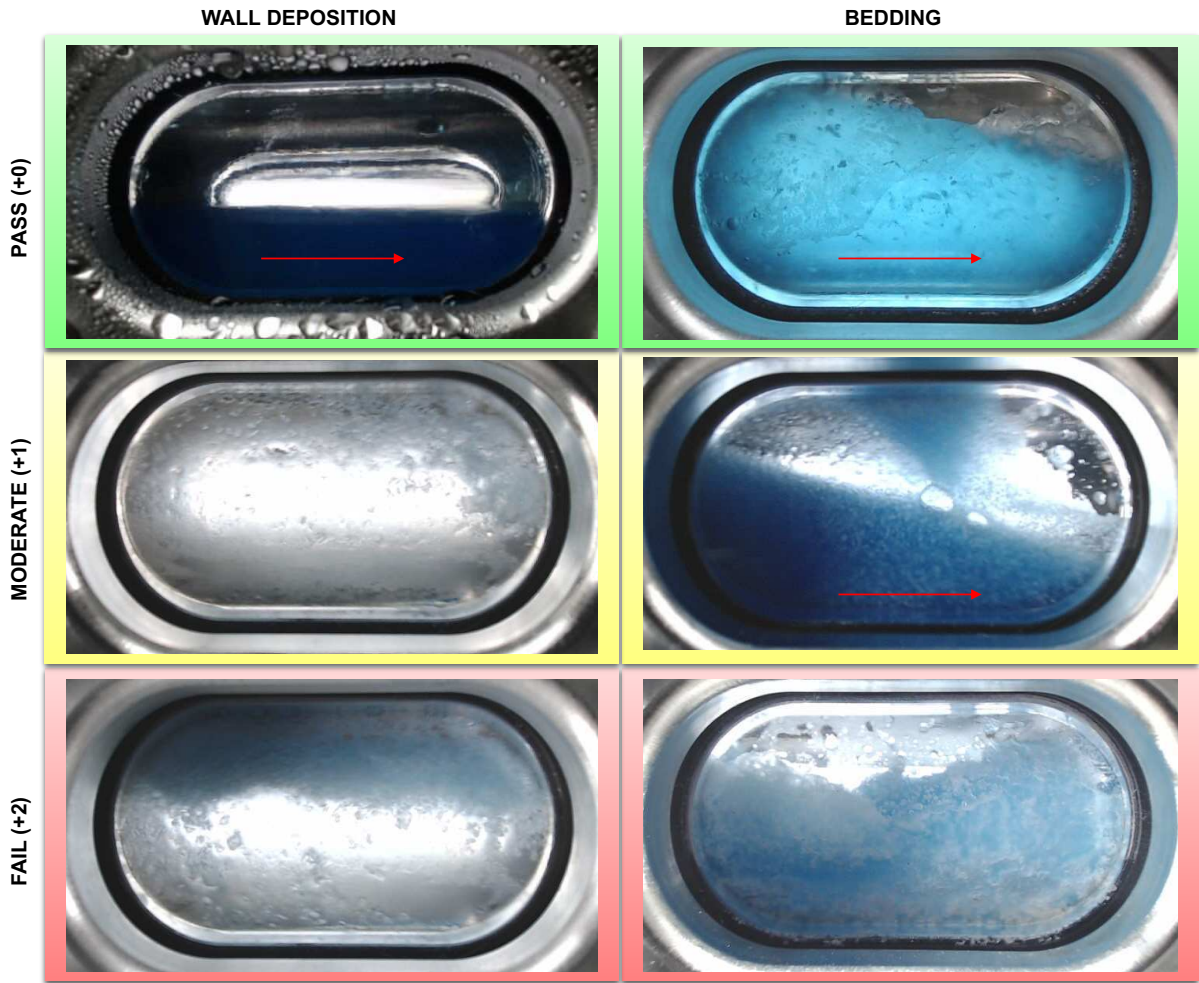
Source: adapted from Melchuna et al. (2020).

The mechanism of hydrate deposition on the wall is described as solid particles adhering to the wall, because of the wave effect, followed by the growth of the hydrate deposit. The hydrate deposits can occur at different positions of the cell following a non-uniform distribution behaviour. The hydrodynamics of the system before the beginning of the hydrate formation and multiphase flow conditions after the hydrate formation indicate where the hydrate deposits might occur probably on a wall surface constantly wetted by the aqueous phase and in contact with the gas phase as described herein. Therefore, the risk analysis criterion for the deposition mechanism was defined as a pass condition (+0) for hydrate particles not adhering to the wall; a moderate condition (+1) if the hydrate particles adhere to the wall forming a thin solid layer or a non-uniform deposit with scattered distribution; and a fault condition (+2) if a

uniform distribution of a hydrate deposit or a thicker hydrate deposit is observed in more than one position of the cell.

The bedding mechanism is defined as the interaction between the hydrate particles and the flow. The criterion used for risk analysis was described as a pass condition (+0) for the homogeneous dispersion of hydrate particles (the blue ink of the water phase is still predominant); moderate condition (+1) for heterogeneous dispersion of hydrate particles (viscous flow due to a large amount of hydrate particles in the bulk) or when a thin hydrate layer is observed at the bottom of the cell; and a fault condition (+2) when hydrate particles settle at the bottom of the cell, resulting in a non-transportable condition. Figure 4.31 illustrates the classification of the flow risk index through the photos taken during the experiments.

Figure 4.31— Photos of the classification for wall deposition and bedding mechanisms according to flow risk criterion for gas-hydrate-water systems. The red arrow indicates that the bulk phase is in constant motion.



Source: own authorship.

In this context, the risk flow index according to the risk methodology presented above are presented in Table 4.2 for water and methane systems and Table 4.3 for water and methane/ethane gas mixture systems.

Table 4.2— Flow risk analysis for water and methane systems. Grade 0 represents a pass condition, grade 1 is a moderate condition, and grade 2 is a fault condition. The maximum flow risk index is 8 indicating a high risk of flow disruption. The first column represents the analysis after 5 minutes of the beginning of the hydrate formation and the other at the end of the experiment.

Exp.	Flow Risk	Wall Deposition		Bedding	
		5 min	Final	5 min	Final
1	8	2	2	2	2
2	8	2	2	2	2
3	8	2	2	2	2

Table 4.2— Flow risk analysis for water and methane systems. Grade 0 represents a pass condition, grade 1 is a moderate condition, and grade 2 is a fault condition. The maximum flow risk index is 8 indicating a high risk of flow disruption. The first column represents the analysis after 5 minutes of the beginning of the hydrate formation and the other at the end of the experiment.

Exp.	Flow Risk	Wall Deposition		Bedding	
		5 min	Final	5 min	Final
4	7	2	2	1	2
5	4	1	2	0	1
6	8	2	2	2	2
7	5	1	2	1	1
8	4	1	2	1	0
9	4	1	2	1	0
10	4	1	2	1	0
11	3	1	1	1	0
12	3	1	1	1	0

Source: own authorship.

Table 4.3— Flow risk analysis for water and methane/ethane gas mixture systems. Grade 0 represents a pass condition, grade 1 is a moderate condition, and grade 2 is a fault condition. The maximum flow risk index is 8 indicating a high risk of flow disruption. The first column represents the analysis after 5 minutes of the beginning of the hydrate formation and the other at the end of the experiment.

Exp.	Flow Risk	Wall Deposition		Bedding	
		5 min	Final	5 min	Final
13	5	1	2	1	1
14	8	2	2	2	2
15	5	1	2	1	1
16	5	1	1	1	2
17	5	1	1	1	2
18	5	1	1	1	2
19	4	1	1	0	2
20	4	1	1	0	2
21	4	1	1	0	2
22	8	2	2	2	2
23	8	2	2	2	2
24	7	2	2	2	1
25	8	2	2	2	2
26	8	2	2	2	2
27	6	2	2	1	1
28	7	2	2	1	2
29	6	2	2	1	1
30	6	2	2	1	1

Table 4.3— Flow risk analysis for water and methane/ethane gas mixture systems. Grade 0 represents a pass condition, grade 1 is a moderate condition, and grade 2 is a fault condition. The maximum flow risk index is 8 indicating a high risk of flow disruption. The first column represents the analysis after 5 minutes of the beginning of the hydrate formation and the other at the end of the experiment.

Exp.	Flow Risk	Wall Deposition		Bedding	
		5 min	Final	5 min	Final
31	4	2	2	0	0
32	5	1	2	1	1
33	5	1	2	1	1
34	4	2	2	0	0
35	4	2	2	0	0
36	4	2	2	0	0
37	4	2	2	0	0
38	4	2	2	0	0
39	6	1	2	1	2

Source: own authorship.

Therefore, according to the criteria applied, the flow risk with index 3 (three) represents the condition of a solid transportable hydrate slurry. It was only observed in the water and methane gas systems (sl hydrate structure). Under these conditions, the system has a low risk of forming a hydrate plug. A production disruption will be observed for a flow risk index equal to or higher than 4 (four). A thicker hydrate deposit was formed in experiments #31 to #39, albeit not presenting a high risk. In these experiments, the blockage of the pipeline was not observed, but a noticeable fraction of the cross-section was compromised because of the upper wall solid deposit.

Given that, the hydrate formation in the gas-water system presents a high risk of production impairment due to the bedding and wall deposition formation, which reduces the cross-section area, and in the worst-case scenario, production disruption caused by the formation of a hydrate plug.

#### 4.7 Final considerations of the chapter

This chapter showed the experimental results obtained for gas-hydrate-water systems. The footage taken during the experiments allowed gathering visual information about the mechanisms involved in the hydrate formation and accumulation processes, such as wall deposition, sloughing, and plug formation. The morphology of

the system, as determined from the photos, and the measured data increased the knowledge towards an enhanced understanding about the mechanisms that play a role in hydrate formation and accumulation inside multiphase flow systems. The main conclusions from this chapter are:

- Hydrate deposition occurred independently of the existence of a gradient of temperature between the upper and bottom wall of the rock-flow cell. This was not expected, as it was believed that the nucleation of hydrates and their deposition on the wall was due to the lower wall temperature when compared to the bulk.
- The consolidation of hydrates on the wall and the consequent growth of the deposit come from that what is called the wave effect and happens mainly because of the liquid bridging of the particles coming from the wavy hydrodynamic motion of the gas-water interface. Such a mechanism is so strong and fast that thick hydrate deposits were observed on the upper wall of the rock-flow cell only a few minutes after the onset of the hydrate formation, enduring gravity. The hydrates deposits on the wall have already been observed in the literature. They are usually believed to come from a lower wall temperature which prompts the nucleation of the hydrate seeds directly on the wall. The newly proposed mechanism (the wave effect) seems more reasonable on the grounds of the experimental observations shown in this chapter.
- The wave effect can be described in an intermittent gas/liquid flow as the hydrate particles dispersed in the liquid eventually colliding against the wall due to the flow conditions. The impact of the fluid (water with hydrate particles) to the wall when in contact with the gas phase causes the formation of liquid bridges. The liquid bridge causes a binding force that keeps the hydrate particle adhered to the wall. The intermittent flow conditions favour the crystallisation of the liquid bridge on the wall during the gas flow, depending on the contact time and subcooling. The crystallisation attaches the hydrate particles to the wall, forming the first layer of the hydrate deposit. When the liquid flow arrives, the second wave, for example, due to the intermittent gas/liquid flow, moistens the



surface of the hydrate deposit. It renews the surface with bulk hydrate particles, increasing the thickness of the hydrate deposit. But, depending on the flow energy, it also provides power to detach the hydrate deposit or wash the hydrate particles in the surface of the hydrate deposit away, if not properly consolidated.

- Hydrate sloughing events were observed in methane gas-hydrate-water systems. The low subcooling condition of the system at the beginning of the hydrate formation might have increased the unconverted water inside the hydrate deposit structure, thus reducing its mechanical stability and promoting sloughing events. In contrast, the high subcooling conditions imposed by the water-methane/ethane gas system reduce the unconverted water inside the hydrate structure, thus enabling faster water conversion to hydrates and contributing to the hydrate deposit stability.
- A conceptual hydrate formation and accumulation model in water-continuous systems was proposed based on the experiments; see Figure 4.19. When the system is inside the hydrate formation envelope and depending on the flow and fluid conditions, hydrates can form at any time. In a gas/liquid intermittent flow, the upper region of the pipeline is exposed either by the liquid phase or gas phase. With the beginning of the hydrate formation on the gas-water interface, the particles dispersed in the bulk are carried by the liquid-phase flow to the upper region. Eventually, the particles collide against the wall, stick to it because of the liquid bridge and consolidate during the gas phase exposure, as the flow energy is low compared to the fluid flow energy. The continuous supply of hydrate-forming compounds on the surface of the deposit due to the intermittent flow gradually increases the deposit thickness (vertical direction of the deposit). However, the flow characteristics change due to the hydrate formation and deposition. Because of the upward and intermittent flow conditions, the deposit thickness also increases in the direction of the flow. This conceptual model and the time to reach a stable morphology under actual flow conditions may differ from the rock-flow

cell system. The phenomena observed are nevertheless expected to be qualitatively the same.

- The water conversion, and consequently the hydrate formation, depends on the hydrate accumulation morphology because this interferes with the mass and heat transfer.
- The rate of hydrate formation is seemingly influenced by the initial subcooling (driving force), liquid loading conditions (flow shearing) and the morphology of the hydrate accumulation. It was observed that the rate of hydrate formation was reduced when the liquid loading in the gas-hydrate-water experiments was increased.
- The two experiments performed under static conditions — to investigate the influence of the water evaporation followed by wall condensation, capillary force and flow condition on the formation of hydrate deposits — indicates that water evaporation/condensation (diffusion) and capillarity force (water permeation on the wall) present little influence on hydrate deposition.
- The risk estimation was based on the visual observations; the absence of agglomerations in gas-hydrate-water systems changed the criterion for the flow risk index developed by Melchuna et al. (2020). A production disruption will be observed for a flow risk index equal to or higher than 4 (four). In contrast, a low-risk index of 3 (three) represents the condition for the transportability of solids, which was only observed in the water and methane gas systems.

## 5. RESULTS AND DISCUSSION OF WATER, MINERAL OIL AND SYNTHETIC GAS SYSTEMS

A challenge when studying the process of hydrate accumulation under multiphase flow conditions is to find the phenomena involved in the accumulation process regardless of any specific characteristic that originates only, for example, from the limitation of the experimental apparatus, experimental conditions, fluids in the system, or flow conditions used. Through the knowledge of the phenomena involved, it is possible to determine the hydrate accumulation process in any system by just knowing some flow parameters and thereby finding the right strategy for hydrate management.

To investigate the interdependence of the multiphase flow conditions and the process of hydrate accumulation, experiments were performed in a rock-flow cell with visualisation capabilities. The system studied was composed of freshwater as the aqueous phase, light mineral oil as the oil phase, and a gas mixture composed of 74.7 mol% methane / 25.3 mol% ethane as the gas phase. In this study, pure methane gas was not used because of the low driven force (subcooling) for the hydrate formation. The hydrodynamics of the system was assessed by investigating the influence of the water content, the liquid loading, the subcooling and the temperature gradient inside the pipeline under different flow rate conditions. Depending on the experimental conditions of the system, a shear-stabilised dispersion of the liquid phase was formed between the water and oil phases before the beginning of hydrate formation. No additives were added to these systems.

The hydrodynamic of the system before the onset of the hydrate formation, the dispersion or not of the shear-stabilised dispersion after the beginning of hydrate formation, and the key mechanism leading to hydrate wall deposition are some of the findings from the image processing, which will be described in the following subsections.

## 5.1 Hydrate formation in fresh water- mineral oil- gas systems

Several experiments were carried out by varying: the liquid loading from 40 to 80 %vol., the water content from 20 to 70 %vol., the rock-flow cell oscillation from 6 to 18.75 rpm to simulate different flow conditions and the wall temperature from 4 to 10°C to study the influence of the wall temperature on hydrate upper wall deposition. These decisions were based on the experimental conditions necessary to form a shear-stabilised dispersion and on the willingness to understand the influence of the hydrodynamics and the wall temperature on the process of hydrate wall deposition as observed in the experiments with 100% of water content (without oil phase). Despite the attempts made to simulate different flows in pipelines, the predominant flow pattern in all experiments before the onset of the hydrate formation was stratified wavy flow (SW). One should remember that one limitation of employing the rock-flow cell apparatus vis-a-vis actual pipelines comes from the fluid collision with the lateral walls at the ends of the cell, forming a recirculation region. These experiments were performed without the water memory effect as the gas mixture presents a higher equilibrium temperature, giving a higher subcooling range when compared to pure methane gas. The high driving force (higher subcooling) presumes fast nucleation kinetics.

The temperature and pressure profile of the oil-gas-hydrate-water system follows the same procedure as described in section 4.1. The average experimental temperature is estimated based on Eq.4.1 as a consequence of the experimental methodology employed, which in some cases imposed a gradient of temperature inside the rock-flow cell — the top wall of the cell is set at a lower temperature than the bottom wall temperature.

The experimental conditions at the beginning of the hydrate formation for the thirty-two (32) experiments performed in oil-gas-water systems are shown in Table 5.1, with the respective flow regime before the onset of the hydrate formation, the approximated time elapsed within hydrate formation region until the beginning of the hydrate formation onset ( $t_{\text{hydrate onset}}$ ), the time elapsed from the beginning of the hydrate formation to the beginning of the hydrate dissociation process, the water converted to hydrates at the end of the experiment— which indicates the amount of hydrate formed —, and the risk of flow disruption under the given experimental conditions.

Table 5.1— Experimental data summary for fresh water, mineral oil, gas mixture and gas hydrate systems with the respective measured data at the onset of the hydrate formation, estimated amount of water converted to hydrate and flow risk index.

Exp.	Gas phase	Hydrate structure	LL [%vol.]	WC [%vol.]	$\omega^a$ [rpm]	Flow regime <sup>b</sup>	PONSET [bar]	T <sub>average</sub> [°C]	Subcooling onset [°C]	t <sub>hydrate onset</sub> [h]	$\Delta t$ [h]	Water Converted [%]	Final Morphology <sup>c</sup>	Flow risk <sup>d</sup>
40	CH <sub>4</sub> +C <sub>2</sub> H <sub>6</sub>	sII	40	20	06	I	62.65	5.13	11.23	4.10	48.13	24.27	I	7
41	CH <sub>4</sub> +C <sub>2</sub> H <sub>6</sub>	sII	40	20	06	I	63.80	7.50	8.99	8.82	47.98	10.36	I	8
42	CH <sub>4</sub> +C <sub>2</sub> H <sub>6</sub>	sII	40	20	11.25	I	62.63	5.01	11.35	6.09	48	61.65	I / IV <sup>e</sup>	9
43	CH <sub>4</sub> +C <sub>2</sub> H <sub>6</sub>	sII	40	20	11.25	I	64.01	7.90	8.62	2.77	48	10.13	I	8
44	CH <sub>4</sub> +C <sub>2</sub> H <sub>6</sub>	sII	40	20	18.75	I	62.67	5.00	11.36	10.63	48	65.97	I / IV <sup>e</sup>	9
45	CH <sub>4</sub> +C <sub>2</sub> H <sub>6</sub>	sII	40	20	18.75	I	64.06	7.78	8.75	2.75	48	12.47	I	8
46	CH <sub>4</sub> +C <sub>2</sub> H <sub>6</sub>	sII	40	45	06	III	64.18	8.67	7.88	2.50	47.98	5.19	II <sup>f</sup>	4
47	CH <sub>4</sub> +C <sub>2</sub> H <sub>6</sub>	sII	40	45	11.25	III	64.96	10.99	5.64	1.58	48	7.75	II	8
48	CH <sub>4</sub> +C <sub>2</sub> H <sub>6</sub>	sII	40	45	11.25	III	62.54	5.37	10.98	3.57	48	6.43	II <sup>f</sup>	9
49	CH <sub>4</sub> +C <sub>2</sub> H <sub>6</sub>	sII	40	45	18.75	III	64.79	10.42	6.19	1.71	48	7.32	II	9
50	CH <sub>4</sub> +C <sub>2</sub> H <sub>6</sub>	sII	40	45	18.75	III	62.65	5.52	10.84	3.32	48	7.27	II	9
51	CH <sub>4</sub> +C <sub>2</sub> H <sub>6</sub>	sII	40	70	06	IV	63.19	7.23	9.20	2.57	48	17.51	III	5
52	CH <sub>4</sub> +C <sub>2</sub> H <sub>6</sub>	sII	40	70	11.25	IV	62.37	5.18	11.15	3.13	54.30	19.57	III	8
53	CH <sub>4</sub> +C <sub>2</sub> H <sub>6</sub>	sII	40	70	11.25	IV	63.61	8.18	8.30	3.04	48.22	17.45	III	6
54	CH <sub>4</sub> +C <sub>2</sub> H <sub>6</sub>	sII	40	70	18.75	IV	63.87	8.90	7.61	2.14	48	25.19	III	6
55	CH <sub>4</sub> +C <sub>2</sub> H <sub>6</sub>	sII	40	70	18.75	IV	63.72	8.30	8.19	2.72	48	20.27	III	6
56	CH <sub>4</sub> +C <sub>2</sub> H <sub>6</sub>	sII	60	20	11.25	I	62.04	5.57	10.72	8.41	50.38	10.99	I	8
57	CH <sub>4</sub> +C <sub>2</sub> H <sub>6</sub>	sII	60	20	11.25	I	61.92	5.40	10.87	20.06	48.63	11.89	I	8
58	CH <sub>4</sub> +C <sub>2</sub> H <sub>6</sub>	sII	60	70	18.75	IV	61.86	5.58	10.68	7.81	59.94	21.69	III	8
59	CH <sub>4</sub> +C <sub>2</sub> H <sub>6</sub>	sII	60	70	18.75	IV	61.82	5.06	11.21	3.85	48.00	22.57	III	8
60	CH <sub>4</sub> +C <sub>2</sub> H <sub>6</sub>	sII	80	20	11.25	I	59.21	4.10	11.84	8.35	51.60	60.06	IV <sup>g</sup>	8

Table 5.1— Experimental data summary for fresh water, mineral oil, gas mixture and gas hydrate systems with the respective measured data at the onset of the hydrate formation, estimated amount of water converted to hydrate and flow risk index.

Exp.	Gas phase	Hydrate structure	LL [%vol.]	WC [%vol.]	$\omega^a$ [rpm]	Flow regime <sup>b</sup>	PONSET [bar]	T <sub>average</sub> [°C]	Subcooling onset [°C]	t <sub>hydrate onset</sub> [h]	$\Delta t$ [h]	Water Converted [%]	Final Morphology <sup>c</sup>	Flow risk <sup>d</sup>
61	CH <sub>4</sub> +C <sub>2</sub> H <sub>6</sub>	sII	80	20	11.25	I	60.52	6.96	9.14	9.10	51.46	50.95	IV <sup>g</sup>	5
62	CH <sub>4</sub> +C <sub>2</sub> H <sub>6</sub>	sII	80	20	18.75	I	59.53	4.07	11.90	16.17	48.64	57.66	IV	7
63	CH <sub>4</sub> +C <sub>2</sub> H <sub>6</sub>	sII	80	20	18.75	I	63.82	12.97	3.53	1.10	50.99	48.29	IV	4
64	CH <sub>4</sub> +C <sub>2</sub> H <sub>6</sub>	sII	80	45	11.25	II	61.71	12.51	3.74	1.25	62.49	16.95	IV <sup>g</sup>	4
65	CH <sub>4</sub> +C <sub>2</sub> H <sub>6</sub>	sII	80	45	11.25	II	64.10	13.03	3.51	1.01	51.87	12.93	IV	6
66	CH <sub>4</sub> +C <sub>2</sub> H <sub>6</sub>	sII	80	45	18.75	II	62.83	11.38	5.00	1.48	50.91	11.39	IV	6
67	CH <sub>4</sub> +C <sub>2</sub> H <sub>6</sub>	sII	80	45	18.75	II	63.27	12.91	3.52	1.09	49.46	13.16	IV	6
68	CH <sub>4</sub> +C <sub>2</sub> H <sub>6</sub>	sII	80	70	11.25	IV	64.90	14.38	2.25	0.37	50.48	10.76	IV	6
69	CH <sub>4</sub> +C <sub>2</sub> H <sub>6</sub>	sII	80	70	11.25	IV	63.26	12.89	3.55	0.73	69.83	9.07	IV	6
70	CH <sub>4</sub> +C <sub>2</sub> H <sub>6</sub>	sII	80	70	18.75	IV	59.76	4.07	11.93	6.69	49.89	12.25	IV <sup>h</sup>	7
71	CH <sub>4</sub> +C <sub>2</sub> H <sub>6</sub>	sII	80	70	18.75	IV	59.26	12.98	2.96	1.83	49.63	8.12	IV <sup>i</sup>	5

<sup>a</sup> The lowest oscillation rate, 06 rpm, presented poor shear conditions for oil-gas-water systems, therefore few experiments were performed in this condition.

<sup>b</sup> Refer to the map of Figure 5.5 for the classification of the water flow regime in the rock-flow cell before the beginning of hydrate formation.

<sup>c</sup> Refer to the map of Figure 5.12 to classify the final morphology of the oil-gas-hydrate-water system.

<sup>d</sup> Refer to the risk of disruption under the given experimental conditions based on the morphology and associated risk, Figure 5.24.

<sup>e</sup> At the beginning, its behaviour was similar to the experiments of region I. Still, approximately one hour after the beginning of hydrate formation, the agglomerates started breaking into small pieces forming a slurry. In the end, an upper hydrate wall deposit and a flowable hydrate slurry at the bottom were observed.

<sup>f</sup> A thin oil film flowing, almost unnoticeable, above the deposit was observed at the end, indicating that almost all oil phase was trapped in the hydrate porous structure.

<sup>g</sup> The temperature gradient imposed in the cell and the shear conditions broke the bottom wall deposits, thence a thicker upper wall hydrate deposit was observed at the end.

<sup>h</sup> Complete obstruction of the cross-section area. Plug formation with a thicker upper wall hydrate deposit and an enclosed water-free phase was observed at the end of the experiment.

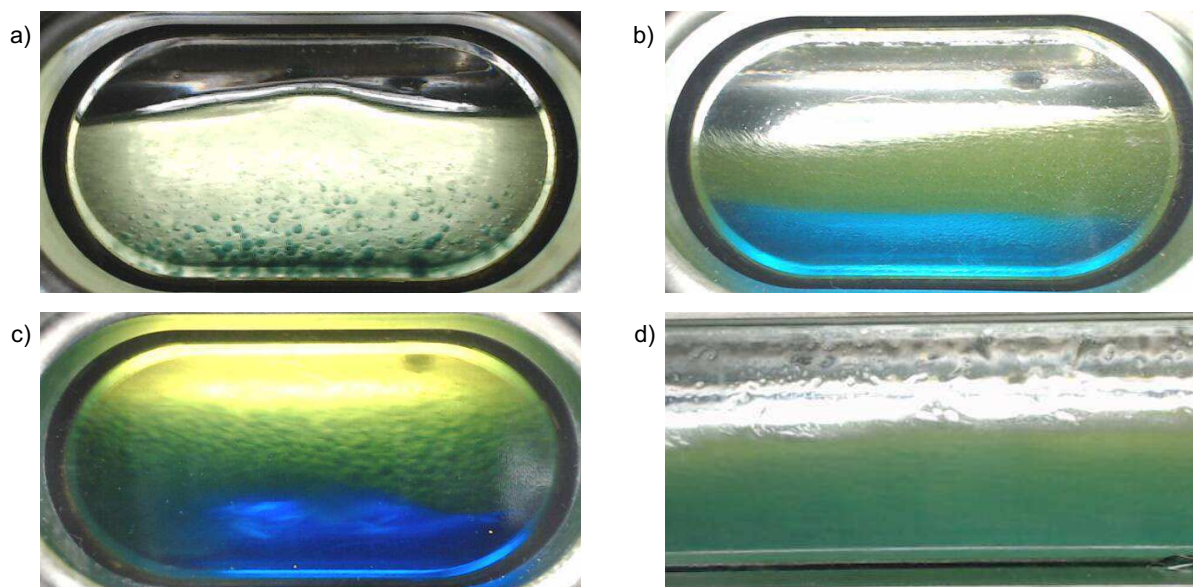
<sup>i</sup> Sloughing events occurred throughout the experiments. At the end, an upper wall hydrate deposit and a flowable hydrate slurry was observed.

## 5.2 Flow conditions before hydrate formation onset

The system hydrodynamics proved to be important to further the understanding on the morphology of the system in the presence of gas hydrates — one of the conclusions shown in Chapter 4 for gas-water systems. The oil-gas-water flow conditions before the onset of the hydrate formation is presented considering the water content (20%vol. to 70%vol.), the liquid loading (40%vol. to 80%vol.) and the rock-flow cell oscillation (6, 11.25 and 18.75 rpm). These parameters affect the dispersion of the liquid phases influencing the oil-gas-water interfacial area and flow energy. They will also give an important insight into the leading mechanism associated with the process of hydrate formation and accumulation in multiphase flow.

Photos of the main flow conditions observed throughout the experiments are presented in Figure 5.1. Letter a) presented a system with water phase dispersed in the oil-continuous phase (experiment #63, 80 %vol. LL and 20 %vol. WC). Letter b) shows a thicker, free water layer with a dispersed water and oil phase (experiment #68, 80 %vol. LL and 70 %vol. WC). A water-free phase at the bottom, an intermediate layer of dispersed water and oil, and an oil phase above (experiment #66, 80 %vol. LL and 45 %vol. WC) is presented in c). Letter d) presents a dispersed water and oil phase at the bottom and an oil phase above (experiment #49, 40 %vol. LL and 45 %vol. WC). The water phase was blue-dyed, whilst the oil phase was yellow-dyed; therefore, the water and the oil dispersed phases appear green in the footage.

Figure 5.1— The oil-gas-water flow images observed before the onset of the hydrate formation throughout the experiments: a) water phase dispersed in the oil-continuous phase (experiment #63, 80 %vol. LL and 20%vol. WC). b) a thicker free water layer with a dispersed water and oil phase (experiment #68, 80 %vol. LL and 70%vol. WC). c) a water-free phase at the bottom, an intermediate layer of dispersed water and oil, and an oil phase above (experiment #66, 80 %vol. LL and 45%vol. WC). d) a dispersed water and oil phase at the bottom and an oil phase above (experiment #49, 40 %vol. LL and 45%vol. WC).

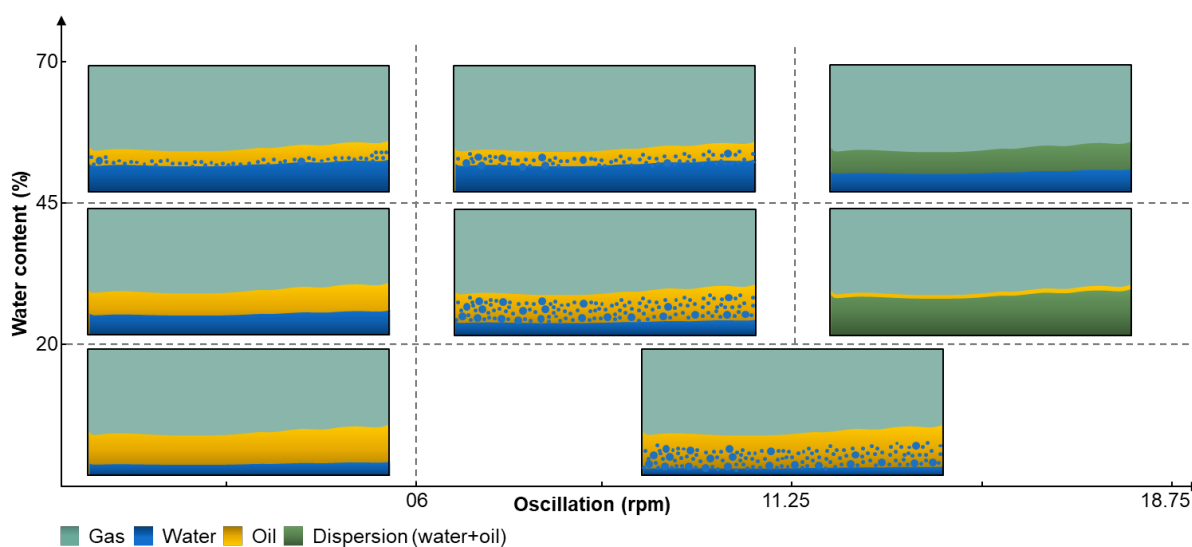


Source: own authorship.

A flow map as a function of the water content and oscillation rate is illustrated in Figure 5.2 for the 40 %vol. of liquid loading based on the footage taken during the experiments. The increases in the percentage of water in the liquid phase increase mainly the thickness of the free water layer at the bottom for low to medium oscillation rates (06 and 11.25 rpm) of the rock-flow cell. For this condition, the flow resembles the image presented in letter a) of Figure 5.1. As the flow energy increases (18.75 rpm), a dispersed layer with a free liquid phase (oil or water, depending on the water content) was observed for medium to high amounts of water in the system (45 and 70%vol. of water content). Because of the difference in the density of the oil and water phase, the flow looks like Figure 5.1.b when the free liquid phase is water; otherwise, it resembles Figure 5.1.d. The presence of the dispersed layer will be later related to a lower water conversion to hydrates.



Figure 5.2— Illustration of an oil-gas-water flow map for 40 %vol. of liquid loading in the rock flow cell before the onset of the hydrate formation as a function of water content and oscillation rate. The categorisation was based on the footage considering what happens in the middle of the rock-flow cell.

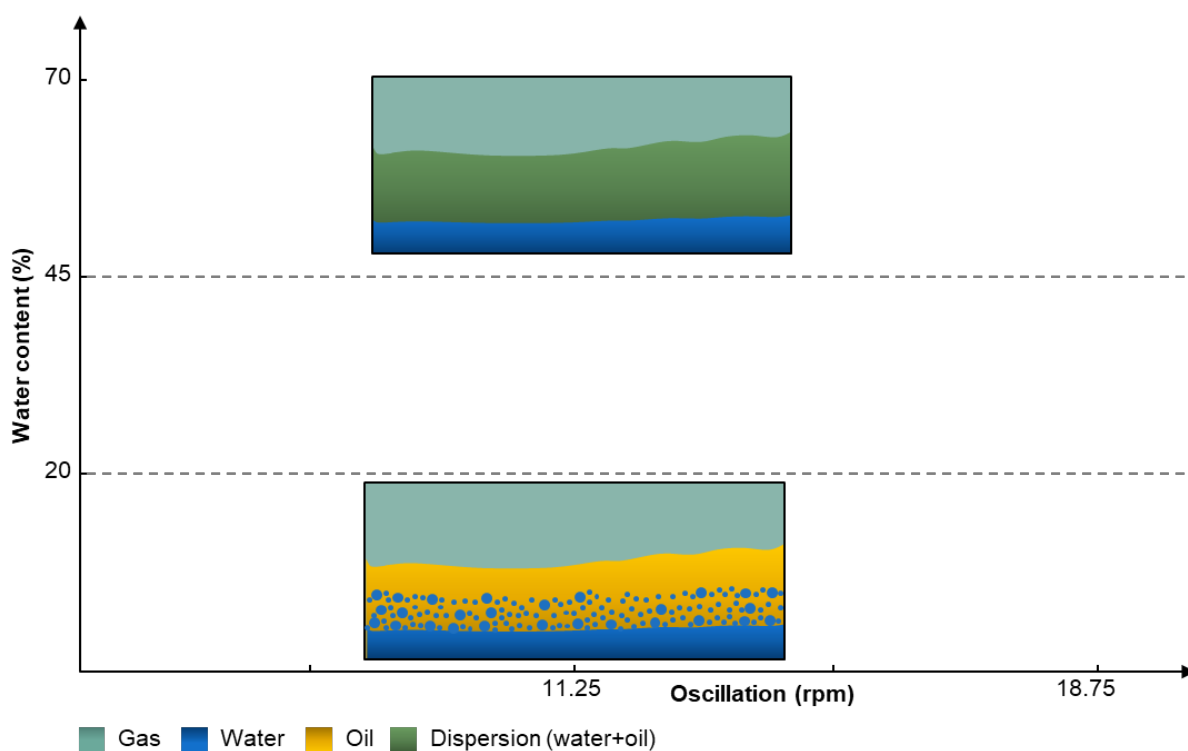


Source: own authorship.

The low oscillation rate, 06 rpm, demonstrated poor shear conditions for oil-gas-water systems. In these cases, the flow conditions could not disperse the liquid phases. The dispersion of the fluids was only observed at the extremities of the rock-flow cell in the recirculation region. Hence, there is no reason to persevere with this experimental condition.

Figure 5.3 illustrates the oil-gas-water flow map before the onset of the hydrate formation for experiments with 60 %vol. of liquid loading. The same trend of the experiments with 40 %vol. of liquid loading for low (< 20 %vol. LL) and high water contents (> 70 %vol. LL) was observed. The increase of the volume of the liquid in the system allowed a better dispersion of the water phase in the oil phase. In addition, that may indicate the influence of water in the flow energy, which may have increased because of the increase in the percentage of water in the system, enabling the formation of the dispersed layer above a water-free phase.

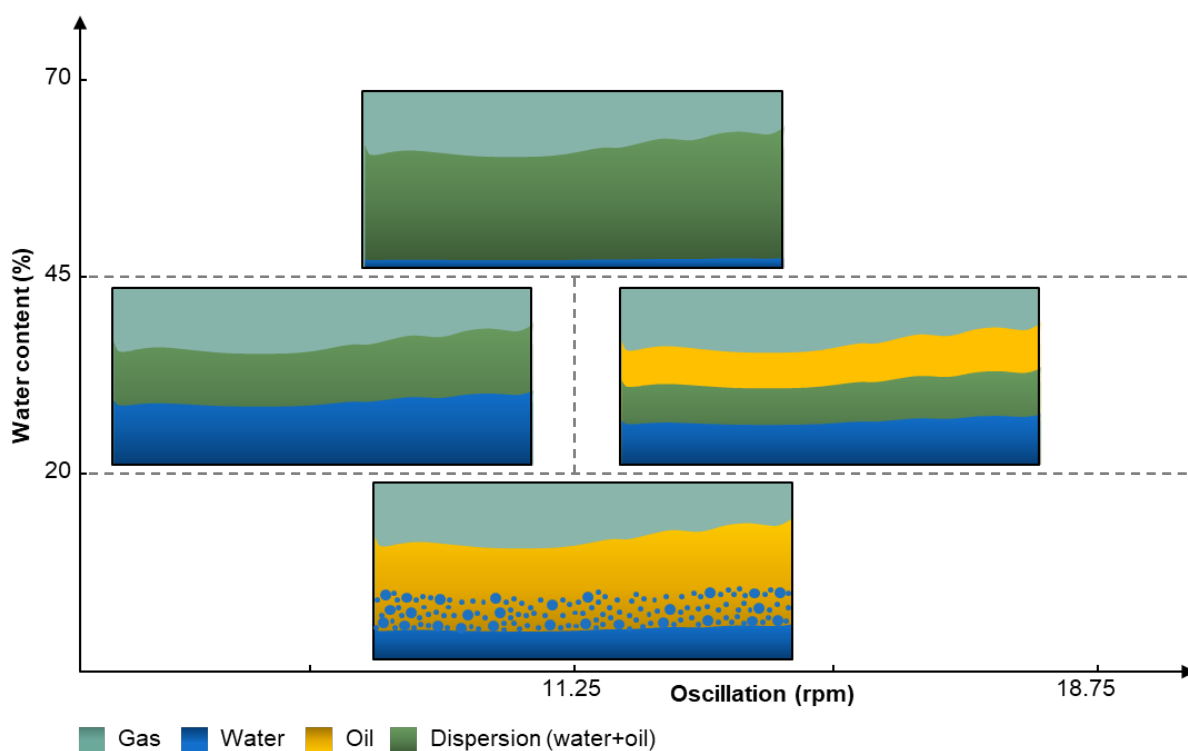
Figure 5.3— Illustration of an oil-gas-water flow map for 60 %vol. of liquid loading in the rock flow cell before the beginning of the hydrate formation as a function of water content and oscillation rate. The categorisation was based on the footage considering what happens in the middle of the rock-flow cell.



Source: own authorship.

Figure 5.4 shows the flow conditions observed for the experiments with 80 %vol. of liquid loading. The experiments with 45 %vol. of water content create a four-phase flow system (gas-oil-dispersion-water). Figure 5.1.c shows a photo of the three liquid phases formed in the system. Probably, the shear stresses in the systems were not able to completely disperse the water in the oil phase, leaving an intermediated phase between the free oil and water phases. Both systems — 70 %vol. of WC and 45 %vol. of WC at a low oscillation rate ( $< 11.25$  rpm) — present the same flow conditions, but it was counter-intuitive to observe a thicker water-free phase in the latter one, which presents a low amount of water in the system compared to the former.

Figure 5.4— Illustration of an oil-gas-water flow map for 80 %vol. of liquid loading in the rock flow cell before the beginning of the hydrate formation as a function of water content and oscillation rate. The categorisation was based on the footage considering what happens in the middle of the rock-flow cell.



Source: own authorship.

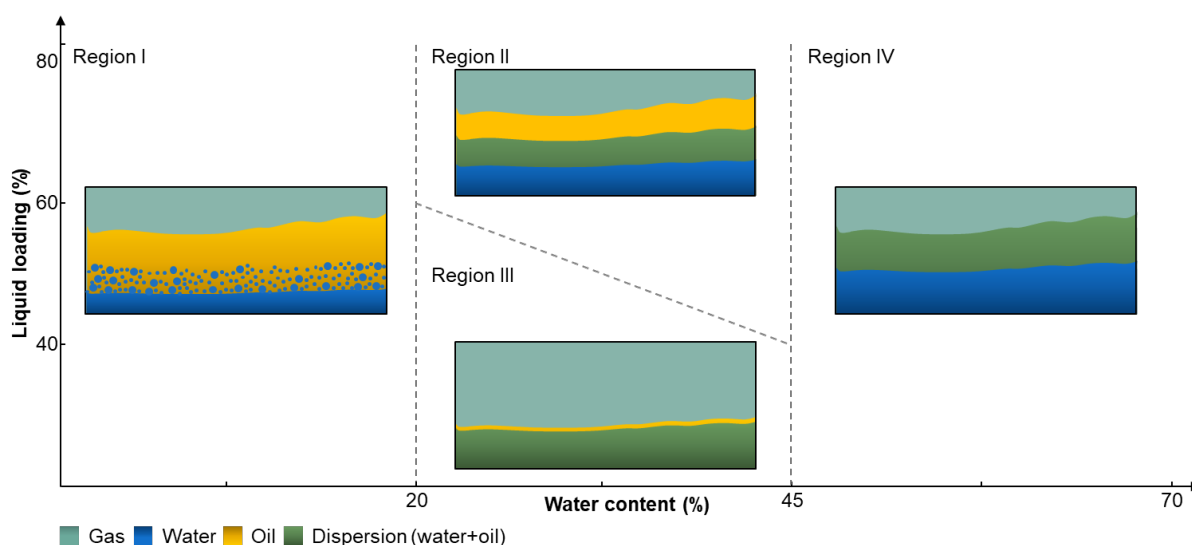
Based on the analysis above, the information was summarised in a flow map, as presented in Figure 5.5, considering the liquid loading and water content parameters. The flow map is independent of the oscillation rate, an explanation for this might be the liquid velocity range studied, which remains in the range of 0.1 to 0.31 m/s, (Marques et al. 2019). The four flow conditions observed before the onset of the hydrate formation for the oil-gas-water system are:

- Region I, the water phase is dispersed in the oil-continuous phase. The water liquid only touches the upper wall at the ends of the rock-flow cell, where a recirculation region is formed. From Figure 5.5, it happens for low water content (< 20 %vol.) independent of the liquid loading. In Figure 5.1, region I corresponds to the conditions of letter a).
- Region II comprises four phases: a water-free phase at the bottom, a layer of dispersed water and oil, an oil phase above it, and a gas phase at the top. The shear stress presented in this system could not completely

disperse the oil phase into the water phase forming an intermediate phase. According to Figure 5.5, it happens for high liquid loading (> 60 %vol.) at a water content around 45 %vol. Figure 5.1.c corresponds to the conditions of region II.

- Region III formed a thicker dispersed water and oil phase with a thin oil phase above. As shown in Figure 5.5, it happens for low liquid loading (< 40 %vol.) at a water content around 45 %vol. Figure 5.1.d resembles the flow conditions of region III.
- Region IV, the system is composed of three phases: a water phase at the bottom, a dispersed water and oil phase above it, and a gas phase at the top. According to Figure 5.5, it happens for high liquid loading (> 80 %vol.) independent of the water content. Figure 5.1.b characterised the flow conditions of region IV.

Figure 5.5— Illustration of an oil-gas-water flow map in the rock flow cell before the onset of the hydrate formation as a function of liquid loading and water content. The categorisation was based on the footage considering what happens in the middle of the rock-flow cell and the velocities analysed.



Source: own authorship.

These classifications may give information about the stability of the dispersion after the onset of the hydrate formation, which will be discussed in subsection 5.3.1. The stability of the dispersion may also affect the gas diffusion amongst the phases influencing the hydrate growth rate, as this process is mass transfer-controlled. As

discussed in Chapter 4, the hydrodynamics of the system before the beginning of the hydrate formation impacted the hydrate deposition for a gas-hydrate-water system, and it is probable that it also affects the final hydrate morphology in an oil-gas-hydrate-water system, which will be considered in the following subsection.

### **5.3 Hydrate morphology of formation and accumulation**

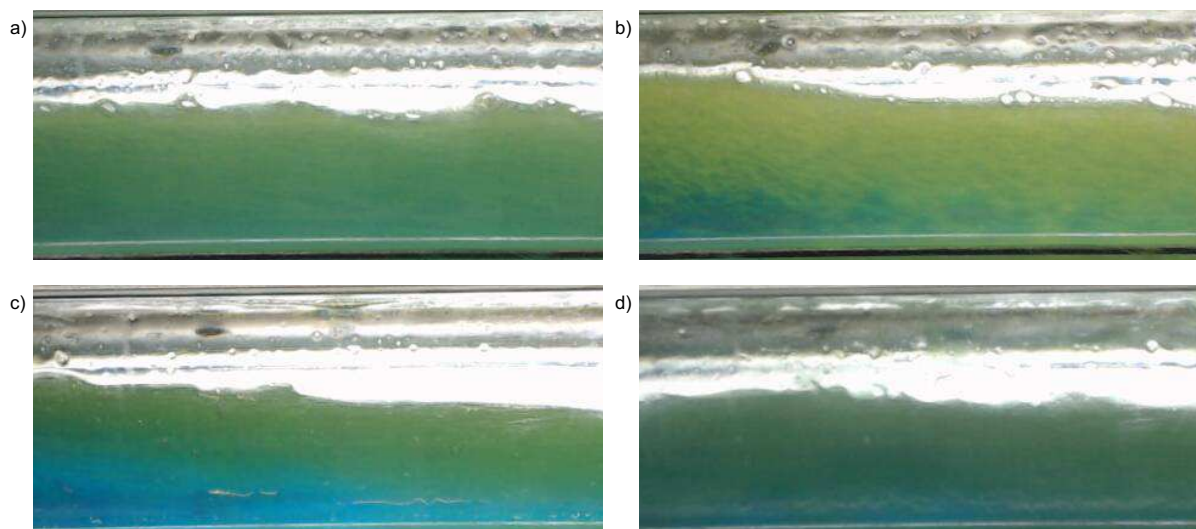
#### **5.3.1 The onset of the hydrate formation and stability of the dispersion**

The set of experiments studied for the oil-gas-water system can form a shear-stabilised dispersion layer before the beginning of the hydrate formation due to the oscillation of the rock-flow cell, as observed in Figure 5.1 (b-d). The mineral oil composition is free of surfactants, and no chemical additive was used to emulsify the system. However, the shear-stabilised dispersion may or may not be phase-separated before the macroscopic detection of hydrates in the system, depending on the experimental conditions. Song et al. (2020) explain these phenomena, phase separation and emulsion stabilisation, based on the wettability of the hydrates. The water-wet hydrate particles absorb nearby water droplets and tend to agglomerate. That causes the coalescence of the dispersed water particles, resulting in a free-water layer that destabilises the water-in-oil dispersion. The stabilisation of the oil-in-water dispersion occurs as a consequence of the water-wet hydrate particles acting as a physical barrier outside the oil droplet avoiding coalescence and, consequently, the formation of a free phase, which promotes the stabilisation of the phases.

The shear stabilised water dispersion in the oil phase for low water content (< 20 %vol.) systems seems to phase separated at the beginning of the hydrate formation. Yet, the phase separation was not clearly observed in all the experiments described herein because of the low amount of water in the system. For high water content (> 70%vol.), the beginning of the hydrate formation stabilises the dispersion, and a flowable slurry is observed. Figure 5.6 shows images of the experiment #49 (40 %vol. LL, 45 %vol. WC and 18.75 rpm) and #54 (40 %vol. LL, 70 %vol. WC and 18.75 rpm). The photos on the left show (letter a and c) the system condition before the beginning of the hydrate formation, and the images on the right are the corresponding

ones on the verge of hydrate formation (letter b and d). Letter b shows the phase separation before the visual observation of hydrates by the naked eye. Letter d shows the formation of a water-oil-hydrate dispersion at the hydrate formation onset.

Figure 5.6— Photos of experiment #49 (letters a and b, 40 %vol. LL, 45 %vol. WC and 18.75 rpm) and #54 (letters c and d, 40 %vol. LL, 70 %vol. WC and 18.75 rpm). a) water and oil dispersion with a thin oil layer at the top before the beginning of the hydrate formation. b) phase separation before hydrate is visually observed by the naked eye. c) two liquid phases before the onset of the hydrate formation: a water and oil dispersion above a water layer. d) dispersed flow after the hydrate formation onset.

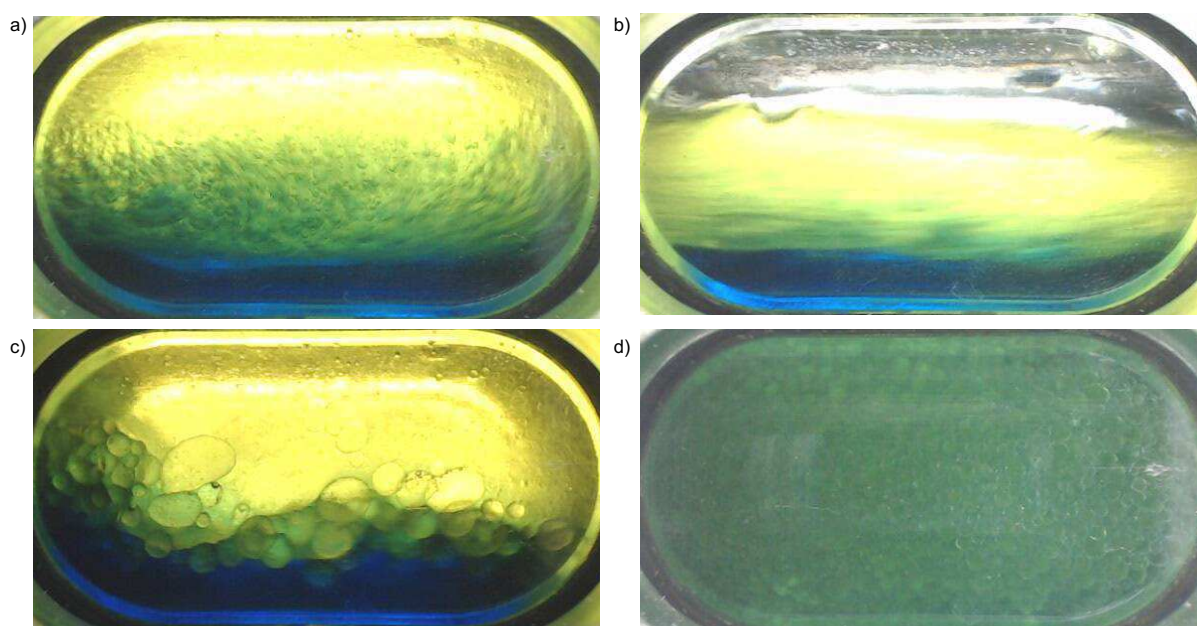


Source: own authorship.

For a medium water content (at around 45 %vol.), the beginning of the hydrate formation appears to be phase-separated for the low to medium liquid loading (< 40 %vol.) systems. However, it stabilises the dispersion for higher liquid loading (> 70 %vol.). An exception was experiment #66 (80 %vol. LL, 45 %vol. WC and 18.75 rpm), when the four-phase system (gas, oil, water-oil dispersion and water-free phase) created an intermediate water-in-oil dispersion which contributed to the coalescence of water droplets at the beginning of the hydrate formation, thus promoting the destabilisation of the dispersion and phase separation which were observed macroscopically. After approximately 2 minutes from the onset of the hydrate formation, the system formed a stabilised single-phase dispersion (hydrate, oil, water); this behaviour might be explained by the water conversion to hydrates, which might have provoked an inversion of the continuous phase. Subsequently, the continuous water conversion to hydrates followed by phenomena such as agglomeration and wave effect cause the appearance of an oil phase. That happens because the oil phase had

not remained trapped inside the porous hydrate structures. Figure 5.7 illustrates these steps with photos taken during the experiments.

Figure 5.7— Photos of experiment #66 (80 %vol. LL, 45 %vol. WC and 18.75 rpm) showing the system's dispersion before the onset of the hydrate formation, the phase separation at the beginning of the hydrate formation followed by the formation of a dispersion. The photos show a) the system before the beginning of the hydrate formation; b) phase separation of the liquid phases, although hydrate formation is not visually observed by the naked eye (5 seconds after the picture of letter a); c) formation of an intermediate phase between the oil and water phases after the beginning of the hydrate formation (the photo was taken 35 seconds after the previous image, letter b); d) a slurry is observed 45 seconds from the previous image (letter c).



Source: own authorship.

### 5.3.2 Characterization of hydrate formation and accumulation

The characteristic of the fluids (water, oil, gas) in the system, the interaction of the phases, flow conditions, and subcooling are some of the parameters influencing the hydrate accumulation and deposition process. Flow conditions before the beginning of the hydrate formation affects the process of hydrate accumulation and wall deposition. The presence of hydrates in the system also affects the flow conditions because of the water consumption during hydrate formation and increased fluid viscosity due to the formation of a hydrate slurry, for example. Increasing the liquid loading or the oscillation rate of the rock-flow cell causes an increase in the average speed of the phases and, consequently, the shear stress in the cell. It is also related to the rise in the dispersion of the phases (water and oil) before the onset of the hydrate

formation. Note that the physical length limitation of the rock-flow cell creates a recirculation zone due to the collision of the fluids at the end of the cell, and it contributes to increasing the dispersion of the phases in this region.

Hydrate formation in the oil-gas-water system must occur on the gas-water and oil-gas-water interface. In this case, this is due to the gas solubilisation and diffusion in the oil phase. This explained the hydrate formation even when the water phase remained stratified in the lower region of the cell. The flow conditions determine the interfacial area amongst the phases. Hydrate formation in the system is accompanied by a pressure drop, a consequence of the isochoric experimental procedure, and a slight increase in the bulk temperature. At the beginning of the hydrate formation, the water-oil dispersion may or may not separate as described in the section, 5.3.1. The hydrate growth in the system increases the apparent viscosity of the liquid phase. The constant oscillation of the rock-flow cell promotes hydrate particle-particle collision and hydrate particle-wall collision. The formation of liquid bridges and capillary effects provoke the adhesion of the hydrates onto the wall or the formation of aggregates.

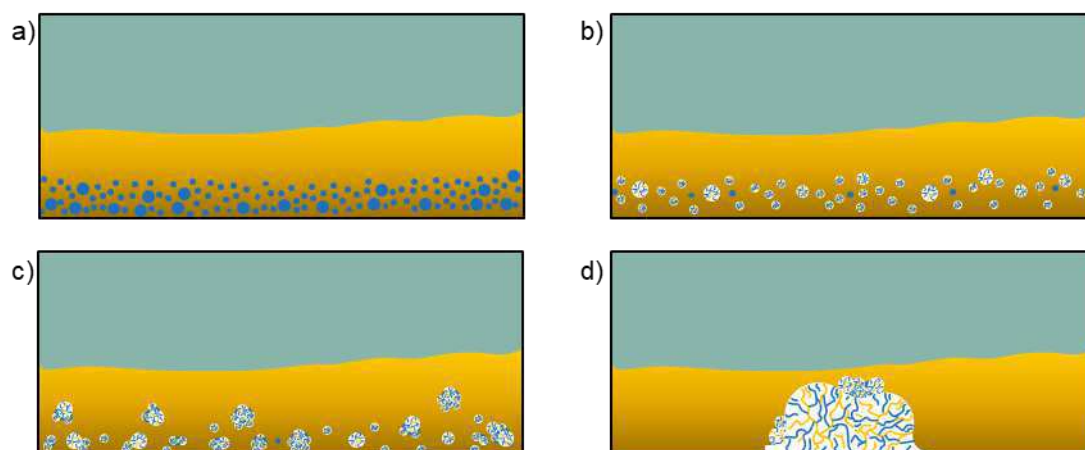
The crystallisation of the liquid bridge, formed between the hydrate particle and the wall, creates the first layer of the hydrate deposit, as a consequence of the presence of free water after the beginning of the hydrate formation. The constant supply of hydrate-forming components can subsequently build a thicker hydrate deposit. The crystallisation of the aggregates capillaries forms agglomerates that can differ in size. The size of the agglomerate will be a result of the capillary effect, shear forces, contact time and subcooling. If the flow energy is insufficient to keep the agglomerate suspended in the flow, they eventually settle, forming a bedding and later depositing on the bottom of the cell.

The continuous phase (water or oil) before the onset of the hydrate formation and the inversion of such phase — if it happens — after the hydrate formation due to water conversion to hydrates in the system determine the primary mechanism leading to hydrate accumulation and deposition in the system. No free water was observed at the end of the experiments, except for experiment #70 (80 %vol. LL, 70 %vol. WC, and 18.75 rpm). Yet, not all water in the system was converted to hydrates, meaning that the remaining water was trapped in the porous hydrate structure.



Figure 5.8 illustrates the process of hydrate formation and accumulation for low water content ( $< 20\%$  vol.) and for low to medium liquid loadings (40 to 60 %vol.). Before the beginning of hydrate formation, the flow condition was composed of water dispersed in the oil phase. At the beginning of the hydrate formation, hydrate particles flow freely in the bulk. Because the rock-flow cell is in constant motion, the hydrate particles eventually collide with each other forming agglomerates (chunks) of hydrates. The agglomerate settles if the flow energy is not enough to keep them suspended in the flow, and, in these cases, it may later consolidate on the bottom wall of the rock-flow cell. In the end, the oil phase flows freely along the rock-flow cell without visible hydrate particles or water-free phase.

Figure 5.8— Illustration of the process of hydrate formation for low water content ( $< 20\%$  vol.) and for low to medium liquid loading (40 to 60 %vol. LL): a) flow characteristic before the onset of the hydrate formation, stratified wavy oil and water layer with a thin layer of dispersed water above a thin water film; b) the onset of the hydrate formation with hydrate particles flowing in the bulk; c) collision of hydrate particles forms agglomerates; d) the agglomerates settles and consolidates on the bottom of the cell with no free water available in the system.

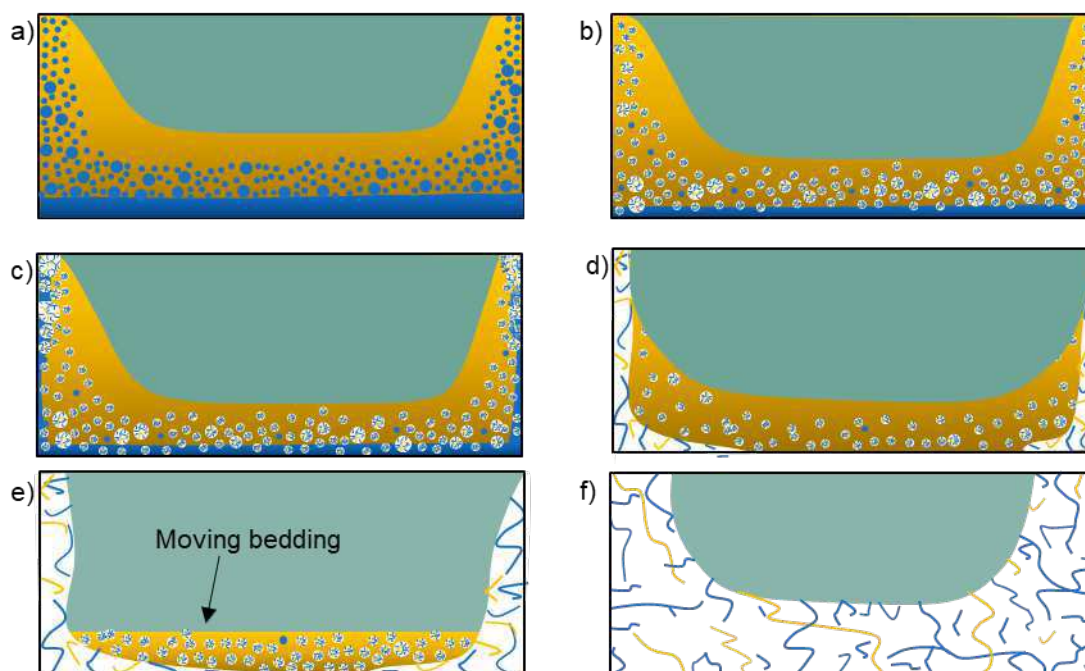


Source: own authorship.

For the combination of middle water content ( $20 < WC < 45\%$  vol.) and for low to medium liquid loading ( $40 < LL < 60\%$  vol.), hydrate particles flow dispersed in the bulk as a slurry forming a stabilised dispersed phase (water-oil-hydrate phase) at the onset of the hydrate formation. Eventually, hydrate particles adhered to the pipe wall creating an accumulation of hydrate particles on the laterals just above the liquid flow. Hydrate particles flow in the bulk, whereas the hydrate deposit grows because of the presence of hydrate-forming compounds and the adhesion of hydrate particles which were floating in the bulk. The liquid phase in the system gradually decreases as the

water is converted to hydrates and the liquid phase gets trapped inside the hydrate porous structure. In the end, the system dries up, with no visible liquid flowing. The oil phase and the remaining water (unconverted water) were trapped inside the porous hydrate deposits on the bottom of the cell. Figure 5.9 shows an illustration of the process of hydrate formation and accumulation in this kind of system.

Figure 5.9— Illustration of the process of hydrate formation for middle water content (20 to 45 %vol.) and for low to medium liquid loading (40 to 60 %vol. LL): a) flow characteristic before the onset of the hydrate formation, an oil layer at the top, a dispersed layer of water in oil, and a water-free phase at the bottom; b) the onset of the hydrate formation with hydrate particles flowing dispersed in the bulk as a slurry forming a stabilised dispersed phase (water-oil-hydrate phase); c) hydrate particles adhered to the pipe wall; d) a thin layer of hydrate deposit is created on the laterals of the cell; e) hydrate deposit growth in the presence of a flowable hydrate slurry; f) the liquid phase dries out. The oil phase and the remaining water in the system were trapped inside the porous hydrate deposits on the bottom of the cell.

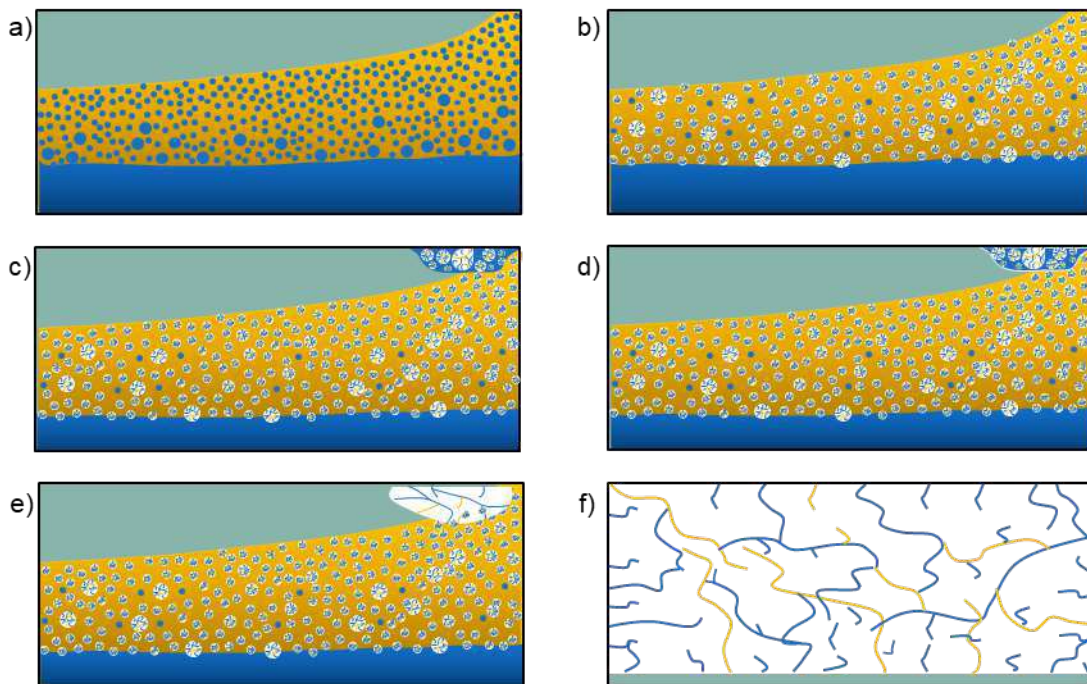


Source: own authorship.

For water content higher than 45 %vol. WC and for low to medium liquid loading ( $40 < LL < 60$  %vol.), hydrate particles flow dispersed in the bulk, forming a stabilised dispersed phase (water-oil-hydrate phase) at the beginning of the hydrate formation. A few minutes after the formation ( $< 2$  min), hydrate particles start adhering and accumulating onto the pipe wall forming hydrate deposits on the lateral of the rock-flow cell. The position of the hydrate deposit on the laterals of the cell changes according to the liquid loading, but the preferred region for the hydrate deposition is the upper

region because of the low energy flow compared to the liquid bulk and the constant feeding of gas and water particles due to the motion of the cell. The constant wetting of the hydrate structure adhered onto the wall rapidly increases the deposition, forming a thicker hydrate deposit a few minutes after the beginning of the hydrate formation (approximately < 30 min). Figure 5.10 illustrates this process of hydrate formation and accumulation. In this case, a free water or oil phase was observed at the end of the experiments. This behaviour is similar to the 100% water-cut (oil-free) experiments presented in Chapter 4.

Figure 5.10— Illustration of the process of hydrate formation for high water content (> 45 %vol.) and low to middle liquid loading (40 to 60 %vol. LL): a) flow characteristic before the onset of the hydrate formation, a dispersed layer of water in oil with a water layer at the bottom; b) the onset of the hydrate formation with hydrate particles flowing dispersed in the bulk forming a stabilised dispersed phase (water-oil-hydrate phase); c) hydrate particles adhered to the pipe wall; d) the preferred region for hydrate deposition is the upper one because of the lower flow energy; e) the hydrate deposit is constantly wetted because of the tilting of the cell forming a thicker hydrate deposit few minutes (< 30 min) after the onset of the hydrate formation. Because of the high volume in the system, a water-free or oil phase can be observed at the end of some experiments. This behaviour is similar to the 100% of water content (oil-free) experiments.

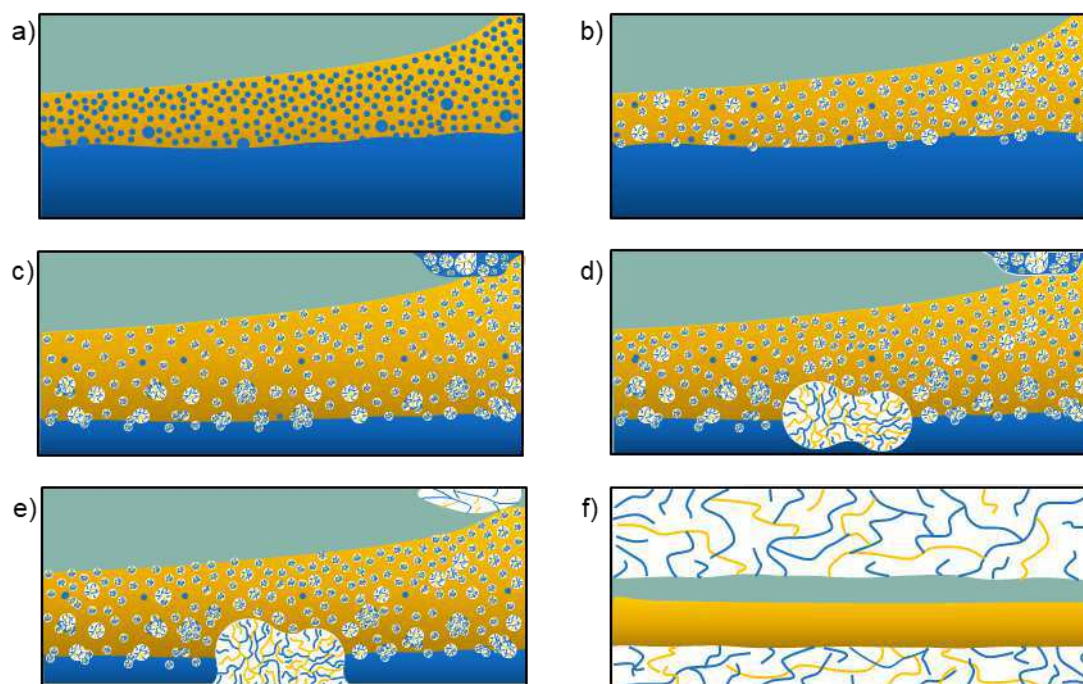


Source: own authorship.

The presence of hydrate deposits on the upper wall and agglomeration in the bulk, see Figure 5.11, indicates a hybrid region (> 80 %vol. LL, independent of the water content). At the beginning of the hydrate formation, hydrate particles flow dispersed in the bulk, forming a stabilised dispersed phase (water-oil-hydrate phase).

A few minutes later, some hydrate particles adhered to the pipe wall forming hydrate deposits on the laterals of the cell. Some hydrate particles which were floating in the bulk may collide forming agglomerates of hydrates of different sizes. The constant motion of the rock-flow cell keeps wetting the upper hydrate structure, and the contact with the gas phase contributes to the formation of thicker hydrate deposits on the top of the cell. As the flow energy was insufficient to keep the agglomerates suspended in the flow, they eventually settled, forming a bed and later depositing on the bottom of the cell. The size of the agglomerate will be a result of the capillary effect, shear forces, contact time and subcooling.

Figure 5.11— Illustration of the process of hydrate formation for high liquid loading ( $> 80\%$  vol. LL): a) flow characteristic before the onset of the hydrate formation, a dispersed layer of water in oil with a water layer at the bottom; b) the onset of the hydrate formation with hydrate particles flowing dispersed in the bulk, forming a stabilised dispersed phase (water-oil-hydrate phase); c) some hydrate particles adhered to the pipe wall and some hydrate particles float in the bulk; d) hydrate deposits start forming on the laterals, whereas agglomerates start forming in the bulk; e) the upper hydrate deposit is constantly wetted due to the motion of the cell forming a thicker hydrate deposit whereas the agglomerates settle forming a bed and later a bottom deposit. This behaviour may represent a hybrid region with two fundamental mechanisms: wave effect and agglomeration.

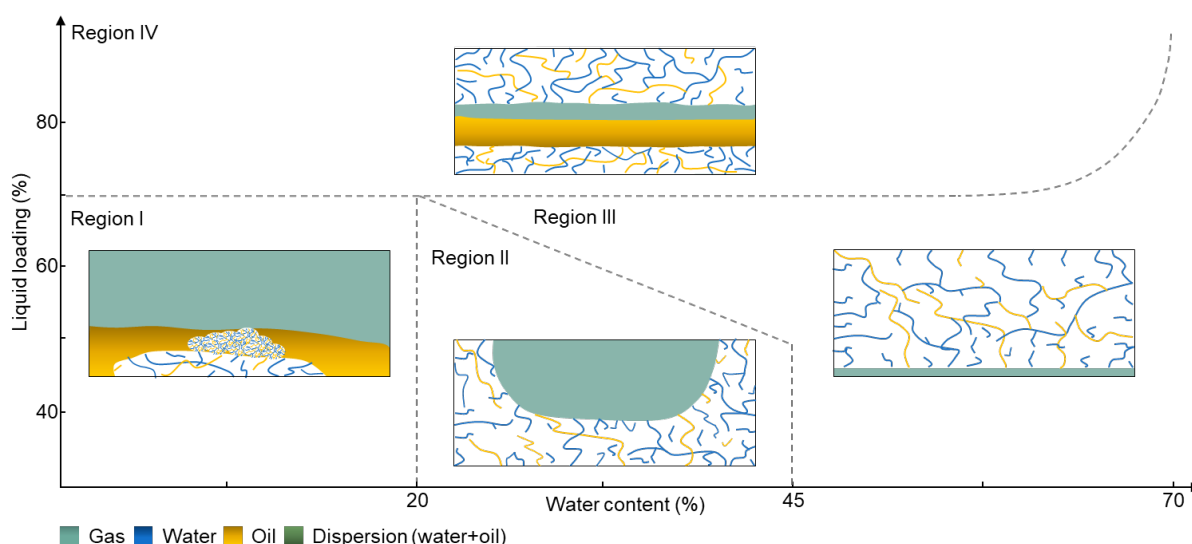


Source: own authorship.

Figure 5.12 summarises the morphology of the hydrate deposits observed in the rock-flow cell for an oil-gas-hydrate-water system at the end of the experiments. The final morphology in this kind of system can be classified into four categories: regions I

to IV. These regions were described in Figure 5.8 to Figure 5.11, respectively. Region I presents hydrate agglomeration followed by deposition on the bottom. The formation process of Region I was described in Figure 5.8. Figure 5.9 exemplifies the formation process of Region II, which shows lateral and bottom wall hydrate deposits without forming a liquid phase in the system. Region III corresponds to the formation of a thicker upper hydrate deposit, whose formation process was illustrated in Figure 5.10. The upper and bottom hydrate wall depositions of region IV, independent of the water content in the system, corresponds to the process described in Figure 5.11.

Figure 5.12— Illustration of final hydrate morphology as a function of the liquid loading and the water content based on the characteristic oil-gas-water flow map for rock-flow cell experiments. The captured images at three different positions of the rock-flow cell were the basis for the general categorisation. In region I, hydrate agglomeration is the primary mechanism of accumulation. In region II, the liquid phase dried up, indicating that part of the fluid was trapped in the lower porous hydrate structure. Region III is dominated by the hydrate deposition. Region IV is a hybrid region where hydrate wall deposition and agglomeration followed by settling are presented.



Source: own authorship.

The kind of water and oil dispersion before the onset of the hydrate formation was relevant to the classification of the regions. Through Figure 5.5 and Figure 5.12, it is possible to verify the influence of the system condition before the beginning of the hydrate formation with the final hydrate morphology. These regions also indicate the primary mechanisms or junctions of mechanisms present in the process of hydrate accumulation and deposition.

Figure 5.13 shows photos of experiments #57 (60 %vol. LL, 20 %vol. WC and 11.25 rpm), #47 (40 %vol. LL, 45 %vol. WC and 11.25 rpm), #58 (60 %vol. LL,

70 %vol. WC and 18.75 rpm), and #69 (80 %vol. LL, 70 %vol. WC and 11.25 rpm). Letter a) demonstrates the process of hydrate formation for low water content (< 20%vol.) and for low to medium liquid loading (40 to 60 %vol. LL), letter b) the process of hydrate formation for middle water content (20 to 45 %vol.) and for low to medium liquid loading (40 to 60 %vol. LL); letter c) the process of hydrate formation for high water content (> 45 %vol.) and low to middle liquid loading (40 to 60 %vol. LL), and letter d) the process of hydrate formation for high liquid loading (> 80 %vol. LL). These photos illustrate the process of hydrate formation described above from Figure 5.8 to Figure 5.11, and grouped in Figure 5.12.

Figure 5.13— Captured images of the rock-flow cell: a) experiment #57 (60 %vol. LL, 20 %vol. WC and 11.25 rpm) representing the conditions for low water content and low to medium liquid loading system, b) experiment #47 (40 %vol. LL, 45 %vol. WC and 11.25 rpm) representing the conditions for middle water content (20 to 45 %vol.) and for low to medium liquid loading (40 to 60 %vol. LL), c) experiment #58 (60 %vol. LL, 70 %vol. WC and 18.75 rpm) representing the conditions for high water content (> 45%vol.) and low to middle liquid loading (40 to 60 %vol. LL), d) experiment #69 (80 %vol. LL, 70 %vol. WC and 11.25 rpm) representing the conditions for high liquid loading (> 60 %vol. LL).



Source: own authorship.

In Figure 5.13, letter a) presents hydrate agglomeration followed by bottom deposition, corresponding to the condition of Region I in Figure 5.12. Letter b) shows lateral and bottom wall hydrate deposits without a liquid phase in the system at the end, representing the conditions of Region II in Figure 5.12. Letter c) presents the

thicker upper hydrate deposit of Region III in Figure 5.12. Letter d) shows the upper and bottom hydrate wall deposition of Region IV in Figure 5.12.

For low water content ( $< 20$  %vol.), the hydrate deposition on the bottom wall is more predominant than the deposition on the upper wall. In contrast, for high water content ( $> 20$  %vol.), a relation between the oscillation rate and temperature gradient inside the rock-flow cell on the thickness of the upper and bottom deposits was noticed. In general, forcing a temperature gradient inside the cell or increasing the flow velocity (by increasing the oscillation rate) favours the formation of a thicker upper hydrate deposit. The exceptions were experiments #65 (80 %vol. LL, 45 %vol. WC and 11.25 rpm) and #66 (80 %vol. LL, 45 %vol. WC and 18.75 rpm). Overall, it was noticed that by increasing the water content in the system, the process of hydrate accumulation behaves analogously to the experiments with 100% of water content (oil-free).

#### **5.4 Mechanisms related to hydrate wall deposition**

An issue in the process of hydrate accumulation under multiphase flow conditions is how hard it is to distinguish between the final hydrate morphology from different systems and experimental apparatuses and the phenomena involved in it. The identification of the regions in Figure 5.12 can be applied as a general classification for an oil-gas-hydrate-water system, as it is based on fundamental, well understood mechanisms found in the literature. The different morphologies occur depending on the competition between the two phenomena: hydrate agglomeration and wave effect. Hydrate agglomeration was the predominant mechanism in the region I leading to hydrate accumulation and settling at the bottom of the pipe. The wave effect is the leading mechanism in regions II and III, related to hydrate wall deposition. The combination of these two predominant mechanisms, agglomeration and wave effect, formed a hybrid zone defined as region IV in the figure.

Because no visual changes in hydrate morphology were observed between the first minutes of the hydrate formation ( $< 30$  min) and the end of the experiments, it is assumed that the primary mechanism, present at the first hour of hydrate formation and growth, has a stronger influence on the process of accumulation and deposition.



#### 5.4.1 Agglomeration and settling

In the systems where the water droplets are dispersed in the continuous phase without the presence of a water-free phase, the process of hydrate accumulation is led mainly by the agglomeration of hydrate particles due to the capillary forces — which holds the solid particles together after the collision.

Hydrate formation takes place on any gas-water interface. The hydrate particles behave like solid particles and flow freely on the liquid bulk at the beginning of the hydrate formation. The hydrophilic nature of the hydrate particles and the porous structure (like a sponge) that covers the outside of the hydrate particle with water— should it not be a dry particle as a consequence of the rapid conversion of the water inside the porous when in the presence of a higher subcooling, for example — favours the formation of a capillary bridge when in the presence of an immiscible phase, which in this case is the mineral oil. Eventually, one hydrate particle collides with another because of the dynamic flow conditions. The capillary bridge holds the particles together, forming an aggregate. Depending on the contact time and flow conditions, the bridge can crystallise, consolidating the aggregate, and establishing an agglomerate. Further aggregation and crystallisation can increase the size of the agglomerate.

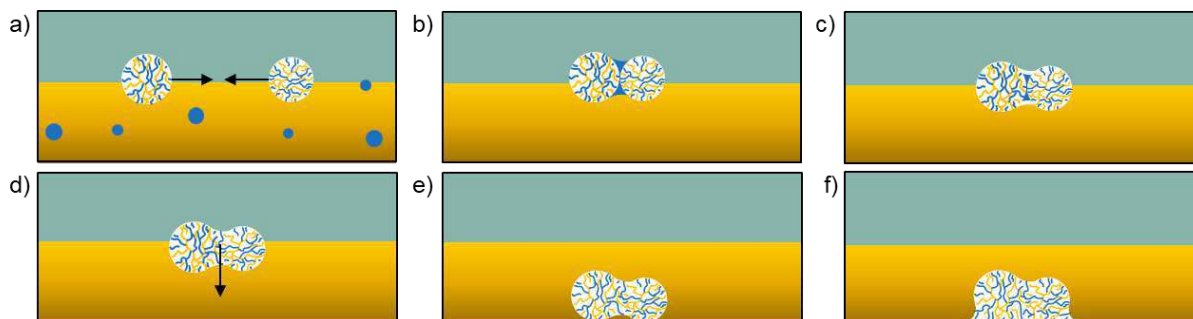
The agglomeration process takes place whilst the hydrate particles are water-wet. The size of an agglomerate is a function of the cohesion force between particles, fluid viscosity of the continuous phase which carries the solid particles — the viscosity influences the rate of collision —, flow conditions which controls the size of the agglomerate —the flow energy can disrupt the agglomerate dispersing in the flow but can also increase the particle collision rate favouring the agglomeration process — subcooling — higher subcooling can seal the outer surface of hydrate particles preventing further agglomeration.

Suppose the flow energy is insufficient to keep the agglomerate suspended in the flow. In that case, it will settle at the bottom of the pipe, forming a bedding layer. The difference between hydrate bottom deposition and bedding is that in the latter case, the agglomerates could still move at a slower velocity than that of the liquid

phase. The settled agglomerates can be later converted to a solid deposit at the bottom with the continuous oil phase flowing freely above (flow with stationary bed).

Figure 5.14 depicts the process of hydrate agglomeration: a) hydrate particles dispersed in the bulk; b) eventually, a hydrate particle collides against another hydrate particle, and because of the capillary bridge formed on the surface of the particle, oil and gas phases, they stick together, forming an aggregate — the aggregates can be easily separated by the flow energy; c) and d) the crystallisation of the capillary bridge forms the first agglomerate; e) if the motion of the rock-flow cell does not provide enough force to lift the agglomerate, the agglomerate settles forming a moving bedding at the bottom; f) otherwise, the agglomerate may consolidate at the bottom forming a deposit.

Figure 5.14— Description of the process of particle aggregation, cristallisation and agglomeration, which leads to the formation of a bedding layer or hydrate deposits on the bottom of the pipe. a) particles dispersed into the bulk; b) collision of the particle against another particle; c) the particle remains attached because of the capillary bridge formed on the particle surface, oil and gas phases; d) cristallisation of the capillary bridge forming the first agglomerate; e) if the motion of the rock-flow cell does not provide enough force to lift the agglomerate, the agglomerate settles forming a moving bedding at the bottom; f) the agglomerate may consolidate at the bottom forming a deposit.



Source: own authorship.

During the experiments, the agglomeration mechanism is present in systems with liquid loading up to approximately 70 %vol. and low water content (< 20 %vol.). The low amount of water in the system contributed to the formation of water dispersed in the oil-continuous phase. This may favour the predominance of the agglomeration mechanism. For a higher amount of water in the system (> 20 %vol.), the primary mechanism related to the hydrate accumulation is changed. For higher liquid loading, a combination of mechanisms, which includes the agglomeration mechanism, was responsible for the accumulation of hydrates.

#### 5.4.2 Wave effect

When free water exists after the beginning of the hydrate formation in an oil-gas-hydrate-water system, the hydrate wall deposition process will be controlled by the wave effect. Under these conditions, the wave effect acts in the same manner as in a 100% water-cut system. Hydrate particles are driven onto the wall by waves because of the flow conditions, and the liquid bridges hold them attached to the wall. The waves and their frequency influence the hydrate deposit profile. As the waves break on the surface of the deposit, new particles can get attached, increasing the size of the deposit, or particles can be detached from the surface of the deposit, decreasing its size or provoking sloughing events before flowing back into the trough (crest falling pushes the former troughs upwards and the wave moves forwards — or backwards because of the oscillation motion of the rock-flow cell). The swash and backwash movements create the deposit, which might characterise most deposits of hydrates in multiphase flow — for stratified wavy or slug flow pattern. Therefore, the naming of the process of hydrate deposition is based on the multiphase flow movement, and the mechanism involved is the liquid bridge formed on the gas, hydrate wet particle and wall interfaces.

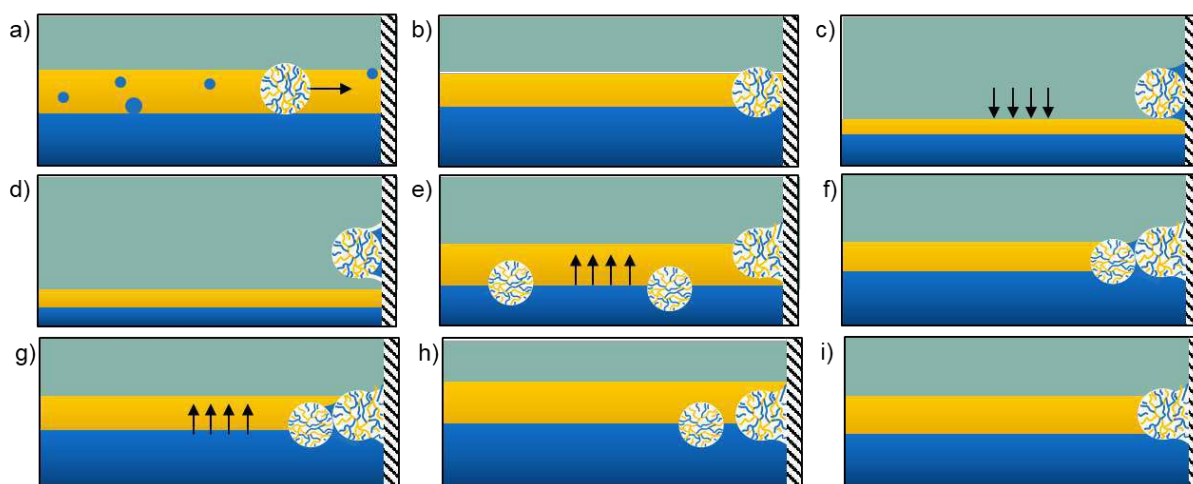
Hydrate particles nucleate in the bulk on any gas-water interface. As more water is converted to hydrates, the bulk phase gradually becomes a hydrate slurry, increasing the apparent bulk viscosity. The motion of the rock-flow cell promotes the collision between hydrate particles and between particles and the wall. The liquid bridge forms between the hydrate particle and the wall because of the presence of a free-water phase in the system, the hydrophilic and porous nature of hydrates, and the pipe wall is made of hydrophilic material. The liquid bridge keeps the hydrate particles attached to the wall; if the water bridge crystallises, it consolidates the hydrate particle in the wall forming the first hydrate deposit layer. However, if the flow energy is enough to overcome the adhesion force, the hydrate particle will detach from the wall.

The wavy motion of the liquid phase (retraction and expansion) keeps supplying hydrate-forming compounds (water and gas) to the hydrate deposit layer, and hydrate particles which can attach to the former hydrate deposit. Therefore, the deposit growth is due to the crystallisation of the water provided by the flow, conversion of the water trapped inside the porous hydrate particle and the attachment of new particles which

were floating in the bulk. In field conditions, the same dynamic conditions might be present in a steady flow.

Figure 5.15 illustrates the process of hydrate particle wall deposition for oil-gas-hydrate-water systems. In the systems studied, increasing the amount of water (above 20 %vol.) favoured the phenomenon of hydrate wall deposition. However, the position of the hydrate deposit changes considerably with the liquid loading. At high liquid loading (up to 70% vol.), regardless of the water content, a hybrid region forms, exhibiting hydrate wall deposition and hydrate agglomeration at the bottom of the cell. No visible changes in hydrate morphology were observed from the beginning of the hydrate formation (after approximately 30 minutes from the onset of the hydrate formation) until the end of the experiments.

Figure 5.15— Description of the particle deposition process on the wall, called wave effect, for gal-oil-water systems, which leads to the formation of hydrate deposits. a) hydrate particle dispersed into the bulk; b) collision of the particle against the wall; c) contraction of the flow, whereas the particle remains attached to the wall because of the liquid bridge formed on the particle surface, wall and gas phases; d) consolidation of the liquid bridge forming the first layer of the deposit; e) the motion of the rock-flow cell wets the surface of the deposit once again providing water, oil and new particles which are dispersed into the bulk; f) new particles adhere to the deposit and may or may not consolidate; g), h), i) eventually, the flow can wash particles out of the deposit if they are not consolidated (time-dependent) and depending on the shear rate.



Source: own authorship.

In the cases where hydrates deposit on the wall in the absence of a water-free phase in the system after the beginning of hydrate formation, the deposition process might be due to the splash effect. The impact of the hydrate particles on the wall, which comes from the rock-flow cell tilting, can cause a reorganisation of the structures of the hydrate particles, causing the coalescence of water molecules, wetting the surface of

the hydrate particles and forming liquid bridges with the wall. Consequently, even in oil continuous flow with some dispersed water, hydrate deposits can develop due to the splash effect. This effect should not be able to develop a thick hydrate deposit. However, the bottom deposition due to the settlement of the agglomerates might come from the splash effect.

Therefore, for the hydrate deposition to occur due to the wave effect, the following conditions must be satisfied — otherwise, the splash effect is the cause: the wall must present affinity to the water phase (hydrophilic material), water should exist as a free phase after the beginning of hydrate formation, and the gas phase needs to reach the surface of the deposit for a quick crystallisation of the liquid bridge. The conditions for a water-free phase to exist after the beginning of the hydrate formation are a water continuous system, a high water content system or phase separation before the beginning of the hydrate formation by the naked eye. The subcooling and shear conditions influence how fast the deposit forms and grows and influence the stability of the deposits as well.

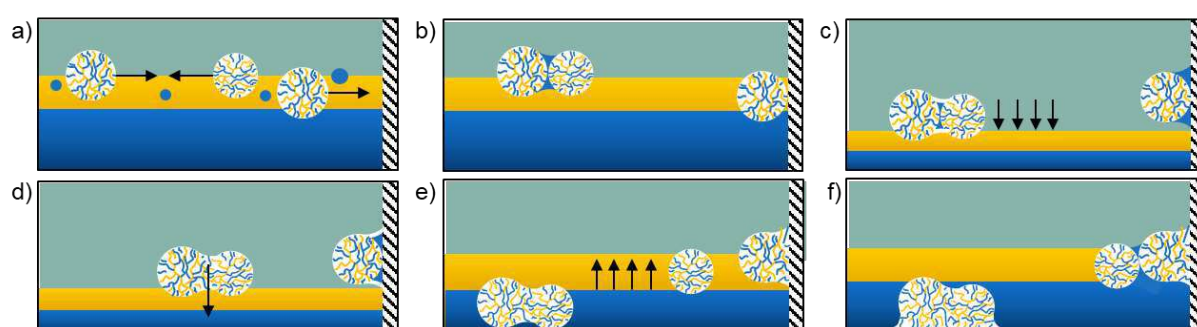
#### 5.4.3 Hybrid systems

For high liquid loading (> 70 %vol.) independent of the water content in the system, a combination of hydrate agglomeration and wall deposition mechanisms rather than one primary predominant mechanism were observed, meaning that a hybrid region exists. In the hybrid region, the competition of the two mechanisms will define the final hydrate morphology in the system. In this condition, the shear stress and flow conditions might be fundamental to determining the thicknesses of the hydrate upper and bottom wall deposits.

Figure 5.16 describes the combination of the agglomeration and wave effects in oil-gas-hydrate-water systems. Hydrate nucleation occurs on any gas-water interface when inside the hydrate phase-envelop. At the beginning of the hydrate formation, hydrate particles flow in the bulk phase. As water converts into hydrate, the apparent viscosity of the bulk phase increases. The dynamic motion of the rock-flow cell increases the collision among hydrate particle-particle and hydrate particle-wall. The particle-particle collision forms a capillary bridge between them, and at this point,

creating an aggregate which is an unstable form of an agglomerate — it is easier to disrupt the particles — and depending on flow conditions and contact time, this bridge crystallises to form an agglomerate. The agglomeration process occurs whilst the agglomerates are water-wet. Depending on the agglomerate size and flow conditions, the agglomerates can settle, forming a moving bed at the bottom of the cell, which subsequently can deposit. The particle that collides with the wall creates a liquid bridge on the particle-gas-wall interface. The bridge consolidates on the wall — depending on the flow energy as it can detach the particle from the wall and on the contact time to crystallise the bridge— establishing the first hydrate deposit layer. The deposit grows because of the crystallisation of the water provided by the flow, conversion of the water trapped inside the porous hydrate particle and the attachment of new particles, that were floating in the bulk. These two mechanisms will be responsible for the bottom and upper wall deposition, respectively.

Figure 5.16— Description of the process of particle deposition on the wall and agglomeration followed by settlement for the hybrid region in an oil-gas-hydrate-water system, which leads to pipe cross-section reduction. a) hydrate particle dispersed into the bulk; b) collision of the particle against the wall and another particle; c) contraction of the flow whereas the particle remains attached to the wall because of the liquid bridge formed on the particle surface, wall and gas phase, and particle-particle capillary bridge formed on the particle, oil, water interface; d) crystallisation of the liquid bridge forming the first layer of the deposit on the wall and crystallisation of the capillary bridge forming an agglomerate in the bulk; e) the motion of the rock-flow cell wets the surface of the deposit once again providing water, oil and new particles which were dispersed into the bulk and eventually the agglomerates settled, establishing a bedding layer in the cases where the flow energy is not enough to lift the agglomerates; f) the wall deposits grow, and the size of the agglomerates increases whilst the hydrate particles are water-wet, and eventually, the bedding layer can become a deposit.



Source: own authorship.

In the experiments performed, although the high amount of liquid in the system changed the flow conditions and contributed to an increase in the shear stresses and to the dispersion of the oil and water phases, the flow energy was not enough to keep the particles suspended in the flow, causing the bottom wall deposition. The

competition of the agglomeration and the wave effect mechanisms might have prevented the formation of a thicker upper hydrate wall deposit for higher water contents as it was observed for lower liquid loading (< 70 %vol.).

At this point, considering the regions presented in Figure 5.12, the main mechanism of region I is the agglomeration process. The wave effect is the primary mechanism of regions II and III. The competition of these two mechanisms will determine the morphology of the Region IV.

#### 5.4.4 Long-time scale mechanisms

In most experiments, the first few minutes into the beginning of the hydrate formation (usually less than 30 min) determine the main mechanisms leading to hydrate accumulation. Still, minor changes can occur as a consequence of the long duration of the experiments, which last about 48 hours after the onset of formation. These variations in the hydrate accumulation morphology may not occur in field operations as they are related to the long-time scale.

Annealing is related to the hardening of the hydrate structure as the effective volume of the porous hydrate structure shrinks. Over time the liquid trapped inside the porous hydrate structure can be expelled because of the pressure drop (in pore level), resulting in the packaging of the hydrate deposit. In addition, the water trapped inside the pores can be converted to hydrates — depending on the diffusion rate, pressure and temperature — thus reducing the pore volume. The annealing process reduces the porosity of the hydrate deposit, increasing its stability.

On the contrary to that, the expansion of the hydrate deposit into the gas phase was reported by Zhang et al. (2020) when the flowable liquid vanished, and this expansion was not related to an increase in porosity. The expansion of the deposit should be associated with the diffusion of the gas into the hydrate deposit. In the experiments reported herein, #62 (80 %vol. LL, 20 %vol. WC, 18.75 rpm) and #70 (80 %vol. LL, 70 %vol. WC, 18.75 rpm), although they presented a flowable liquid phase — oil and water-free phase, respectively — with no visible hydrate particles flowing during the growth of the deposit, an increase in the effective volume of the hydrate deposit was also detected around 1 to 4 hours after the beginning of hydrate formation.

The detachment of the hydrate upper deposit, also known as sloughing events, occurs when the gravity force overcomes the adhesion force of the deposit, but that does not mean that all the deposit will be detached; just a piece or the entire deposit can be released. The presence of sloughing events can indicate an instability in the system. The successive re-attachments and detachments of the hydrate deposit observed throughout experiment #70 (80 %vol. LL, 70 %vol. WC, 18.75 rpm,  $T_{\text{upper}} = 4^{\circ}\text{C}$  and  $T_{\text{bottom}} = 10^{\circ}\text{C}$ ) confirm it. The first event occurred four hours after the beginning of hydrate formation, and Figure 5.17 shows a photo right before and soon after the sloughing event occurs. The presence of a forced gradient of temperature inside the rock-flow cell might have created the instabilities in the system contributing to the detachment of the deposits. Unfortunately (or fortunately), only one experiment in the set of oil-gas-water experiments showed this trend, making it hard to define the parameters that originated these events.

Figure 5.17— Photo from experiment #70 (80 %vol. LL, 70 %vol. WC, 18.75 rpm) showing the detachment of the upper hydrate deposit: the imminence of the sloughing event (left) and right after it has occurred (right).



Source: own authorship.

The break-up of the hydrate particles deposited on the bottom wall was observed when forcing a temperature gradient inside the rock-flow cell — upper wall temperature lower than the bottom wall temperature. The higher temperature in the bottom of the cell causes a smaller driving force for the consolidation of the hydrate particles on the bottom of the cell making it easier for these particles to be removed by the flow energy. This process was observed in the experiment #60 (80 %vol. LL, 20 %vol. WC, 11.25 rpm) and #63 (80 %vol. LL, 20 %vol. WC, 18.75 rpm), for example. In the first few minutes after the onset of the hydrate formation, some hydrate particles adhered to the wall whilst some agglomerates flowed, as the experimental conditions were inside the hybrid zone mentioned above. Later, some agglomerates



settled, forming a deposit on the bottom. At some point, the flow energy was able to break the bottom wall deposit — as the high bottom wall temperature weakened the adhesion force of the hydrate particle to the wall. The chunks remained suspended in the flow and, eventually, they began to attach to the hydrate deposit on the top of the cell. Approximately five hours later, a solid hydrate deposit on the upper wall with no visible hydrate particles flowing in the oil-continuous phase was observed, remaining so unchanged until the end of the experiment. Figure 5.18 presents some pictures of the system conditions before and after the disruption of the bottom wall deposits.

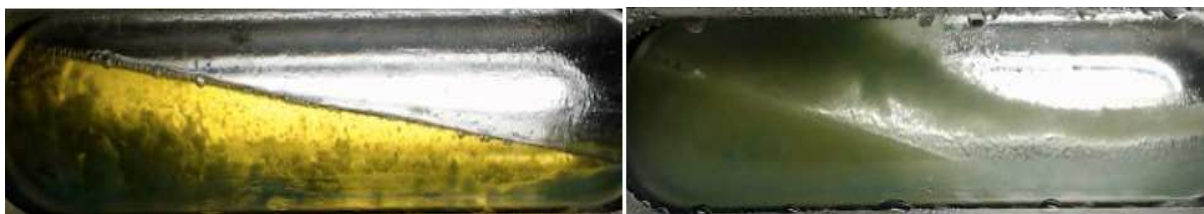
Figure 5.18— Photos of experiment #63 (80 %vol. LL, 20 %vol. WC, 18.75 rpm). a) hydrate bottom and upper wall deposit after 30 min from the onset of the hydrate formation; b) screenshot from 3h40 of the onset of the hydrate formation, the flow energy detaches chunks from the bottom wall deposit, and the hydrate particles in the flow eventually attach to the upper wall deposit; c) 48 hours after the onset of the hydrate formation, a solid hydrate deposit was formed on the upper wall, and the oil phase flows freely.



Source: own authorship.

Hydrate agglomerates started to form in experiments #42 (40 %vol. LL, 20 %vol. WC, 11.25 rpm) and #44 (80 %vol. LL, 20 %vol. WC, 18.75 rpm) after the beginning of the hydrate formation. After a few minutes (about 15 minutes), these agglomerates started to break up into small-sized agglomerates. They form a viscous hydrate slurry, creating a new hydrate morphology in the system. Figure 5.19 shows photos of experiment #42 five minutes after the onset of the hydrate formation with some agglomerates of hydrates flowing in an oil phase and minutes later, where a hydrate slurry was formed with hydrates being deposited on the wall. At this point, the liquid single-phase was able to reach the upper walls — before the onset of the hydrate formation, the water was not able to reach the upper regions as it was dispersed in the bottom of the oil-continuous phase — leading to the formation of a hydrate deposit with a hydrate slurry flowing at the bottom.

Figure 5.19— Photo from experiment #42 (40 %vol. LL, 20 %vol. WC, 18.75 rpm) exhibiting the agglomerates formed 5 minutes after the onset of the hydrate formation (left) and the hydrate slurry with an upper wall deposit formed after the beginning of the hydrate formation (right).



Source: own authorship.

The agglomerate feature remained throughout experiments #43 (40 %vol. LL, 20 %vol. WC, 11.25 rpm) and #45 (40 %vol. LL, 20 %vol. WC, 18.75 rpm) — both designed to force a gradient of temperature inside the rock-flow cell. The main difference among these experiments is the higher subcooling conditions of experiments #42 and #44 at the beginning of the hydrate formation, which may have contributed to the change in the hydrate morphology. In addition, the velocity may also have contributed to the break-up of the agglomerates, as in the experiment #40 (40 %vol. LL, 20 %vol. WC, 06 rpm) — lower velocity applied — the agglomerates formed into the first minutes of the onset of the hydrate formation remained in the system until the end of the observations.

## 5.5 Estimation of the amount of hydrate formed

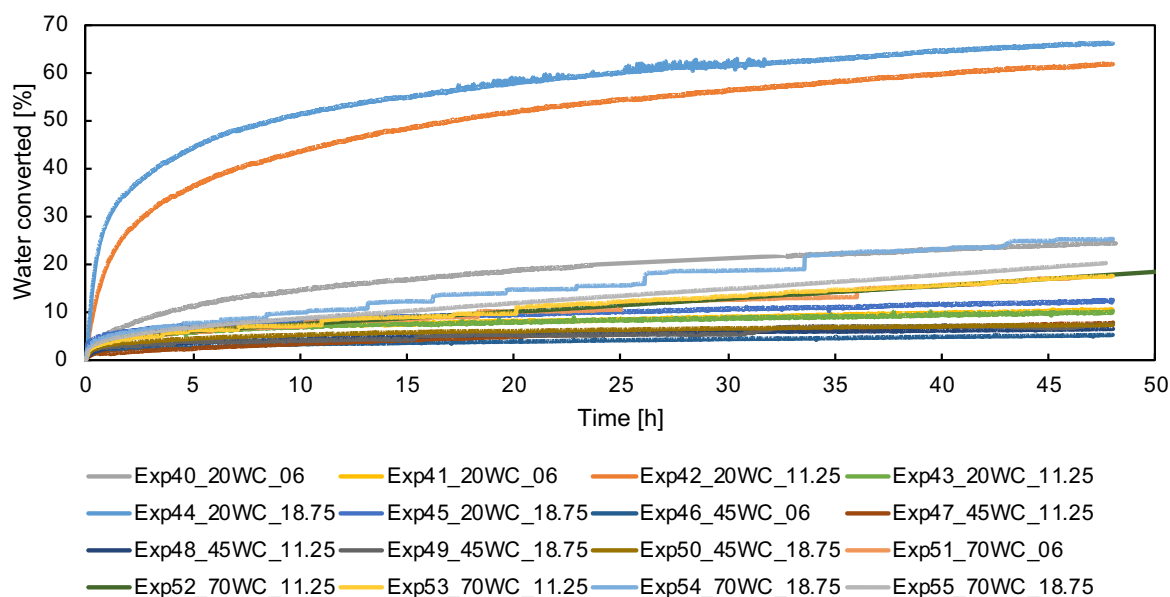
Estimating the amount of water converted to hydrates is an approximated procedure to understand the rate of hydrate formation in the experiments. The volume of gas consumed to form hydrates causes the pressure drop in the system — as a consequence of the isochoric experimental procedure employed —and it can be related to the water conversion by the hydration number — which depends on the hydrate crystalline structure formed. A more robust way to estimate the water converted to hydrates is through a thermodynamic flash routine which accounts for the variation in the system caused by pressure change. However, the composition of the mineral oil used in the experiments is not fully known, thus the methodology proposed by Straume (2017) was not employed as the computational effort would be worthless. The uncertainties in the assumption of the fluid composition would be higher. Therefore, a straightforward calculation was used. The volume of gas consumed was

estimated through the real gas equation. At the beginning of the hydrate formation, the rate of water conversion is faster, but within a few minutes (usually < 30 min), it decreases, presenting an asymptotic trend.

The process of hydrate formation and growth is limited by the heat and mass transfer in the system. The accumulation of hydrates after the beginning of the hydrate formation impacts the heat and mass transfer in the system, influencing the rate of hydrate formation and growth. The flow conditions before the beginning of the hydrate formation have an influence on the process of hydrate accumulation. In addition, the liquid loading and water content are related to the main mechanisms leading to the accumulation of hydrates in the system — agglomeration, wave effect or a combination of these two, as mentioned above. Therefore, the experimental conditions before and after the beginning of the hydrate formation, temperature, pressure condition, amount of the fluids in the system, flow conditions, and the hydrate accumulation morphology play a role in the hydrate formation rate.

The rate of water converted to hydrates for the experiments with 40 %vol. of liquid loading is shown in Figure 5.20. Experiments #42 (40 %vol. LL, 20 %vol. WC, and 11.25 rpm) and #44 (40 %vol LL, 20 %vol. WC, and 18.75 rpm) presented a higher rate of hydrate formation, which might be related to the hydrate morphology found in these systems. The formation of hydrate agglomerates was noticed into the first minutes of the onset of the hydrate formation, but these agglomerates broke down into smaller ones soon after — due to the oscillation of the cell, which promotes collision of the hydrate particles — forming a slurry with some dispersed hydrate deposits in the top region of the cell. The subcooling in those experiments was also high at the beginning of the hydrate formation, which might explain the differences in the morphology compared to the other experiments under similar conditions.

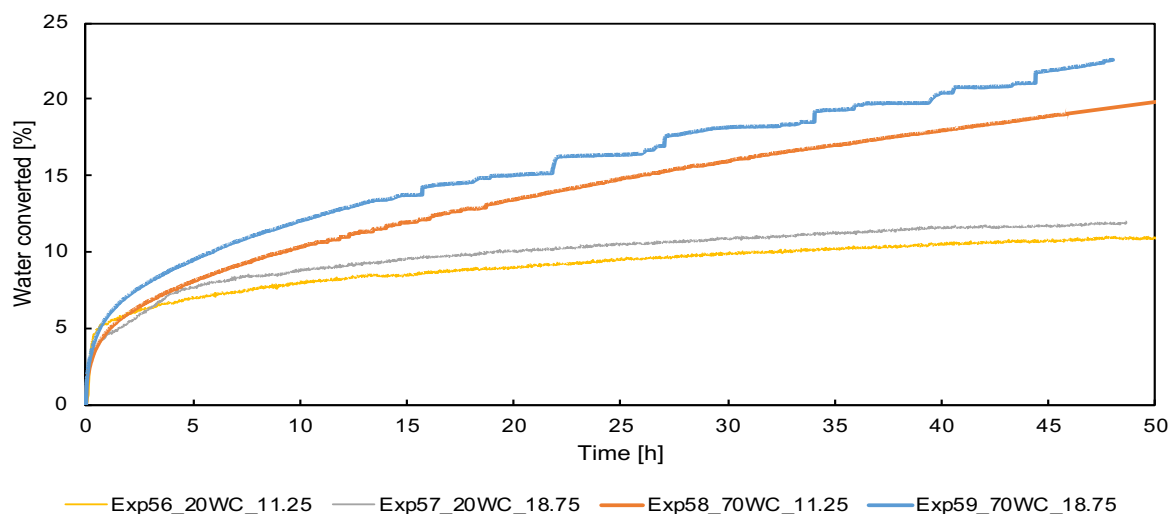
Figure 5.20— Water converted to hydrates over time for the oil-gas-hydrate-water experiments with 40 %vol. of liquid loading at different water contents, oscillation rates and under subcooling conditions.



Source: own authorship.

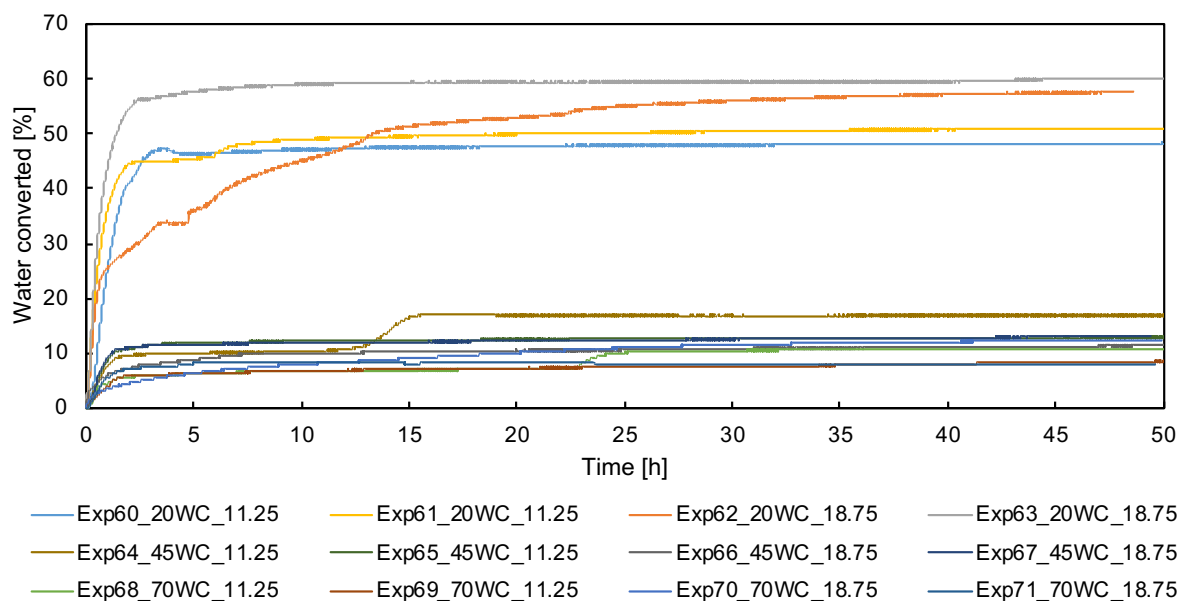
Figure 5.21 shows the percent of water converted to hydrates for 60 %vol. of liquid loading. These experiments presented a lower rate of formation when compared to the other systems studied (20 %vol. and 80 %vol. of LL). Figure 5.22 presents the water conversion to hydrate for 80 %vol. of liquid loading systems. The data can be split into two groups: one for higher growth rates — for 20 %vol. of water content experiments — and other for slower growth rates — for 45% and 70%vol. of water content systems.

Figure 5.21— Water converted to hydrates over time for the oil-gas-hydrate-water experiments with 60 %vol. of liquid loading at different water contents, oscillation rates and under subcooling conditions.



Source: own authorship.

Figure 5.22— Water converted to hydrates over time for the oil-gas-hydrate-water experiments with 80 %vol. of liquid loading at different water contents, oscillation rates and under subcooling conditions.

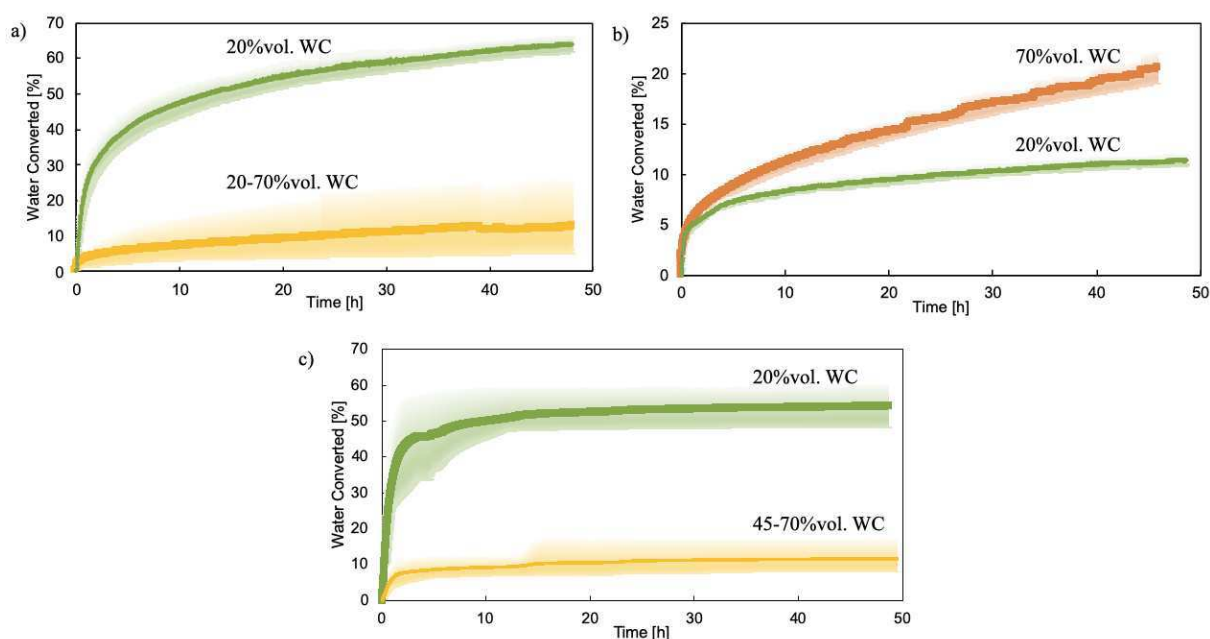


Source: own authorship.

These findings are grouped in Figure 5.23. The average water converted to hydrates is plotted as bold lines, whereas the shaded region is the deviation value. The amount of water converted to hydrates for the parameters analysed herein did not exceed the rate of 65%, with most of the experiments below 20% of water conversion. Overall, the data can be split into two main trends: one with a low formation rate ranging

from 9% to 16% and the other with a higher water conversion rating from 50% to 65%. In most experiments, the remaining water in the system, the unconverted water, was trapped within the porous hydrate deposits. Still, as discussed in the sections above, a free aqueous phase or a slurry composed of mineral oil, hydrate particles and water could be observed at the end of some experiments.

Figure 5.23— Amount of water converted to hydrates over time. a) for 40 %vol. systems; b) for 60 %vol. systems; c) for 80 %vol. systems. The curves were grouped by rate of conversion and water content. The average water converted to hydrates is denoted by bold lines, and the shaded areas are the regions of deviation values.



Source: own authorship.


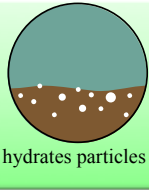
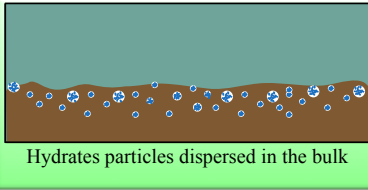
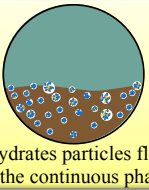
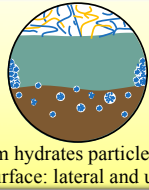
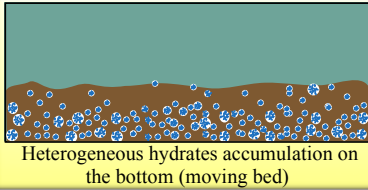
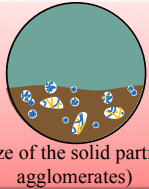
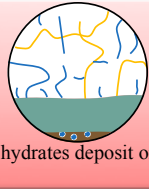
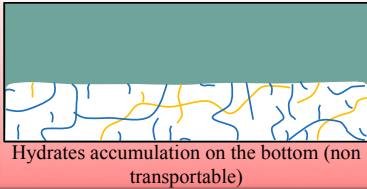
## 5.6 Flow risk analysis

Flow assurance is a major challenge for the oil and gas production system. Generally, the presence of gas hydrates is not welcome in the production system because of the risk of flow impairment and safety issues. The techniques used to prevent gas hydrate formation and agglomeration can be costly. Reducing both the costs with inhibition and the risk associated with hydrate plug formation are concerns in the oil and gas industry. Therefore, efforts have been made to develop better hydrate management strategies. Should it be possible to know the most suitable location for the deposition of hydrate and to assess the risk involved in the accumulation

mechanisms, a more cost-effective hydrate management strategy could be used. In this context, quantifying the risk of hydrate formation and accumulation can be helpful to expand the experimental findings for flow assurance considerations in field flow, standardise the assessment of the different experimental apparatus and reduce the subjective interpretations due to the visual observation bias. The flow index methodology proposed by Melchuna et al. (2020) was applied in the analysis herein presented.

Figure 5.24 shows the flow risk index classification, adapted from the one presented by Melchuna et al. (2020). The combination of the aggregation effect, wall deposition and bedding under three different conditions (pass, moderate, and fail) assesses the risk. A colourmap (red, green and yellow) was used to facilitate the visual assessment of the flow risk: green (pass, +0) represents a risk-free condition; yellow (moderate, +1) indicates a potential threat and is therefore considered as a mixed condition; and red (fail, +2) a high-risk condition.

Figure 5.24— Classification of hydrate mechanisms for flow risk analysis of oil-gas-water systems. The brown colour represents the liquid phase. Green characterises the gas phase, and white symbolises the hydrate deposits or particles. The background colours (green, yellow and red) were used as a method to facilitate risk assessment.

	AGGREGATION	WALL DEPOSITION	BEDDING
PASS (+0)	 <p>Small particle size (not visible by naked eyes)</p>	 <p>No visible hydrates particles on the wall</p>	 <p>Hydrates particles dispersed in the bulk</p>
MODERATE (+1)	 <p>Uniform hydrates particles flowing (the viscosity of the continuous phase increase)</p>	 <p>Non-uniform hydrates particles on the wall (wetted surface: lateral and upper wall)</p>	 <p>Heterogeneous hydrates accumulation on the bottom (moving bed)</p>
FAIL (+2)	 <p>Irregular size of the solid particles (larger agglomerates)</p>	 <p>Uniform hydrates deposit on the wall</p>	 <p>Hydrates accumulation on the bottom (non transportable)</p>

Source: adapted from Melchuna et al. (2020).

The aggregation mechanism expresses the interaction of hydrate particles due to the capillary effect, which can form agglomerates of different sizes. The pass

condition (grade 0) is related to the precipitation of solid particles of small size, which may or may not be visible to the naked eye; but should they be visible to the naked eye and have a uniform size distribution, it is a moderate condition (grade 1); but if the solid particles have an irregular or larger size (large agglomerates) they correspond to the fault condition (grade 2).

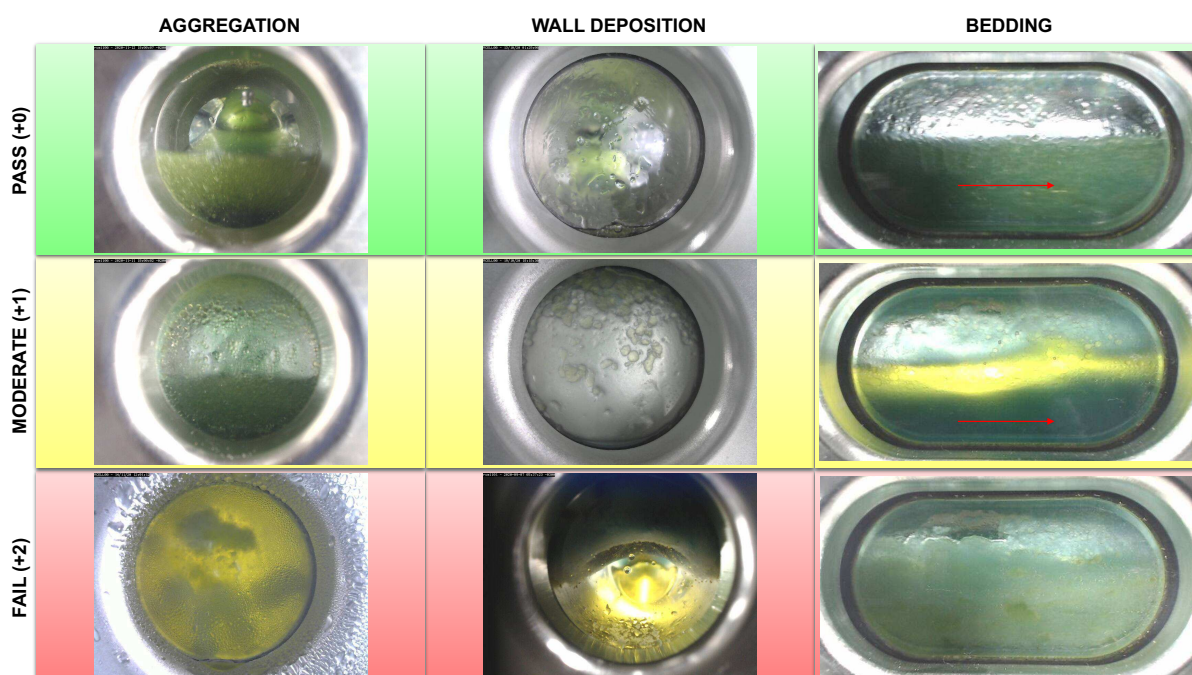
Hydrate deposition on the wall is described as solid particles adhering to the wall followed by the growth of the hydrate deposit — through the aggregation of new solid particles, which were floating in the bulk, and conversion to hydrates of hydrate-forming compounds on the deposit surface —, or expansion of the solid deposit due to the conversion of the water trapped inside the porous solid structure, or by hardening of the deposit (annealing). The hydrate deposits can occur at different positions of the cell following a non-uniform distribution because of the hydrodynamics of the system before the beginning of the hydrate formation and multiphase flow conditions after the hydrate formation. Therefore, the risk analysis criterion for this mechanism was defined as a pass condition for hydrate particles not adhering to the wall; a moderate condition if the hydrate particles adhere to the wall forming a thin solid layer or a non-uniform deposit with scattered distribution; and a fault condition if a uniform distribution of a hydrate deposit or a thicker hydrate deposit is observed in more than one position of the cell.

The bedding mechanism is related to the interaction between the hydrate particles and the flow. The water density is usually higher than the density of the hydrate; therefore, the hydrate particles tend to float. The criterion used for a risk analysis was defined as a pass condition for the homogeneous dispersion of hydrate particles in the flow, a moderate condition for heterogeneous dispersion of hydrate particles — viscous flow caused by a large amount of hydrate particles in the bulk — or when a thin, moving hydrate layer is observed at the bottom of the cell; and a fault condition for the settlement of hydrate particles at the bottom of the cell, resulting in a non-transportable condition.

Figure 5.25 illustrates the classification of the flow risk index described above through the photos taken during the experiments. The photos may show multiple mechanisms simultaneously since it is hard to isolate the mechanisms described above.



Figure 5.25— Photos of the classification for aggregation, wall deposition and bedding mechanisms according to flow risk criterion for oil-gas-hydrate-water systems. The red arrow indicates that the bulk phase is in motion. The aggregation and wall deposition show photos from the side view of the rock-flow cell and the bedding from the front views.



Source: own authorship.

The flow risk analysis of the experiments focused on what happened in the middle of the rock-flow cell because of the edge effect that can mask the actual condition. The oscillation motion and the smaller scale of the cell provokes a recirculation fluid zone at the ends of the cell — edge effect — resulting in hydrate build-up. The footage was analysed 5 minutes after the beginning of the hydrate formation to capture the first minutes of the hydrate appearance and growth where the driven force is higher and at the end of the experiment as an approach to capture any transformation of the initial hydrate morphology during the investigation.

Table 5.2 presents the flow risk index for the experiments performed for oil-gas-hydrate-water systems. The hydrate formation and accumulation in oil-gas-water systems result in severe concerns regarding the transportability of the fluids and plug formation. The higher the flow risk index, the higher the risk of interruption of production and pressure build-up.

Table 5.2— Flow risk analysis for oil-gas-hydrate-water systems. Grade 0 represent a pass condition, grade 1 is a moderate condition, and grade 2 is a fault condition. The maximum flow risk index is 12 indicating a high risk of flow disruption.

Exp.	Flow Risk	Aggregation		Wall Deposition		Bedding	
		5 min	Final	5 min	Final	5 min	Final
40	7	2	0	1	0	2	2
41	8	2	0	1	1	2	2
42	9	2	2	1	1	2	1
43	8	2	0	1	1	2	2
44	9	2	2	1	1	2	1
45	8	2	0	1	1	2	2
46	8	1	0	1	2	2	2
47	8	1	0	1	2	2	2
48	9	2	0	1	2	2	2
49	9	2	0	1	2	2	2
50	9	2	0	1	2	2	2
51	5	1	0	1	2	1	0
52	8	1	0	2	2	1	2
53	6	1	0	2	2	1	0
54	6	1	0	2	2	1	0
55	6	1	0	2	2	1	0
56	8	2	0	1	1	2	2
57	8	2	0	1	1	2	2
58	8	1	0	2	2	1	2
59	8	1	0	2	2	1	2
60	8	1	0	1	2	2	2
61	5	1	0	1	2	1	0
62	7	1	0	1	1	2	2
63	4	1	0	1	2	0	0
64	4	1	0	1	2	0	0
65	6	1	0	1	2	0	2
66	6	1	0	1	1	1	2
67	6	1	0	1	2	0	2
68	6	1	0	1	2	0	2
69	6	1	0	1	2	0	2
70	7	1	0	2	2	0	2
71	5	1	1	1	2	0	0

Source: own authorship.

An increase of water in the system appears to have built a lower flow risk index. However, the formation of a thicker hydrate deposit must have masked the hazard to this kind of system. As the deposit grew, the intensity of the other mechanisms must

have been reduced, giving a lower flow risk index to the other conditions, aggregation and bedding. The hydrate deposit quickly builds up, reducing the cross-section area, restricting the flow and leading to plugging formation in the worst case. In the aggregation case, the size of the agglomerates formed has a lower capacity to block the pipe, imposing a lower risk of flow disruption. Despite the moderate and fault bedding conditions not fully obstructing the flow section, they caused flow impairment because of the low flow energy, imposing a higher flow risk index.

## 5.7 Final considerations of the chapter

This chapter showed the experimental results obtained for the hydrate formation and accumulation in oil-gas-water systems. The main conclusions drawn from this chapter are:

- Flow conditions before the beginning of the hydrate formation have been proven to influence the location of the deposit as the areas where the water phase may have wetted indicate. The flow conditions were classified into four regions as a function of the liquid loading and the water content studied, see Figure 5.5. These regions differ in the number of phases formed and in the dispersion of the oil and water phases.
- Four different hydrate morphologies — agglomerates deposit on the bottom; porous wall deposits with no visible liquid phase flowing; thicker upper hydrate deposit; bottom and upper wall depositions with a mobile liquid phase— were found as a function of the liquid loading and the water content. Figure 5.12 illustrates the final hydrate morphology as a function of liquid loading and water content. The competition of two mechanisms — agglomeration and wave effect — and the flow conditions define the different hydrate morphologies found.
- Analysing Figure 5.12 and the mechanism described in subsection Figure 5.4, for liquid load below 70%vol. and low water content (< 20%vol.) the main mechanism is the agglomeration process. The wave effect is the primary mechanism for liquid load below 70%vol. and

high water content ( $> 20\%$ vol.). The competition of these two mechanisms will determine the hydrate morphology above  $70\%$ vol.

- The agglomeration efficiency will depend on the rate of hydrate particle collisions, the cohesive force between hydrate-hydrate particles to form the aggregate, and the shear stress to disrupt the aggregate. Note that the agglomeration only occurs in the presence of the oil phase. The agglomeration process takes place whilst the hydrate particles are water-wet.
- When free water exists after the beginning of the hydrate formation in an oil-gas-hydrate-water system, the hydrate wall deposition process will be controlled by the wave effect. Under this condition, the wave effect acts like in a  $100\%$  water-cut system.
- The wave effect efficiency will depend on the rate of hydrate particle-wall collisions, the cohesive force between hydrate particle-wall, the contact time to consolidate the liquid bridge formed between particle-wall and the shear stress that can detach the particle from the wall depending on the flow conditions.
- For the wave effect to occur, the following conditions must be present: the wall must present affinity to the water phase (hydrophilic material), water should exist as a free phase after the beginning of hydrate formation, and the gas phase needs to reach the surface of the deposit for a quick crystallisation of the liquid bridge.
- For the oil-gas-hydrate-water systems, sloughing events were observed in one single experiment, making it hard to define the parameters that gave rise to these events in this kind of system.
- The hardening of the structure, the volume expansion, and the detachment of the hydrate structure are all transformations of the hydrate macro-morphology related to long timescales. But there is a slight chance that it occurs in field operations because of the required time to form these morphologies.

- In general, the amount of water converted to hydrates in all experiments described herein can be split into two main groups: one for a lower rate of water conversion to hydrates ranging from 9% to 16%, and the other for a higher water conversion rating from 50% to 60%.
- The hydrate formation and accumulation in oil-gas-water systems result in severe concerns regarding the transportability of fluids and plug formation.

## 6. CONCLUSIONS

This study aims to expand the knowledge of the mechanisms involved in the process of hydrate formation and accumulation in multiphase flows to support hydrate management strategies and guarantee operational and safety efficiency.

The literature review showed that few studies focused on hydrate wall deposition in multiphase flow. The hydrate wall deposition reduces the pipeline cross-section area affecting the flow rate, causing impairment of the production system and eventually leading to pipeline blockage in the worst-case scenario. It highlights the importance of studying the mechanisms influencing hydrate accumulation with a focus on wall deposition.

This study investigated the process of hydrate formation and accumulation in multiphase flow based on experiments performed in a rock-flow cell. The rock-flow cell apparatus allows the simulation of the pipeline heat transfer and flow conditions. The main differences brought by using this apparatus regarding pipelines come from: i) the gravity-driven flow in contrast to pressure-driven flow, ii) the fluid collision with the lateral walls at both the ends of the cell, forming a recirculation region, iii) mass-limited condition instead of the constant supply of water and hydrocarbons (oil and gas) resulting in a continuous hydrate formation. These differences must be considered when extending the rock-flow cell analysis to flowline conditions.

Through the analysis of the experiments described herein, the flow conditions before the beginning of the hydrate formation (or, in other words, the hydrodynamics of the system) proved important to understand the system morphology in the presence of gas hydrates.

The discrepancies in the induction time amongst the experiments confirmed the stochastic nature of the hydrate nucleation. The average induction time for the methane gas-water system was 2 hours and 2.2 hours for the gas mixture-water system, whereas for the oil-gas mixture-water system it was 4.7 hours.

Moreover, the primary mechanism presented during the first few minutes into the beginning of the hydrate formation (usually less than 30 min) determines the hydrate accumulation and deposition process. Still, minor changes occurred as a consequence of the long duration of the experiments, such as annealing, expansion of

the hydrate deposit into the gas phase, sloughing events or the break-up of the agglomerates forming a slurry. These variations in the hydrate accumulation morphology may not occur in field operations as they are related to long-time scales.

The findings indicate that the presence of a water-free phase in the production system when inside the hydrate formation zone may increase the risk of flow disruption since the wave effect promotes quick hydrate build-up (deposition) on the wall. The increase of the water produced from mature fields may increase the risk of pressure drop and hydrate plugging formation due to hydrate wall deposition.

The wave effect is the primary mechanism leading to hydrate wall deposition, and to exist the following conditions must be met: the wall presents affinity to the water phase (hydrophilic material), water exists as a free phase after the beginning of hydrate formation and the gas phase reaches the surface of the deposit for a quick crystallisation of the liquid bridge. The wall temperature plays a minor role in the process of deposition, the hydrodynamics has a major impact. However, the subcooling seems to impact the morphology of the system, especially in the first minutes after the beginning of hydrate formation as it influences the cohesion and adhesion between hydrate particles and between hydrate particles and solid surface.

The additional remarks of this work were summarised for the water and synthetic gas system, and the water, mineral oil and synthetic gas system, as follows.

## **6.1 Water and synthetic gas systems**

The main conclusions drawn from the water and synthetic gas systems are:

- Four distinct flow conditions were observed for the gas-water experiments. They are all stratified wavy flows in varied shapes, differing mainly with regard to the wall surfaces which the water may or may not wet.
- For gas-hydrate-water systems, the final morphology of the experiments was classified into five categories: (i) hydrate plug formation, (ii) cross-section reduction due to wall deposition, (iii) upper wall deposition, (iv) sloughing events and (v) a transportable hydrate slurry. These system

morphologies can be related to the flow conditions before the beginning of hydrate formation.

- For gas-water systems, the wave effect is the primary mechanism leading to hydrate wall deposition and pipeline cross-section reduction or a complete blockage. It causes the rapid deposition of hydrates, especially in the upper regions of the wall, whenever the flow conditions allow the particles to collide with the upper wall and the wettability of the solid surface is water wet.
- A conceptual hydrate formation and accumulation model in water-continuous systems was proposed based on the experiments; see Figure 4.19. The continuous supply of hydrate-forming compounds on the surface of the deposit due to the intermittent flow gradually increases the deposit thickness (vertical direction of the deposit). However, the deposit thickness also increases in the direction of the flow because of the inherent flow characteristics.
- The rate of hydrate formation is higher at the beginning of the formation, i.e., from one to five hours and slows down later, showing an asymptotic behaviour. In most experiments, the water conversion to hydrates for gas-hydrate-water systems did not exceed 30%, regardless of the gas phase. The kind of hydrate accumulation and subcooling may have influenced the hydrate formation growth rate.
- The findings from the two experiments carried out under static conditions indicate that water evaporation/condensation (diffusion) and capillarity force (water permeation on the wall) present little influence on the hydrate deposition.
- The flow risk analysis indicated hydrate formation in the gas-water system presents a high risk of production impairment due to the bedding and wall deposition formation.



## 6.2 Water, mineral oil and synthetic gas systems

The main conclusions drawn from the water, mineral oil and synthetic gas systems are:

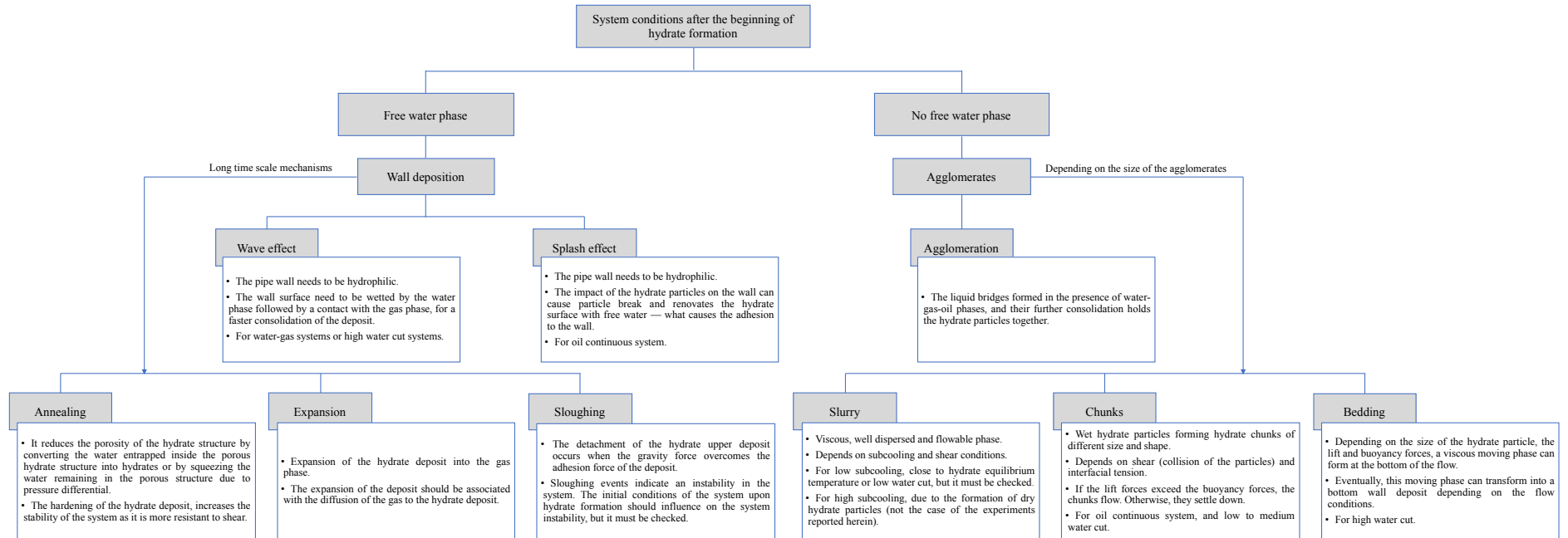
- The flow map for the oil-gas-water system before the beginning of the hydrate formation presented four regions. The four regions are all stratified-wavy flow but differ in the number of phases and in the dispersion of the oil and water phases. This flow map gives information about the shear-stabilised water-oil dispersion, influences the gas diffusion in the system, and gives hints about the process of hydrate accumulation and the location of the deposit in the system.
- The final morphology for the oil-gas-hydrate-water system can be classified into four categories. Region I presents hydrate agglomeration followed by bottom deposition. Region II shows lateral and bottom wall hydrate deposits without a liquid phase in the system. Region III exhibits the conditions for the formation of a thicker upper hydrate deposit. Region IV shows upper and bottom hydrate wall deposition independent of the water content in the system.
- The hydrate accumulation and deposition process for oil-gas-hydrate-water systems depends on the competition between hydrate agglomeration and wave effect.
- The agglomeration process of hydrate particles is the led mechanism in the systems where the water droplets are dispersed in the oil-continuous phase without the presence of a water-free phase. Note that the agglomeration process takes place whilst the hydrate particles are water-wet.
- The process of hydrate deposition on the wall will be controlled by the wave effect formation in an oil-gas-hydrate-water system when free water exists after the beginning of hydrate formation. Under these conditions, the wave effect acts as if it were a 100% water-cut system.
- The presence of both the agglomeration and the wave effect for high liquid loading (> 60 %vol.) independently of the water content in the system

indicated the presence of a hybrid system. In this condition, the competition of these two mechanisms will define the final hydrate morphology in the system. The shear stress and flow conditions might be fundamental to determining the thickness of the hydrate deposit on the upper and bottom walls.

- The amount of water converted to hydrates can be split into two main trends: one with a low formation rate ranging from 9% to 16% and the other with a high water conversion rating from 50% to 65%. The remaining water in the system can be trapped inside the porous hydrate deposits, forming a free aqueous phase or a slurry composed of mineral oil, hydrate particles and water.

The flowchart below, Figure 6.1, can serve as a guideline for the process of hydrate formation and accumulation in the oil-gas-hydrate-water system. It tries to summarise the findings presented herein in a pictorial manner.

Figure 6.1— Flowchart of the process of hydrate formation and accumulation in an oil-gas-hydrate-water system.



### 6.3 Suggestions for future investigations

This work investigated the process of hydrate formation and accumulation in gas-water and oil-gas-water system. For the oil-gas-water system, a shear-stabilised dispersion was formed depending on the flow conditions as no additives were employed to emulsify the mineral oil and water phases. The focus of the work was on the hydrate wall deposition, but the experiments also presented sloughing events, agglomeration, formation of a transportable hydrate slurry, for example. Despite all the efforts made on this study, there is still room for improvements and learning, to namely:

- Improvement of the experimental apparatus: A better instrumentation may enable the measurement of the thickness and porosity of the deposits, the gas phase composition upon the hydrate formation, or the amount of hydrate formed in the system, for example. An increase in the length of the rock-flow cell can minimise the effect of the recirculation zone thus causing lesser impacts on the visual section of the cell. The rock-flow cell creates a gravity-driven flow in contrast to the pressure driven flow of the production system. A pressure-driven flow may increase the shear in the system, making it an interesting condition to study.
- Manufacturing materials: The type of material of the viewing window and the inner pipe wall of the cell influence the system wettability and roughness. Conducting experiments with different materials, for both the inner wall and the viewing window, may improve the consistency of the results presented here.
- Morphology analysis: The hydrate accumulation morphologies — that is, sloughing and transportable hydrate slurries — discussed briefly in this work — need to be studied further in order to understand the parameters that influence those morphologies the most.
- Fluid analysis: The fluids employed in the experiments are fresh water, mineral oil, methane gas and a gas mixture composed of methane and ethane. The fluid characteristics impact on the interfacial tension, the

viscosity, and the hydrate equilibrium curve for example. Performing experiments with different fluids may improve the consistency of the findings presented herein. A different composition of the oil phase may cause an impact on the dispersion of the phases and on the shear rate in the system. Changing the gas composition can lead to different subcooling conditions or hydrate structure in the system. Experiments with salt water, instead of fresh water, would be closer to the field conditions.

- Chemical additives: additives are used in the field operations to avoid or retard the hydrate formation and agglomeration in the system. Additionally, hydrate inhibitors can be naturally present in the oil composition. Therefore, it would be interesting to use some additives in order to reproduce these conditions. Additionally, surfactants can be used to lower the water-oil interfacial tension creating emulsions. Studying the process of hydrate formation and accumulation in an emulsified system may bring new discoveries.
- Flow map: The boundary conditions of the different regions of the flow map before the hydrate formation and the hydrate morphology map were plotted. It is likely important to investigate the conditions close to the boundaries to delimit the boundary conditions of each region with a higher degree of precision.
- Flow patterns: the predominant flow pattern in all experiments before the onset of the hydrate formation was stratified wavy flow (SW). The findings presented herein showed the importance of the flow conditions to the process of hydrate formation. Therefore, different hydrate accumulation morphology for different flow patterns are expected. Different diameters of the inner cell wall or completely loading the cell with the liquid phase leaving dispersed gas bubbles can be helpful to the development of different flow patterns.
- Pipeline: different diameters, wall rugosities or even the wettability of the wall surface may cause an influence on the process of hydrate formation and accumulation, making it an interesting point to be investigated.

- Hydrate equilibrium curve: it might be interesting to investigate the hydrate formation and accumulation near the hydrate equilibrium curve. The proximity of the experimental temperature to the hydrate equilibrium curve can be responsible for the formation of a transportable hydrate slurry in the methane gas-water system. Only two experiments showed this behaviour, making it hard to find the reasons behind this fact.

## REFERENCES

- Aman, Z.M., Brown, E.P., Sloan, D., Sum, A.S., Koh, C.A. 2011. Interfacial mechanism governing cyclopentane clathrate hydrate adhesion/cohesion. *Physical Chemistry Chemical Physics*, 13: 19796-19806. <https://doi.org/10.1039/C1CP21907C>.
- Aman, Z.M., Di Lorenzo, M., Kozielski, K., Koh, C.A., Warriar, P., Johns, M.L., May, E.F. 2016. Hydrate formation and deposition in a gas-dominant flowloop: initial studies of the effect of velocity and subcooling. *Journal of Natural Gas Science and Engineering*, 35: 1490-1498. <https://doi.org/10.1016/j.jngse.2016.05.015>.
- Aspene, G., Høiland, S., Barth, T., Askvik, K.M., Kini, R.A., Larsen, R. 2008. Petroleum hydrate deposition mechanisms: the influence of pipeline wettability. 6th International Conference on Gas Hydrates, Vancouver, 6-10 July. <https://doi.org/10.14288/1.0041092>.
- Austvik, T., Hustvedt, E., Gjertsen, L.H., Urdahl, O. 1997. Formation and removal of hydrate plugs – field trial at Tommeliten. 76th GPA Annual Convention, San Antonio, 10-12 March.
- Bassani, C.L., Melchuna, A.M., Cameirão, A. et al. 2019. A multiscale approach for gas hydrates considering structure, agglomeration, and transportability under multiphase flow conditions: I. Phenomenological model. *Industrial & Engineering Chemistry Research*, 58 (31). <https://doi.org/10.1021/acs.iecr.9b01841>.
- Bassani, C.L. 2020. A multiscale approach for gas hydrates considering structure, growth kinetics, agglomeration and transportability under multiphase flow conditions. PhD Thesis in collaboration of Federal University of Technology – Paraná, Curitiba, Brazil, and Mines Saint-Etienne, Université de Lyon, Saint-Etienne, France.
- Brown, E., Hu, S., Wang, S., Wells, J., Nakatsuka, M., Veedu, V., Koh, C. 2017. Low-adhesion coatings as a novel gas hydrate mitigation strategy. Offshore Technology Conference, Houston, 1-4 May. OTC-27874-MS. <http://doi.org/10.4043/27874-MS>.
- Dholabhai, P.D., Kalogerakis, N., Bishnoi, P.R. 1993. Evaluation of gas hydrate formation and deposition in condensate pipelines: pilot plant studies. *SPE Production & Facilities*, 8 (3): 185-190. SPE-22829-PA. <http://doi.org/10.2118/22829-PA>.
- Estanga, D., Walsh, M., Subramanian, S., Creek, J. 2014. Natural gas hydrate deposition in liquid systems. 8th International Conference on Gas Hydrates, Beijing, China, 28 July – 1 August.
- Fossen, M., and Shmueli, A. 2017. Evaluation of gas hydrates operation zone to establish an optimal hydrate management strategy. Offshore Technology Conference, Brazil, 24-26 October. OTC-28087-MS. <https://doi.org/10.4043/28087-MS>.

Freitas, A.M., Lobão, A.C., Cardoso, C.B. 2002. Hydrate blockages in flowlines and subsea equipment in Campos basin. Offshore Technology Conference, Houston, 6-9 May. OTC-14257-MS. <https://doi.org/10.4043/14257-MS>.

Grasso, G.A., Sloan, E.D., Koh, C.A. et al. 2014. Hydrate deposition mechanisms on pipe walls. Offshore Technology Conference, Houston, 5-8 May. OTC-25309-MS. <https://doi.org/10.4043/25309-MS>.

Hatton, G.J., Kruka, V.R., Guinn, J.A., Greig, G.N. 1997. Hydrate plug dissociation field test. Offshore Technology Conference, Houston, 5-8 May. OTC-8521-MS. <https://doi.org/10.4043/8521-MS>.

Hatton, G.J., Pulici, M., Curti, G., Mansueto, M., Kruka, V.R. 2002. Deepwater natural gas pipeline hydrate blockage caused by a seawater leak test. Offshore Technology Conference, Houston, 6-9 May. OTC-14013-MS. <https://doi.org/10.4043/14013-MS>.

Hernandez, O.C. 2006. Investigation of hydrate slurry flow in horizontal pipelines. Ph.D. thesis, The University of Tulsa, Oklahoma, United States.

Holder, G.D., and Hand, J.H. 1982. Multiple-phase equilibria in hydrates from methane, ethane, propane and water mixtures. *AIChE Journal*, 28 (3): 440-447. <http://dx.doi.org/10.1002/aic.690280312>.

Kakitani, C., Marques, D.C., Neto Marcelino, M.A. et al. 2022. Experimental characterization of hydrate formation in non-emulsifying systems upon shut-in and restart conditions. *Fuel*, 307. <https://doi.org/10.1016/j.fuel.2021.121690>.

KBC. (2014). Multiflash 4.4. Infochem/KBC Advanced Technologies plc.

Lachance, J.W., Keinath, B.L. 2015. Hydrate cold restarts: paradigm shifts in hydrate management. International Petroleum Technology Conference, Qatar, 6-9 December. IPTC-18432-MS. <https://doi.org/10.2523/IPTC-18432-MS>.

Lachance, J.W., Talley, L.D., Shatto, D.P., Tuner, D.J., Eaton, M.W. 2012. Formation of hydrate slurries in a once-through operation. *Energy & fuels*, 26 (7): 4099-4066. <http://doi.org/10.1021/ef3002197>.

Lingelem, M.N., Majeed, A.I., Stange, E. 1994. Industrial experience in evaluation of hydrate formation, inhibition, and dissociation in pipeline design and operation. *Annals of the New York Academy of Science*, 715: 75-93. <https://doi.org/10.1111/j.1749-6632.1994.tb38825.x>.

Liu, X., Zhang, J., Li, Y., Ning, Y., Liu, Z. 2021. Experimental investigation on the process of hydrate deposition using a rock-flow cell. *Fuel*, 306. <https://doi.org/10.1016/j.fuel.2021.121607>.

Lund, A., Hjarbo, K.W., Larsen, R., Straume, E.O., Høiland, S., Bracey, J.T. 2008. Black oil hydrate behavior – a comparison study of testing techniques: Sintef wheel and multicell. 6th International Conference on Gas Hydrates, Vancouver, 6-10 July.



Marques, D., Bassani, C.L., Kakitani, C. et al. 2022. Mapping wall deposition trends of gas hydrates: I. Gas-water-hydrate systems. *Industrial & Engineering Chemistry Research*, 61 (5), 2333-2345. <https://doi.org/10.1021/acs.iecr.1c04723>.

Melchuna, A., Zhang, X., Sa, J. et al. 2020. Flow risk index: a new metric for solid precipitation assessment in flow assurance management applied to gas hydrate transportability. *Energy & Fuels*, 34: 9371-9378. <https://dx.doi.org/10.1021/acs.energyfuels.0c01203>.

Nicholas, J.W., Dieker, L.E., Sloan, E.D., Koh, C.A. 2009a. Assessing the feasibility of hydrate deposition on pipeline walls – Adhesion force measurements of clathrate hydrate particles on carbon steel. *Journal of Colloid and Interface Science*, 331 (2): 322-328. <https://doi.org/10.1016/j.jcis.2008.11.070>.

Nicholas, J.W., Koh, C.A., Sloan, E.D., Nuebling, L., He, H., Horn, B. 2009b. Measuring hydrate/ice deposition in a flow loop from dissolved water in live liquid condensate. *American Institute of Chemical Engineers Journal*, 55 (7): 1882-1888. <https://doi.org/10.1002/aic.11874>.

Olajire, A.A. 2020. Flow assurance issues in deep-water gas well testing and mitigation strategies with respect to gas hydrates deposition in flowlines – A review. *Journal of Molecular Liquids*, 318. <https://doi.org/10.1016/j.molliq.2020.114203>.

Oliveira, M.C.K. de, Gonçalves, M. de A.L., Marques, L.C. do C. 2018. *Fundamentos de Garantia de Escoamento*. Rio de Janeiro: Interciência.

Pickarts, M.A., Ravichandran, S., Ismail, N.A. et al. 2022. Perspective on the oil-dominated gas hydrate plugging conceptual picture as applied to transient shut-in/restart. *Fuel*, 324. <https://doi.org/10.1016/j.fuel.2022.124606>.

Rajnauth, J. 2013. A proposed workflow for disposal of carbon dioxide using carbon dioxide hydrate. *The Journal of the Association of Professional Engineers of Trinidad and Tobago*, 41 (1): 18-22.

Rao, I., Koh, C.A., Sloan, E.D. et al. 2013. Gas hydrate deposition on cold surface in water-saturated gas systems. *Industrial & Engineering Chemistry Research*, 52 (18): 6262-6269. <https://doi.org/10.1021/ie400493a>.

Ravichandran, S., and Daraboina, N. 2019. Mechanistic model to predict hydrate deposition under stratified flow conditions. *Energy & Fuels* 33 (10): 9510-9519. <https://doi.org/10.1021/acs.energyfuels.9b01624>.

Sahu, P., Krishnaswamy, S., Ponnani, K., Pande, N.K. 2018. A thermodynamic approach to selection of suitable hydrate formers for seawater desalination. *Desalination*, 436: 144-151. <https://doi.org/10.1016/j.desal.2018.02.001>.

Sloan, E.D. and Koh, C. 2008. *Clathrate hydrates of natural gases*, third edition. CRC Press.

Sloan, D., Koh, C., Sum, A.K. 2011. Natural gas hydrates in flow assurance. Gulf Professional Publishing. <https://doi.org/10.1016/B978-1-85617-945-4>.

Song, G., Li, Y., Wang, W. et al. 2018. Investigation on the mechanical properties and mechanical stabilities of pipewall hydrate deposition by modelling and numerical simulation. *Chemical Engineering Science*, 192: 477-487. <https://doi.org/10.1016/j.ces.2018.07.055>.

Song, G., Li, Y., Sum, A.K. 2020. Characterization of the coupling between gas hydrate formation and multiphase flow conditions. *Journal of Natural Gas Science and Engineering*, 83. <https://doi.org/10.1016/j.jngse.2020.103567>.

Srivastava, V., Majid, A. A. A., Warriar, P., Grasso, G., Chaudhari, P., Sloan, E.D., Koh, C. Wu, D.T., Zerpa, L.E. 2017. Hydrate Formation and transportability investigations in a high-pressure flowloop during transient shut-in/ restart operations. Offshore Technology Conference, Houston, 1-4 May. OTC-27849-MS. <https://doi.org/10.4043/27849-MS>.

Straume, E.O., Merino-Garcia, D., Sum, A.K., Morales, R.E.M. 2015. Hydrate formation in condensate and mineral oil systems. Offshore Technology Conference, Brazil, 27-29 October. OTC-26189-MS. <https://doi.org/10.4043/26189-MS>.

Straume, E.O. 2017. Study of gas hydrate formation and wall deposition under multiphase flow conditions. Ph.D. thesis, Federal University of Technology - Paraná, Curitiba, Brazil (May 2017).

Strobel, A.T., Hester, K.C., Koh, C.A., Sum, A.K., Jr. Sloan, E.D. 2009. Properties of the clathrates of hydrogen and developments in their applicability for hydrogen storage. *Chemical Physics Letters*, 278 (4-6): 97-109. <https://doi.org/10.1016/j.cplett.2009.07.030>.

Sum, A.K., Burruss, R.C., and Sloan, E.D. 1997. Measurement of Clathrate Hydrates via Raman Spectroscopy. *J. Phys. Chem.*, 101 (38): 7371-7377. <https://doi.org/10.1021/jp970768e>.

Sum, A.K., Koh, C.A., Sloan, E.D. 2012. Developing a comprehensive understanding and model of hydrate in multiphase flow: from laboratory measurements to field applications. *Energy & Fuels*, 26 (7): 4046-4052. <https://doi.org/10.1021/ef300191e>.

Taheri, Z., Shabani, M.R., Nazari, K., Mehdizaheh, A. 2014. Natural gas transportation and storage by hydrate technology: Iran case study. *Journal of Natural Gas Science and Engineering*, 21: 846-849. <http://dx.doi.org/10.1016/j.jngse.2014.09.026>.

Veibestad, A., Larsen, R., Straume, E., Argo, C.B., Fung, G. 2005. Assessment of hydrate plugging potential of king Gulf of Mexico black oil. 5th International Conference on Gas Hydrates, Trondheim, 12-16 June.

Zhang, W., Wang, Y., Lang, X., Fan, S. 2017. Performance analysis of hydrate-based refrigeration system. *Energy Conversion and Management*, 146: 43-51. <http://dx.doi.org/10.1016/j.enconman.2017.04.091>.

Zhang, X., Melchuna, A., Sa, J. et al . 2020. Gas hydrates porosity and effective volume under multiphase flow conditions. *Journal of Natural Gas Science and Engineering*, 79. <https://doi.org/10.1016/j.jngse.2020.103340>.

Zhao, J., Wang, B., Sum, A.K. 2017. Dynamics of hydrate formation and deposition under pseudo multiphase flow. *American Institute of Chemical Engineers Journal*, 63 (9): 4136-4146. <https://doi.org/10.1002/aic.15722>.

## APPENDIX A — PROCEDURE FOR THE ESTIMATION OF THE AMOUNT OF HYDRATE FORMED

The experiments were performed in a closed system under isochoric conditions. Therefore, any variation in the amount and volume of components in the phases is a consequence of P and T variations.

An algorithm to estimate the amount of hydrate formed in the system was presented by Straume (2017). The amount of component in each phase was determined based on flash calculations performed in a Microsoft Excel® spreadsheet by calling Multiflash® (v.6.1.35, 2017) libraries, and volume balance. The system is assumed to be under equilibrium conditions at each measured pressure and temperature for flash calculations.

The pressure and temperature conditions measured, the volume of the rock-flow cell and the initial amount of each component admitted in the system is the input data for the flash calculation and, therefore, for the estimation of the amount of hydrate formed after the beginning of hydrate formation.

Above is presented a brief summary of the procedure and simplifications needed to perform the estimation of the amount of hydrate formed for the gas-water-hydrate systems:

- i. The composition of the gas and aqueous phases ( $X_{G,Ci}$ ,  $X_{G,W}$ ,  $X_{Aq,G}$ ,  $X_{Aq,W}$ ) and molar volume of the phases ( $V_{M,G}$  and  $V_{M,Aq}$ ) is obtained from flash calculations. The inputs to start the estimations, the unknown components, are the quantity of each phase measured in mol,  $n_G$  and  $n_{Aq}$ , and the unknown, but fixed quantity of filled gas in mol,  $n_{C1}$  and  $n_{C2}$ .
- ii. The amount of the water is calculated by the Eq.A.1 and the amount of gas admitted into the cell is estimated through the equation of state for a real gas. The gas compressibility factor ( $Z$ ) is given by Multiflash® whereas the gas solubility in water was neglected.

$$n_w = \frac{m_w}{M_w} \tag{Eq.A.1}$$

- iii. The total volume of the cell is known and can be expressed as Eq.A.2:

$$V_T = V_G + V_{Aq} = V_{M,G}n_G + V_{M,Aq}n_{Aq} \quad \text{Eq.A.2}$$

iv. Substituting  $V_M = 1/\rho_{mol}$  in the Eq.A.2:

$$n_G = \frac{V_T}{V_{M,G}} - \frac{V_{M,Aq}}{V_{M,G}} n_{Aq} = \rho_{mol,G} V_T - \frac{\rho_{mol,G}}{\rho_{mol,Aq}} n_{Aq} \quad \text{Eq.A.3}$$

v. The total amount of water in the system is the sum of water in each of the phases. The amount of water in the aqueous phase is found by substituting with expression for  $n_G$  from previous equation:

$$n_W = X_{G,W}n_G + X_{Aq,W}n_{Aq} \quad \text{Eq.A.4}$$

$$\begin{aligned} n_{Aq} &= \frac{n_W}{X_{Aq,W}} - \frac{X_{G,W}}{X_{Aq,W}} n_G = \frac{n_W}{X_{Aq,W}} - \frac{X_{G,W}}{X_{Aq,W}} \frac{V_T}{V_{M,G}} + \frac{X_{G,W}}{X_{Aq,W}} \frac{V_{M,Aq}}{V_{M,G}} n_{Aq} \\ &= \frac{n_W - \rho_{mol,G} X_{G,W} V_T}{X_{Aq,W}} + \frac{\rho_{mol,G} X_{G,W}}{\rho_{mol,Aq} X_{Aq,W}} n_{Aq} \end{aligned}$$

$$n_{Aq} = \frac{n_W V_{M,G} - X_{G,W} V_T}{X_{Aq,W} V_{M,G} - X_{G,W} V_{M,Aq}} = \frac{n_W - \rho_{mol,G} X_{G,W} V_T}{X_{Aq,W} - \frac{\rho_{mol,G} X_{G,W}}{\rho_{mol,Aq}}} \quad \text{Eq.A.5}$$

vi. The molar volume can be given by Multiflash<sup>®</sup> for the pressure and temperature condition. After  $n_G$  and  $n_{Aq}$  are calculated from Eq.A.3 and Eq.A.5, the quantity of each gas phase component can be calculated through Eq.A.6.

$$n_{Ci} = X_{G,Ci}n_G + X_{Aq,Ci}n_{Aq} \quad \text{Eq.A.6}$$

vii. After the beginning of hydrate formation, it is necessary to determine the composition of the gas, aqueous and hydrate ( $X_G$ ,  $X_{G,W}$ ,  $X_{Aq,G}$ ,  $X_{Aq,W}$ ,  $X_{H,G}$ ,  $X_{H,W}$ ) and molar volume of the phases ( $V_{M,G}$ ,  $V_{M,Aq}$  and  $V_{M,H}$ ). The three-phase system — gas, water, gas hydrate — is simplified to two systems of two-phase — gas-water and gas-gas hydrate. Because of it, the amount of components and volume should be corrected at each time

step so that the overall amount of components remain constant. Two flash calculations for each pressure and temperature step is performed.

- viii. The quantity of each of the three phases can be calculated from the equations for total volume, total amount of gas, and total amount of water in the system, Eq.A.7 to Eq.A.9 respectively.

$$V_T = V_G + V_{Aq} + V_H = V_{M,G}n_G + V_{M,Aq}n_{Aq} + V_{M,H}n_H \quad \text{Eq.A.7}$$

$$n_W = X_{G,W}n_G + X_{Aq,W}n_{Aq} + X_{H,W}n_H \quad \text{Eq.A.8}$$

$$n_{Ci} = X_{G,Ci}n_G + X_{Aq,Ci}n_{Aq} + X_{H,Ci}n_H \quad \text{Eq.A.9}$$

- ix. An approximation is made to solve the equations, Eq.A.7 to Eq.A.9, by using known values of  $n_G$  and  $n_{Aq}$  from previous time step ( $t-1$ ) in the calculation of  $n_H$  in the current time step ( $t$ ). After it, the  $n_G$  and  $n_{Aq}$  are calculated for current time step. This gives the following equation:

$$n_{Aq(t)} = \frac{n_W - X_{G,W}n_{G(t-1)}}{X_{Aq,W}} - \frac{X_{H,W}}{X_{Aq,W}}n_{H(t)} \quad \text{Eq.A.10}$$

$$n_{G(t)} = \sum_{i=1}^n \left( \frac{n_{Ci} - X_{Aq,Ci}n_{Aq(t-1)}}{X_{G,Ci}} - \frac{X_{H,Ci}}{X_{G,Ci}}n_{H(t)} \right) \quad \text{Eq.A.11}$$

$$V_T - \sum_{i=1}^n \left[ \frac{V_{M,G}(n_{Ci} - X_{Aq,Ci}n_{Aq(t-1)})}{X_{G,Ci}} \right] - \frac{V_{M,Aq}(n_W - X_{G,W}n_{G(t-1)})}{X_{Aq,W}} \quad \text{Eq.A.12}$$

$$= \left[ V_{M,H} - \sum_{i=1}^n \left( \frac{V_{M,G}X_{H,Ci}}{X_{G,Ci}} \right) - \frac{V_{M,Aq}X_{H,W}}{X_{Aq,W}} \right] n_H$$

$$n_H = \frac{V_T - \sum_{i=1}^n \left[ \frac{V_{M,G}(n_{Ci} - X_{Aq,Ci}n_{Aq(t-1)})}{X_{G,Ci}} \right] - \frac{V_{M,Aq}(n_W - X_{G,W}n_{G(t-1)})}{X_{Aq,W}}}{V_{M,H} - \sum_{i=1}^n \left( \frac{V_{M,G}X_{H,Ci}}{X_{G,Ci}} \right) - \frac{V_{M,Aq}X_{H,W}}{X_{Aq,W}}} \quad \text{Eq.A.13}$$

- x. The error in quantity of components and volume can be estimated for each time step before continuing with the calculations for the next time step.

$$n_E = \frac{\sum_{i=1}^n n_{Ci} + n_W - n_G - n_{Aq} - n_H}{\sum_{i=1}^n n_{Ci} + n_W} \quad \text{Eq.A.14}$$

$$V_E = \frac{V_T - V_{M,G}n_G - V_{M,Aq}n_{Aq} - V_{M,H}n_H}{V_T} \quad \text{Eq.A.15}$$